

# Simulation of the Anaerobic Corrosion of Carbon Steel Used Fuel Containers Using the Steel Corrosion Model Version 1.0 (SCM V1.0)

NWMO TR-2012-07

May 2012

**Fraser King<sup>1</sup> and Miroslav Kolar<sup>2</sup>**

<sup>1</sup> Integrity Corrosion Consulting Limited

<sup>2</sup> LS Computing Limited

**nwmo**

NUCLEAR WASTE  
MANAGEMENT  
ORGANIZATION

SOCIÉTÉ DE GESTION  
DES DÉCHETS  
NUCLÉAIRES

**Nuclear Waste Management Organization**  
22 St. Clair Avenue East, 6<sup>th</sup> Floor  
Toronto, Ontario  
M4T 2S3  
Canada

Tel: 416-934-9814  
Web: [www.nwmo.ca](http://www.nwmo.ca)

**Simulation of the Anaerobic Corrosion of Carbon Steel Used Fuel Containers Using the  
Steel Corrosion Model Version 1.0 (SCM V1.0)**

**NWMO TR-2012-07**

May 2012

**Fraser King<sup>1</sup> and Miroslav Kolar<sup>2</sup>**  
<sup>1</sup> Integrity Corrosion Consulting Limited  
<sup>2</sup> LS Computing Limited

---

Disclaimer:

This report does not necessarily reflect the views or position of the Nuclear Waste Management Organization, its directors, officers, employees and agents (the "NWMO") and unless otherwise specifically stated, is made available to the public by the NWMO for information only. The contents of this report reflect the views of the author(s) who are solely responsible for the text and its conclusions as well as the accuracy of any data used in its creation. The NWMO does not make any warranty, express or implied, or assume any legal liability or responsibility for the accuracy, completeness, or usefulness of any information disclosed, or represent that the use of any information would not infringe privately owned rights. Any reference to a specific commercial product, process or service by trade name, trademark, manufacturer, or otherwise, does not constitute or imply its endorsement, recommendation, or preference by NWMO.

---

## ABSTRACT

**Title:** Simulation of the Anaerobic Corrosion of Carbon Steel Used Fuel Containers Using the Steel Corrosion Model Version 1.0 (SCM V1.0)  
**Report No.:** NWMO TR-2012-07  
**Author(s):** Fraser King<sup>1</sup> and Miroslav Kolar<sup>2</sup>  
**Company:** <sup>1</sup> Integrity Corrosion Consulting Limited, <sup>2</sup> LS Computing Limited  
**Date:** May 2012

### Abstract

The results of preliminary simulations performed using the Steel Corrosion Model Version 1.0 (SCM V1.0) are presented and discussed. The SCM V1.0 simulates the anaerobic corrosion behaviour of carbon steel containers in a deep geological repository in sedimentary host rock and the impact of corrosion products on other barriers in the repository. The model is based on a series of one-dimensional reactive-transport equations that describe the various mass-transport, redox, adsorption/desorption, precipitation/dissolution, and chemical speciation processes of each of the thirteen chemical species considered in the model. Solution of these equations involves the use of a mixed-potential model based on the electrochemical reactions involved in the corrosion of the container, from which the time dependent corrosion rate and corrosion potential can be predicted, leading to an estimate of the container lifetime. An important aspect of the corrosion behaviour is the formation of a precipitated corrosion product film that blocks the surface interfacial reactions and inhibits the transport of reactants to, and of corrosion products away from, the corroding interface. The effects of slow saturation of the repository as a result of the low hydraulic conductivity of the sedimentary host rock are also taken into account.

In addition to the corrosion reactions, the model also simulates the interaction of dissolved Fe(II) ions with the bentonite clay. Those interactions may involve the adsorption of Fe(II) on the clay by ion exchange, alteration to non-swelling berthierine clay, and/or blockage of the bentonite pore volume by the precipitation of corrosion product. The generation, transport, and release of hydrogen is simulated in a simplified manner.

So-called Base Case simulations have been performed for both shale and limestone host rocks, the two cases differing in the host rock thermal properties and calcite content. The sensitivity of the predicted repository performance to certain input parameters and model assumptions was also investigated, in particular the effect of the assumed repository saturation period, the values of threshold relative humidity values that control the rates of the surface electrochemical reactions, and the assumed minimum porosity for precipitated corrosion products.

The Base Case simulations using best-estimate values of the various input parameters predict lifetimes of 11,200 to 36,500 a for carbon steel containers with a corrosion allowance of 1 to 3 cm. Extensive precipitation of corrosion product (in the form of magnetite) occurs within a few tens of cm of the container, but minimal clay alteration is predicted. The results and capabilities of the SCM are compared with both corrosion rates from laboratory and archaeological analog studies and predictions from other similar models described in the literature. Areas for further development of the model and key pieces of missing mechanistic understanding and experimental data are identified.



**TABLE OF CONTENTS**

	<b><u>Page</u></b>
<b>ABSTRACT</b> .....	<b>v</b>
<b>1. INTRODUCTION</b> .....	<b>1</b>
<b>2. STEEL CORROSION MODEL VERSION 1.0 (SCM V1.0)</b> .....	<b>2</b>
<b>2.1 CORROSION ASPECTS OF THE MODEL</b> .....	<b>2</b>
2.1.1 Reaction Scheme.....	2
2.1.2 Processes Included in the Model .....	5
2.1.2.1 Interfacial Electrochemical Processes.....	5
2.1.2.2 Film Formation.....	5
2.1.2.3 Interaction Between Fe(II) and Bentonite.....	6
2.2.2.4 Gas Generation and Transport.....	7
2.2.2.5 Unsaturated Conditions.....	7
<b>2.2 MATHEMATICAL ASPECTS</b> .....	<b>11</b>
2.2.1 Mass-balance Equations.....	11
2.2.2 Boundary Conditions.....	12
2.2.3 Model Geometry .....	14
<b>2.3 ASSUMPTIONS</b> .....	<b>16</b>
<b>3. SIMULATIONS PERFORMED USING SCM V1.0</b> .....	<b>19</b>
<b>3.1 BASE CASE SIMULATIONS</b> .....	<b>19</b>
<b>3.2 SENSITIVITY ANALYSES</b> .....	<b>21</b>
3.2.1 Saturation Time .....	21
3.2.2 Minimum Porosity .....	21
3.2.3 Threshold Relative Humidity .....	21
<b>4. RESULTS OF SIMULATIONS</b> .....	<b>22</b>
<b>4.1 BASE CASE SIMULATIONS</b> .....	<b>22</b>
4.1.1 Shale Host Rock .....	22
4.1.1.1 Phase 1 .....	22
4.1.1.2 Phase 2 .....	24
4.1.2 Limestone Host Rock.....	32
<b>4.2 SENSITIVITY ANALYSES</b> .....	<b>38</b>
4.2.1 Saturation Time .....	38
4.2.2 Minimum Porosity .....	40
4.2.3 Threshold Relative Humidity .....	42
<b>5. DISCUSSION</b> .....	<b>46</b>
<b>5.1 GENERAL OBSERVATIONS</b> .....	<b>46</b>
5.1.1 Effect of Host Rock Type .....	46
5.1.2 Effect of Saturation Time.....	46
5.1.3 Effect of Minimum Porosity .....	47
5.1.4 Effect of Threshold RH Values.....	47
<b>5.2 PREDICTION OF CONTAINER CORROSION</b> .....	<b>48</b>
<b>5.3 CONTAINER LIFETIMES</b> .....	<b>53</b>
<b>5.4 COMPARISON WITH PREVIOUS MODELLING STUDIES</b> .....	<b>53</b>
<b>5.5 FURTHER DEVELOPMENT AND IMPROVEMENTS TO THE MODEL</b> .....	<b>59</b>

<b>6.</b>	<b>CONCLUSIONS .....</b>	<b>60</b>
	<b>REFERENCES .....</b>	<b>61</b>
	<b>APPENDIX A: INPUT DATA FOR STEEL CORROSION MODEL VERSION 1.0 .....</b>	<b>67</b>

## **LIST OF TABLES**

	<b><u>Page</u></b>
Table 1: Notation for the Thirteen Species Included in the SCM V1.0. ....	3
Table 2: List of Assumptions for the SCM V1.0. ....	17
Table 3: Layer-dependent Properties for the Base Case Simulations.....	20
Table 4: Summary of the Predicted Container Corrosion Performance for the Base Case Simulations and Sensitivity Analyses.....	35
Table 5: Predicted Container Lifetime as a Function of the Corrosion Allowance. ....	53
Table 6: Comparison of Features of Various Models for the Carbon Steel-Bentonite System. ...	55

## **LIST OF FIGURES**

	<b><u>Page</u></b>
Figure 1: Reaction Scheme for the Steel Corrosion Model Version 1.0 (SCM V1.0).....	4
Figure 2: Assumed Time Dependence of the Degree of Saturation for the SCM V1.0 Base Case Simulation. ....	10
Figure 3: Assumed Time Dependence of the Degree of Saturation for the SCM V1.0 Base Case Simulation for a Period of One Thousand Years Following Repository Closure....	10
Figure 4: Cross-sectional Views of the In-room Disposal Repository Design.....	15
Figure 5: Placement Room Longitudinal Section. ....	15
Figure 6: Series of Mass-transport Layers Used for the SCM V1.0 Geometry. ....	16
Figure 7: Temporal Variation of the Degree of Saturation in the Various Layers for the Base Case SCM V1.0 Simulations. ....	19
Figure 8: Time Dependence of the Pore-water Chloride Ion Inventory During Phase 1 of the Base Case Simulation for Shale Host Rock. ....	23
Figure 9: Saturation Profiles for the Buffer and EDZ During Phase 1 of the Base Case Simulation for Shale Host Rock. ....	23
Figure 10: Predicted Time Dependence of the Corrosion Rate and Corrosion Potential of a Carbon Steel Container for the Base Case Simulation with Shale Host Rock.....	24
Figure 11: Predicted Time Dependence of the Anodic and Cathodic Current Densities for the Base Case Simulation with Shale Host Rock.....	25
Figure 12: Time Dependence of the Corrosion Rate and Interfacial Porosity Illustrating Various Stages in the Evolution of the Corrosion Behaviour. ....	25
Figure 13: Predicted Time Dependence of the Inventories of Iron-based Corrosion Products for the Base Case Simulation with Shale Host Rock.....	26
Figure 14: Time Dependence of the Accumulation of Magnetite, Adsorbed Iron, and Altered Clay for the Base Case Simulation with Shale Host Rock.....	27
Figure 15: Progression of the Magnetite “Front” for the Base Case Simulation with Shale Host Rock.....	28
Figure 16: Predicted Time Dependence of the Porosity of the Bentonite, EDZ, and Host Rock Layers for the Base Case Simulation with Shale Host Rock. ....	28
Figure 17: Concentration Profiles for Adsorbed Fe(II) as a Function of Time for the Base Case Simulation with Shale Host Rock.....	29
Figure 18: Predicted Distribution of Altered Bentonite Clay as a Function of Time for the Base Case Simulation with Shale Host Rock.....	29
Figure 19: Predicted Hydrogen Partial Pressure in the Repository for Selected Times for the Base Case Simulation with Shale Host Rock.....	31
Figure 20: Inventory of Gaseous and Dissolved Hydrogen in the Repository as a Function of Time for the Base Case Simulation with Shale Host Rock. ....	31

Figure 21: Cumulative Number of Gas Release Events for the Base Case Simulation with Shale Host Rock.....32

Figure 22: Comparison of the Distribution of Temperature and Calcite Solubility in the Buffer and Host Rock at the End of Phase 1 (4998 a) for the Base Case Simulations with Shale and Limestone Host Rock.....33

Figure 23: Comparison of the Predicted Time Dependence of the Corrosion Potential for the Base Case Simulations with Limestone and Shale Host Rocks. ....34

Figure 24: Comparison of the Predicted Time Dependence of the Corrosion Rate for the Base Case Simulations with Limestone and Shale Host Rocks. ....34

Figure 25: Comparison of the Predicted Time Dependence of the Depth of Corrosion for the Base Case Simulations with Limestone and Shale Host Rocks. ....35

Figure 26: Comparison of the Predicted Corrosion Rate and Interfacial Porosity for the Period Between 5000 a and 6000 a for the Base Case Simulations with Shale and Limestone Host Rocks. ....36

Figure 27: Comparison of the Number of Gas Releases for the Base Case Simulations with Limestone and Shale Host Rocks.....37

Figure 28: Effect of Saturation Time on the Predicted Time Dependence of the Corrosion Rate for Shale Host Rock.....38

Figure 29: Effect of Saturation Time on the Predicted Time Dependence of the Depth of Corrosion for Shale Host Rock. ....39

Figure 30: Predicted Time Dependence of the Release of Hydrogen Gas as a Function of Repository Saturation Time for Shale Host Rock.....40

Figure 31: Comparison of the Predicted Corrosion Rate for the Base Case Simulation for Shale Host Rock (epsMin = 0.01) and the Variant Case With Higher Minimum Porosity (epsMin = 0.05). ....41

Figure 32: Comparison of the Effect of Threshold Relative Humidity for the Interfacial Electrochemical Reactions on the Predicted Time Dependence of the Corrosion Rate for Limestone Host Rock. ....43

Figure 33: Comparison of the Effect of Threshold Relative Humidity on the Predicted Depth of Corrosion for Limestone Host Rock. ....44

Figure 34: Comparison of the Effect of Threshold Relative Humidity on the Predicted Time Dependence of the Corrosion Potential for Limestone Host Rock.....44

Figure 35: Effect of Relative Humidity Thresholds on the Predicted Time Dependence of Gas Release Events for Limestone Host Rock.....45

Figure 36: Comparison of the Anaerobic Corrosion Behaviour of Carbon Steel in Bulk Solution and Compacted Bentonite. ....49

Figure 37: Corrosion Rates of Buried Archaeological Iron Objects. ....50

Figure 38: Corrosion Rates of Carbon Steel and Cast Iron from Archaeological Analogs.....51

Figure 39: Schematic Illustration of the Characteristics of Corroded Archaeological Iron Objects in Soil. ....52

Figure 40: Predicted Time Dependence of the pH at the Container-Bentonite Interface.....57

Figure 41: Predicted Spatial Variation of the Volume Fraction of Original Clay Components and Corrosion and Alteration Products. ....58

## 1. INTRODUCTION

The Nuclear Waste Management Organization (NWMO) is carrying out a research and development program to support implementation of Adaptive Phase Management for the long-term management of Canada's used nuclear fuel (NWMO 2005). The NWMO program includes technologies associated with a deep geological repository (DGR) for used fuel in a suitable geological formation, such as crystalline rock or sedimentary deposits. Any such repository would be based on a multi-barrier design, comprising a number of natural and engineered barriers (Russell and Simmons 2003). One of the engineered barriers would be a long-lived used-fuel container (UFC) designed to provide long-term containment and isolation of used fuel for a considerable length of time. Copper is the reference container material for the disposal of used fuel in a DGR in crystalline rock (King et al. 2008, Maak 1999), whilst carbon steel (C-steel) has been considered for a repository in sedimentary host rock (King 2007).

Carbon steel has been considered as a potential container material for the disposal of high-level waste (HLW) and used fuel in a number of countries, including France (Andra 2005), Japan (JNC 2000), Switzerland (Nagra 2002), Belgium (Kursten et al. 2011), and Spain (Torres et al. 2007). Because of understandable conservatism in early studies, C-steel has long been viewed as a material with a relatively short container lifetime (particularly in comparison to the long lifetime for copper UFC) and, hence, has often been proposed for use in sedimentary deposits (Andra 2005, Nagra 2002), where it is believed that the host rock will provide significant containment and retardation of radionuclides. However, with further study, it is now apparent that C-steel containers could have long lifetimes (King 2007) so that their use in more-permeable host rocks would appear to be feasible.

The corrosion behaviour of C-steel UFC has been extensively studied both experimentally and through the study of natural analogs and by mathematical modelling (King 2007). With the exception of the Belgian Supercontainer design which has a cementitious overpack (Kursten et al. 2011), C-steel containers are generally proposed for use with a bentonite buffer surrounding the container. Of any of the various materials proposed for UFC, C-steel is the one that has the greatest potential to impact the properties of the other barriers in the multi-barrier system (King and Padovani 2011). Thus, in addition to understanding the corrosion behaviour of the container material, there has been a lot of effort to understand the impact of the generation and transport of H<sub>2</sub> through compacted bentonite and low-permeability host rock (King 2012) and the interaction between Fe(II) and montmorillonite (Wersin and Snellman 2008).

The Steel Corrosion Model (SCM) was developed to predict the anaerobic corrosion behaviour of C-steel UFC (King and Kolar 2009). Thus, the SCM does not consider corrosion during the aerobic phase of the evolution in the DGR environment and, since localised corrosion and stress corrosion cracking are not considered to be possible under anaerobic conditions, the model is limited to a prediction of the uniform corrosion behaviour of the container. The model is based on the same modelling principles used previously for the Copper Corrosion Model (King et al. 2008, King and Kolar 2000) and the Mixed Potential Model for the dissolution of used fuel (King and Kolar 1999, 2001; Shoosmith et al. 2003). A series of one-dimensional reactive-transport equations are written for the various species included in the model which describe the mass transport, redox reactions, adsorption/desorption, and precipitation/dissolution processes occurring in the near- and far-fields. These equations are solved subject to mathematical boundary conditions, the most important of which are electrochemical expressions that describe the corrosion processes occurring on the container

surface and which permit the prediction of the container lifetime, as well as the time-dependent corrosion rate and corrosion potential ( $E_{\text{CORR}}$ ).

In addition to prediction of the corrosion behaviour of the container, however, the SCM also treats the interaction of corrosion products with other barriers in the system and predicts the overall evolution of the repository environment. An important characteristic of sedimentary host rock is the low hydraulic conductivity which may result in repository saturation times of the order of tens of thousands of years. The effects of this slow saturation process on the corrosion behaviour and on mass transport of species to and from the container are considered in the model. The generation and transport of dissolved and gaseous hydrogen are also treated in the model, as is interaction between dissolved Fe(II) and the bentonite barrier. These interactions may take the form of Fe(II) adsorption, Fe(II)-induced alteration of montmorillonite to a non-smectite type clay, and the loss of porosity as a result of the precipitation of C-steel corrosion products in the bentonite close to the container.

A summary of the model and of the more important processes in the SCM is presented in Section 2, with full details provided by King and Kolar (2009), along with a summary of the underlying assumptions in the model. Two “Base Case” simulations, one each for shale and limestone host rocks, are described in Section 3, along with a number of variant cases performed to assess the sensitivity of the predicted results to the saturation time, the minimum porosity of the precipitated corrosion product and other barriers, and the threshold relative humidity values that control the onset of corrosion. The results of these simulations are presented in Section 4. A comparison of the SCM with other models is presented in Section 5, which also discusses the implications of the simulations for the expected corrosion behaviour of the containers and provides suggestions for further experimental and modelling studies. A complete set of input parameters is provided in Appendix A.

## **2. STEEL CORROSION MODEL VERSION 1.0 (SCM V1.0)**

### **2.1 CORROSION ASPECTS OF THE MODEL**

#### **2.1.1 Reaction Scheme**

The reaction scheme for the SCM V1.0 is shown in Figure 1. This mechanism includes a number of processes of interest for the corrosion of C-steel containers which are described in more detail in the next section. A central feature of this mechanistic description of the corrosion process is that it couples the interfacial corrosion reactions to processes that occur away from the container surface in the buffer material and host rock. In this way, the impact of the evolution of the repository environment on the corrosion behaviour of the container, and vice versa, are implicitly included in the model. The processes occurring in the near field include reversible adsorption/desorption of Fe(II) by bentonite, the irreversible alteration of bentonite (montmorillonite) by reaction with Fe(II), the precipitation and dissolution of solid corrosion products and mineral phases, the generation and transport of H<sub>2</sub> gas, and the transport of dissolved pore water species and corrosion products.

The SCM V1.0 has been developed to account for the anaerobic corrosion of C-steel only. Corrosion during the aerobic and transitional aerobic-anaerobic phases is excluded, as is the impact of remnant corrosion products on the subsequent anaerobic phase. The preceding aerobic and transitional phases are simulated simply by a delay in the onset of the interfacial

electrochemical corrosion reactions, during which the containers cool slightly from their peak temperature.

A total of thirteen chemical species are considered in the model, including: dissolved ferrous chloride ions ( $\text{FeCl}^+$ ), dissolved ferrous-carbonate complexes ( $\text{Fe}(\text{CO}_3)_2^{2-}$ ), dissolved ferrous-hydroxy ion ( $\text{FeOH}^+$ ), dissolved hydrogen ( $\text{H}_2(\text{aq})$ ), dissolved bicarbonate ion ( $\text{HCO}_3^-$ ), dissolved chloride ion ( $\text{Cl}^-$ ), precipitated ferrous hydroxide ( $\text{Fe}(\text{OH})_2$ ), magnetite ( $\text{Fe}_3\text{O}_4$ ), ferrous carbonate ( $\text{FeCO}_3$ ), ferrous ions adsorbed on the clay or host rock minerals ( $\text{Fe}(\text{II})_{\text{ADS}}$ ), dissolved Fe incorporated into altered bentonite clay ( $\text{Fe}(\text{clay})$ ), calcite ( $\text{CaCO}_3$ ), and gaseous hydrogen ( $\text{H}_2(\text{g})$ ). The thirteen species and their notations are listed in Table 1.

**Table 1: Notation for the Thirteen Species Included in the SCM V1.0**

	<b>Notation</b>
<b>Aqueous species</b>	
$\text{FeCl}^+(\text{aq})$	C <sub>1</sub>
$\text{Fe}(\text{CO}_3)_2^{2-}(\text{aq})$	C <sub>2</sub>
$\text{FeOH}^+(\text{aq})$	C <sub>3</sub>
$\text{H}_2(\text{aq})$	C <sub>4</sub>
$\text{HCO}_3^-(\text{aq})$	C <sub>5</sub>
$\text{Cl}^-(\text{aq})$	C <sub>6</sub>
<b>Solid or precipitated species</b>	
$\text{Fe}(\text{OH})_2(\text{s})$	C <sub>7</sub>
$\text{Fe}_3\text{O}_4(\text{s})$	C <sub>8</sub>
$\text{FeCO}_3(\text{s})$	C <sub>9</sub>
$\text{Fe}(\text{II})_{\text{ADS}}$	C <sub>10</sub>
$\text{Fe}(\text{clay})$	C <sub>11</sub>
$\text{CaCO}_3(\text{s})$	C <sub>12</sub>
<b>Gaseous species</b>	
$\text{H}_2(\text{g})$	C <sub>13</sub>

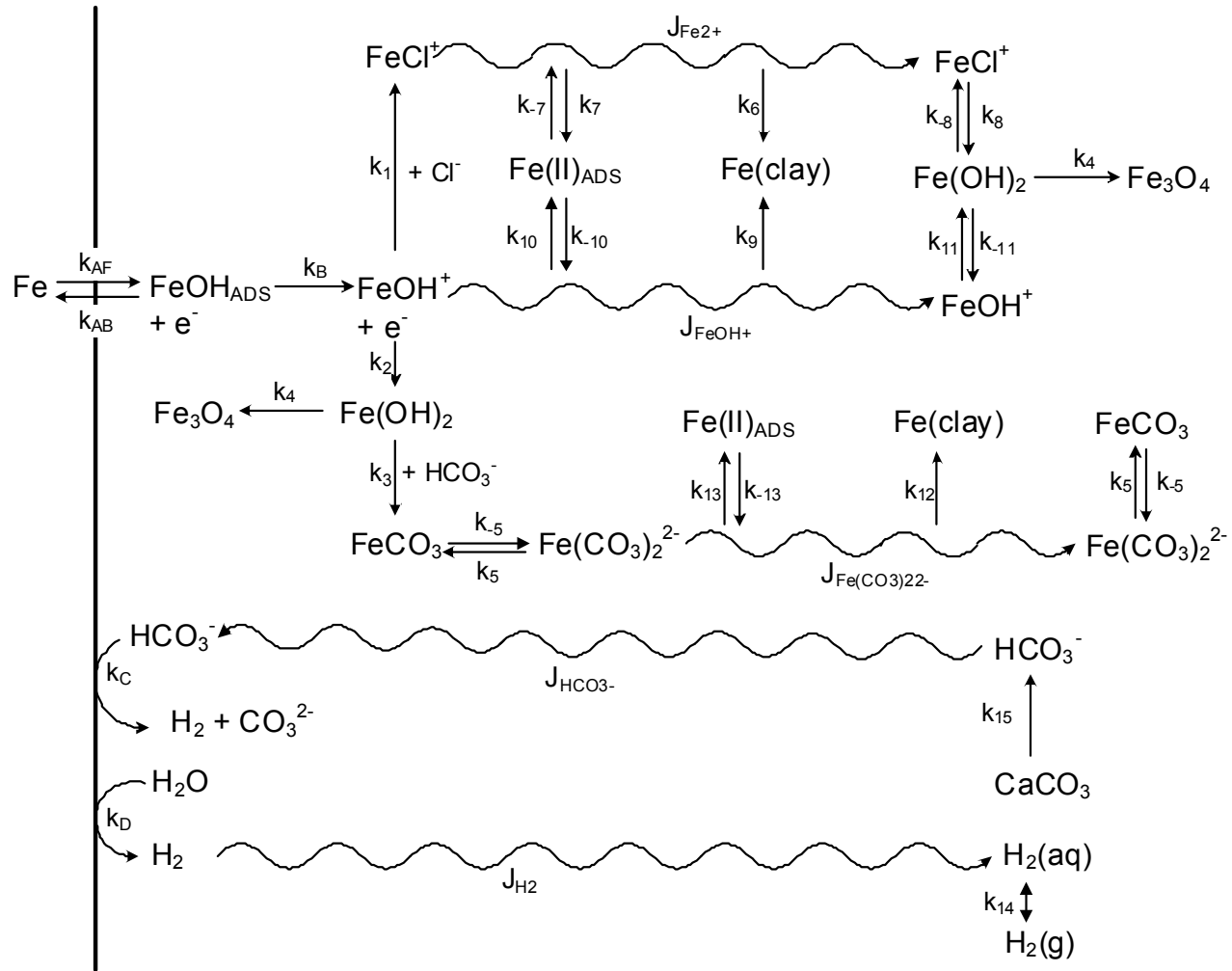


Figure 1: Reaction Scheme for the Steel Corrosion Model Version 1.0 (SCM V1.0)

## 2.1.2 Processes Included in the Model

### 2.1.2.1 Interfacial Electrochemical Processes

The interfacial corrosion reaction is represented in the SCM by a series of anodic and cathodic reactions (King and Kolar 2009). The anodic dissolution of Fe as  $\text{FeOH}^+$



is coupled to the cathodic reduction of  $\text{H}_2\text{O}$



and of  $\text{HCO}_3^-$



The dissolved  $\text{FeOH}^+$  species produced by Reaction (1) can be further transformed into either dissolved  $\text{FeCl}^+$  or precipitated  $\text{Fe}(\text{OH})_2$  (King and Kolar 2009).

### 2.1.2.2 Film Formation

Because of the limited solubility of Fe(II) under DGR conditions, precipitation of solid phases is an important process to include in the SCM. (Any Fe(III) species formed during the aerobic phase are assumed to have been reduced to Fe(II) during the transitional period prior to the development of anaerobic conditions and, hence, are not considered in the SCM V1.0). Precipitation can, in theory, occur anywhere within the repository, but is most likely to occur at the container surface since that is the location of highest Fe(II) concentration.

Three solid Fe(II) corrosion products are considered in the SCM; ferrous hydroxide  $\text{Fe}(\text{OH})_2$ , magnetite  $\text{Fe}_3\text{O}_4$ , and iron carbonate (siderite)  $\text{FeCO}_3$ . Ferrous hydroxide is assumed to be formed at the interface by the hydrolysis of  $\text{FeOH}^+$  ions (rate constant  $k_2$ , Figure 1)



The conversion of  $\text{Fe}(\text{OH})_2$  to  $\text{Fe}_3\text{O}_4$ , via the well-known Schikorr reaction ( $k_4$ , Figure 1)



results in the formation of  $\text{H}_2$  and the mixed Fe(II)/Fe(III) oxide.

In the presence of carbonate (or more likely  $\text{HCO}_3^-$  at the assumed pore-water pH of pH 8), ferrous ions may also precipitate as  $\text{FeCO}_3$  ( $k_3$ ). At high carbonate/bicarbonate concentrations, siderite may dissolve (or re-precipitate) via the soluble  $\text{Fe}(\text{CO}_3)_2^{2-}$  complex ion ( $k_5/k_{-5}$ ).

Each of the solid phases  $\text{Fe}(\text{OH})_2$ ,  $\text{Fe}_3\text{O}_4$ , and  $\text{FeCO}_3$  may precipitate either at the canister surface or anywhere throughout the near and far fields.

An important aspect of the interfacial precipitation of solid Fe(II) phases is that a protective layer of corrosion products is then formed on the container surface. These corrosion products not only limit the transport of corrosion products away from, and of reactants to, the container surface but also serve to physically block the surface from further corrosion. Both of these effects are modelled using the porosity ( $\varepsilon$ ) of the corrosion product layer. The effective diffusivity of dissolved species is proportional to the porosity of the corrosion products. Furthermore, for a network or randomly sized and randomly orientated pores,  $\varepsilon$  is also a measure of the effective surface area of the C-steel surface exposed at the base of the pores, corresponding to the effective surface area for the anodic and cathodic electrochemical reactions (King and Kolar 2001).

The porosity of the corrosion product layer is treated as a parameter within the SCM and is directly computed within the code via

$$\varepsilon_a = \varepsilon_a^{\text{init}} - \frac{M_7}{\rho_7} c_7 - \frac{M_8}{\rho_8} c_8 - \frac{M_9}{\rho_9} c_9 \quad (6)$$

where  $\varepsilon_a$  is the accessible porosity,  $\varepsilon_a^{\text{init}}$  is the initial value at a particular location,  $c$ ,  $M$ , and  $\rho_d$  are the concentration, molecular mass, and density, respectively, and species 7, 8, and 9 are  $\text{Fe}(\text{OH})_2$ ,  $\text{Fe}_3\text{O}_4$ , and  $\text{FeCO}_3$ , respectively. The accessible porosity is spatially dependent, through the spatial (and temporal) dependence on  $c$ , and precipitation could reduce the pore volume anywhere within the near or far field. However, precipitation has the greatest impact when it occurs at the corroding surface. Because the concentration of dissolved Fe(II) is highest at the container surface precipitation can reduce the interfacial porosity  $\varepsilon_0$  (defined as the mean porosity over the first five points of the spatial grid) to zero, resulting in the corrosion rate falling to zero. This situation is unrealistic as protective (as opposed to passive) surface films inevitably retain some porosity, either because film growth occurs at the film/solution interface or because of local acidification in the pores because of the hydrolysis of dissolved metal ions. For this reason, a minimum interfacial porosity  $\varepsilon_{\text{MIN}}$  is used in the code to simulate the inherent porosity of the protective surface film.

### 2.1.2.3 Interaction Between Fe(II) and Bentonite

Ferrous corrosion products are assumed to interact with the bentonite clay by ion exchange and by alteration of montmorillonite to either a non-swelling clay or an Fe-rich smectite (Wersin et al. 2007). The treatment of the ion-exchange reaction between Fe(II) and bentonite is described by a reversible process assuming a Langmuir adsorption isotherm (King and Kolar 2009) in a similar fashion to the sorption of copper in the Copper Corrosion Model (King et al. 2008) and is not discussed further here.

The literature is by no means consistent on the subject of the transformation of montmorillonite and there is a lack of mechanistic understanding of the process. Wersin et al. (2007) used data for the rate of montmorillonite dissolution to predict the extent of clay alteration due to the corrosion of the steel shell of a KBS-3H supercontainer. Implicit in this treatment is that the rate of montmorillonite transformation is controlled by the initial dissolution step and that the subsequent precipitation of either an Fe-rich smectite or a non-swelling clay such as berthierine or chlorite is fast. In the absence of more-specific mechanistic information, a similar approach is used here.

Kinetic data for the dissolution of montmorillonite were taken from the compilation of Palandri and Kharaka (2004), as was done by Wersin et al. (2007). Dissolution rates are reported in units of  $\text{mol}\cdot\text{m}^{-2}\cdot\text{s}^{-1}$  and were converted to the required units of  $\text{mol}\cdot\text{dm}^{-3}\cdot\text{s}^{-1}$  based on an assumed specific surface area of montmorillonite of  $37.5 \text{ m}^2\cdot\text{g}^{-1}$  and a dry density of  $1.65 \text{ Mg}\cdot\text{m}^{-3}$ . The rate expression for the transformation of montmorillonite by reaction with  $\text{FeCl}^+$  (species 1, rate constant  $k_6$ ),  $\text{Fe}(\text{CO}_3)_2^{2-}$  (species 2, rate constant  $k_{12}$ ), and  $\text{FeOH}^+$  (species 3, rate constant  $k_9$ ) is given by

$$\rho_d \frac{\partial c_{11}}{\partial t} = \varepsilon_a S (k_6 c_1 + k_9 c_3 + k_{12} c_2) \quad (7)$$

where species 11 (concentration  $c_{11}$ ) is the altered clay,  $\rho_d$  is the bentonite dry density, and  $\varepsilon_a$  is the accessible porosity. The corresponding loss terms for  $c_1$ ,  $c_2$ , and  $c_3$  are given by

$$\frac{\partial c_1}{\partial t} = -1.7k_6 c_1; \quad \frac{\partial c_2}{\partial t} = -1.7k_{12} c_2; \quad \text{and} \quad \frac{\partial c_3}{\partial t} = -1.7k_9 c_3 \quad (8)$$

where the 1.7 term accounts for the fact that 1.7 moles of Fe(II) are required to convert one mole of montmorillonite to one mole of berthierine, the assumed transformation product.

#### 2.2.2.4 Gas Generation and Transport

Hydrogen generation and transport is a major issue with the use C-steel containers. Because the rate of diffusion of dissolved  $\text{H}_2$  in highly compacted bentonite is small (equivalent to a corrosion rate of the order of  $1\text{-}10 \text{ nm}\cdot\text{a}^{-1}$ ), it is likely that a  $\text{H}_2$  gas phase will form at some stage during the anaerobic phase. Formation of  $\text{H}_2$  at too high a rate may result in irreversible changes to the bentonite or host rock (Nagra 2004). Based on work by Nagra, the anaerobic corrosion rate at which  $\text{H}_2$  can be transported away from the container without causing irreversible damage to the bentonite or host rock is of the order of  $10 \text{ }\mu\text{m}\cdot\text{a}^{-1}$ .

Both hydrogen generation and transport are treated in the SCM V1.0, although detailed treatment of gas transport by two-phase flow and the dilation of transport pathways is not included in the model. Hydrogen generation is predicted based on the interfacial cathodic processes (Reactions (2) and (3)), the rates of which are determined in the model. Hydrogen transport is modelled as a diffusion process and is assumed to occur both in the saturated phase (dissolved  $\text{H}_2$ ) and in the unsaturated phase (gaseous  $\text{H}_2$ ). When the pressure of  $\text{H}_2$  in the unsaturated phase exceeds the breakthrough pressure gas is assumed to be lost from the system and the pressure released.

#### 2.2.2.5 Unsaturated Conditions

A characteristic of a repository in sedimentary host rock in Southern Ontario is that there is likely to be an extended saturation period, possibly of the order of tens of thousands of years (G. Kwong, private communication 2010). The degree of saturation of the bentonite and host rock affects a number of processes in the model, including:

- the thermal conductivity of the buffer and rock and, hence, the spatial- and temporal-dependence of the temperature within the repository,
- the diffusive mass transport of dissolved and, especially, of gaseous species to and from the UFC surface,
- the change in concentration of dissolved species as a consequence of the change in volume of pore solution,
- the increase in pore-water Cl<sup>-</sup> concentration and the total amount of Cl<sup>-</sup> as the bentonite is saturated by incoming pore fluids from the host rock,
- the propensity for the precipitation of solid corrosion products, and
- the effect of the interfacial moisture content on the rate of electrochemical processes.

In the SCM V1.0, the temporal- and spatial-dependence of the degree of saturation ( $S(x,t)$ ) is treated as an input parameter, as described in more detail below.

Certain aspects of the effect of unsaturated conditions on the thermal profiles in the repository are simulated in the SCM V1.0. The thermal conductivity of the bentonite is a function of the moisture content (or degree of saturation), as shown in Figure A-1. However, because the host rock is assumed to be largely saturated at all times (except for the excavation damaged zone EDZ), the thermal conductivity of the shale or limestone host rock is treated as a constant and equivalent to that for the saturated formation. The specific heat of each material is also a function of the degree of saturation, which is calculated explicitly within the code based on the values for the solid particles (an input parameter) and of the aqueous phase, as well as  $S(x,t)$ . The subsequent effects on time-dependent container surface and far-field temperatures are not treated in the model since these temperatures are pre-defined as boundary conditions for the solution of the heat-conduction equation.

The effect of  $S$  on the diffusivity of gaseous and dissolved species is treated in the model using saturation-dependent effective diffusion coefficients. For dissolved species, the effective diffusion coefficient ( $D_{\text{eff}}$ ) is given by (King et al. 1996)

$$D_{\text{eff}} = \tau_f \epsilon_e S D_i \quad (9)$$

where  $\tau_f$  is the tortuosity factor,  $\epsilon_e$  is the effective porosity for diffusive mass transport, and  $D_i$  is the diffusivity of species  $i$  in bulk solution. The only gaseous species included in the SCM V1.0 is  $H_2$ , for which the effective diffusivity is given by

$$D_{\text{eff}} = \tau_f \epsilon_e (1 - S)^3 D_g \quad (10)$$

where  $D_g$  is the gas-phase diffusion coefficient and the  $(1 - S)^3$  term is based on the dependence of the diffusion coefficient of  $O_2$  on  $S$  in unsaturated soils (Collin and Rasmuson 1988).

Various effects of saturation on the concentration of chemical species are included in the model. Based on the principle of the conservation of mass, the concentration of dissolved species increases or decreases as the degree of saturation decreases or increases, respectively. For Cl<sup>-</sup> ions only, the concentration in the bentonite pore water increases, as does the total Cl<sup>-</sup> inventory, as the overall degree of saturation of the bentonite increases due to the ingress of saline pore fluids from the host rock. Finally, there is a greater tendency for certain species to precipitate (or dissolve) as the concentration of dissolved species increases (or decreases) in response to changes in  $S$ .

Because electrochemical corrosion reactions require the presence of an aqueous phase or, as a minimum, a thin surface liquid film, corrosion may not be possible in compacted bentonite at low moisture contents. To account for this phenomenon, the interfacial rate constants for the various interfacial processes considered in the model are assumed to depend on the surface moisture content  $h_k$  as follows:

$$\begin{aligned}
 k_i &= 0 & \text{for} & \quad h_k \leq h_{k,\min} \\
 k_i &= \frac{h_k - h_{k,\min}}{h_{k,\max} - h_{k,\min}} k_{i,\max} & \text{for} & \quad h_{k,\min} < h_k < h_{k,\max} ; \quad i = A, C, D \\
 k_i &= k_{i,\max} & \text{for} & \quad h_k \geq h_{k,\max}
 \end{aligned} \tag{11}$$

where  $k_{i,\max}$  is the maximum value of the respective rate constant corresponding to fully saturated conditions, and  $h_{k,\min}$  and  $h_{k,\max}$  are the values of  $h_k$  between which  $k_i$  grows linearly from 0 to its maximum value. The values of  $h_{k,\min}$  and  $h_{k,\max}$  are defined by the threshold relative humidity for atmospheric corrosion (60-70% RH), and correspond to the relative humidity below which there is insufficient surface water to support electrochemical processes (Shreir et al. 1993). In Equation (11), the rate constant  $k_A$  is equal to the combined rate constant  $k_{AF}k_B/k_{AB}$ , where all of the rate constants are noted in Figure 1.

As noted above, the spatial and temporal distribution of the degree of saturation is treated as an input parameter in the SCM V1.0. The initial  $S$  of the pre-compacted bentonite blocks and bentonite pellets in the disposal tunnel are 0.65 and 0.06, respectively, giving a volume-averaged degree of saturation of 0.10. It is reasonable to expect that the EDZ will be unsaturated initially due to evaporation of pore fluids during the operational phase, although the host rock in the far field is likely to be saturated. Evidence from large-scale heater tests in hard rock laboratories (Graham et al. 1997, Karnland et al. 2000) suggests that the moisture initially in the bentonite is re-distributed under the action of the thermal gradient produced by the container but that water is not lost from the deposition hole. The saturation time for the repository is a function of the initial moisture content and the competing effects of water movement away from the container down the thermal gradient and the ingress of water due to the hydraulic gradient from the host rock. Because of the low hydraulic conductivity of sedimentary deposits and, in part, because of the low initial moisture content of the repository, it is expected that the saturation time will be of the order of tens of thousands of years.

As discussed in more detail below, a total of five mass-transport barriers or layers are simulated in the SCM V1.0, three layers of compacted bentonite, the EDZ, and a layer representing the host rock. The bentonite buffer is sub-divided into three layers in order to better represent the spatial variation of the degree of saturation. The parameter  $S$  is treated as a layer-dependent parameter in the model whose value is spatially uniform within a given layer.

Figure 2 shows the time-dependent distribution of  $S$  for the five layers in the model. Complete saturation is assumed to occur after 10,000 a for the Base Case simulation as shown in the figure. Figure 3 shows the time-dependent distribution of  $S$  over the first 1000 a. The initial moisture content of the bentonite is assumed to be re-distributed through the three layers representing the buffer for the first 500 a, after which the buffer moisture content is assumed to increase linearly with time until full saturation after 10,000 a. (Full saturation is defined as corresponding to  $S = 0.99$  to allow for the continued accumulation and release of gaseous  $H_2$ ).

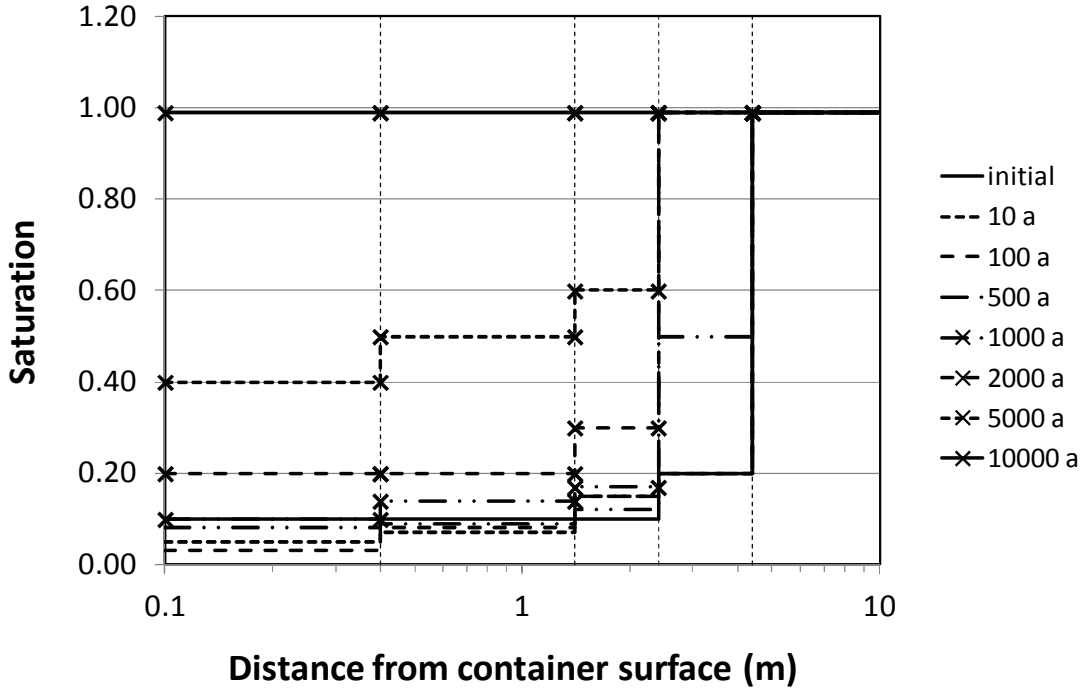


Figure 2: Assumed Time Dependence of the Degree of Saturation for the SCM V1.0 Base Case Simulation. From the left to right, the five layers (separated by the dashed vertical lines) are the three layers of compacted bentonite, the EDZ, and the host rock

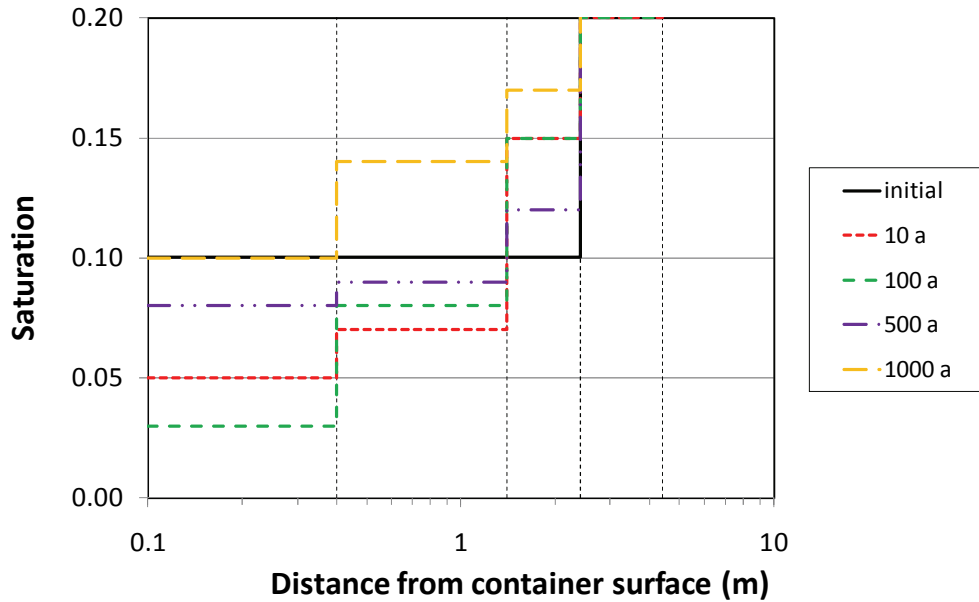


Figure 3: Assumed Time Dependence of the Degree of Saturation for the SCM V1.0 Base Case Simulation for a Period of One Thousand Years Following Repository Closure. From the left to right, the five layers (separated by the dashed vertical lines) are the three layers of compacted bentonite, the EDZ, and the host rock

Thus, the saturation of the two sub-layers of bentonite closest to the container is assumed to decrease for a period of 100 a, with the outermost bentonite sub-layer becoming wetter. After 100 a, by which time the thermal gradient is expected to have diminished, the saturation of all three buffer sub-layers increases with time as the bentonite slowly saturates with incoming pore water from the host rock. During this period, the degree of saturation of the EDZ is assumed to remain at the initial value of 0.2 for 500 a, after which it increases and becomes fully saturated after 1000 a. The host rock is assumed to be saturated at all times.

Because of the current uncertainty in the saturation time, a number of variants involving slower or faster saturation are also considered (Section 3.2.2).

## 2.2 MATHEMATICAL ASPECTS

### 2.2.1 Mass-balance Equations

The mass-balance equations for the thirteen chemical species in the model are:

$$\frac{\partial(\varepsilon_a S c_1)}{\partial t} = \frac{\partial}{\partial x} \left( \tau_f \varepsilon_e S D_1 \frac{\partial c_1}{\partial x} \right) + \varepsilon_a S \left( k_1 c_3 c_6 - 1.7 k_6 c_1 - k_7 c_1 (c_{10}^{\max} - c_{10}) \rho_d + k_{-7} c_{10} \rho_d - k_8 \max(0, c_1 - c_1^{\text{sat}}) \right) + k_{-8} c_7 \quad (12a)$$

$$\frac{\partial(\varepsilon_a S c_2)}{\partial t} = \frac{\partial}{\partial x} \left( \tau_f \varepsilon_e S D_2 \frac{\partial c_2}{\partial x} \right) + \varepsilon_a S \left( -1.7 k_{12} c_2 - k_{13} c_2 (c_{10}^{\max} - c_{10}) \rho_d + k_{-13} c_5 c_{10} \rho_d - k_5 \max(0, c_2 - c_2^{\text{sat}}) \right) + k_{-5} c_5 c_9 \quad (12b)$$

$$\frac{\partial(\varepsilon_a S c_3)}{\partial t} = \frac{\partial}{\partial x} \left( \tau_f \varepsilon_e S D_3 \frac{\partial c_3}{\partial x} \right) + \varepsilon_a S \left( -k_1 c_3 c_6 - k_2 c_3 - 1.7 k_9 c_3 - k_{10} c_3 (c_{10}^{\max} - c_{10}) \rho_d + k_{-10} c_{10} \rho_d - k_{11} \max(0, c_3 - c_3^{\text{sat}}) \right) + k_{-11} c_7 \quad (12c)$$

$$\frac{\partial(\varepsilon_a S c_4)}{\partial t} = \frac{\partial}{\partial x} \left( \tau_f \varepsilon_e S D_4 \frac{\partial c_4}{\partial x} \right) + R_H + k_4 c_7 \quad (12d)$$

$$\frac{\partial(\varepsilon_a S c_5)}{\partial t} = \frac{\partial}{\partial x} \left( \tau_f \varepsilon_e S D_5 \frac{\partial c_5}{\partial x} \right) + \varepsilon_a S \left( k_5 \max(0, c_2 - c_2^{\text{sat}}) + 2k_{12} c_2 + 2k_{13} c_2 (c_{10}^{\max} - c_{10}) \rho_d - 2k_{-13} c_5 c_{10} \rho_d - k_3 c_5 c_7 - k_{-5} c_5 c_9 + k_{15} \max(0, c_5^{\text{sat}} - c_5) c_{12} \right) \quad (12e)$$

$$\frac{\partial(\varepsilon_a S c_6)}{\partial t} = \frac{\partial}{\partial x} \left( \tau_f \varepsilon_e S D_6 \frac{\partial c_6}{\partial x} \right) + \varepsilon_a S \left( -k_1 c_3 c_6 + k_6 c_1 + k_7 c_1 (c_{10}^{\max} - c_{10}) \rho_d - k_{-7} c_{10} \rho_d + k_8 \max(0, c_1 - c_1^{\text{sat}}) \right) - k_{-8} c_7 \quad (12f)$$

$$\frac{\partial c_7}{\partial t} = \varepsilon_a S \left( k_2 c_3 + k_8 \max(0, c_1 - c_1^{\text{sat}}) + k_{11} \max(0, c_3 - c_3^{\text{sat}}) \right) - k_3 c_5 c_7 - 3k_4 c_7 - k_{-8} c_7 - k_{-11} c_7 \quad (12g)$$

$$\frac{\partial c_8}{\partial t} = k_4 c_7 \quad (12h)$$

$$\frac{\partial c_9}{\partial t} = \varepsilon_a S k_5 \max(0, c_2 - c_2^{\text{sat}}) + k_3 c_5 c_7 - k_{-5} c_5 c_9 \quad (12i)$$

$$\rho_d \frac{\partial c_{10}}{\partial t} = \varepsilon_a S \rho_d (k_7 c_1 (c_{10}^{\text{max}} - c_{10}) - k_{-7} c_{10} + k_{10} c_3 (c_{10}^{\text{max}} - c_{10}) - k_{-10} c_{10} + k_{13} c_2 (c_{10}^{\text{max}} - c_{10}) - k_{-13} c_5 c_{10}) \quad (12j)$$

$$\rho_d \frac{\partial c_{11}}{\partial t} = \varepsilon_a S (k_6 c_1 + k_9 c_3 + k_{12} c_2) \quad (12k)$$

$$\frac{\partial c_{12}}{\partial t} = -k_{15} \max(0, c_5^{\text{sat}} - c_5) c_{12} \quad (12l)$$

and

$$\frac{\partial((1-S)\varepsilon_a c_{13})}{\partial t} = \frac{\partial}{\partial x} \left( \tau_f \varepsilon_e (1-S)^3 D_{13} \frac{\partial c_{13}}{\partial x} \right) - R_H \quad (12m)$$

These mass-balance equations differ slightly from those given in the SCM theory manual (King and Kolar 2009). These differences are the result of treating the alteration of the bentonite by reaction with  $\text{FeCl}^+$  (rate constant  $k_6$ ),  $\text{FeOH}^+$  ( $k_9$ ), and  $\text{Fe}(\text{CO}_3)_2^{2-}$  ( $k_{12}$ ) as a zero-order reaction in which the rate-controlling step is the dissolution of montmorillonite, resulting in a change in the mass-balance equation for  $\text{FeCl}^+$  (species 1),  $\text{Fe}(\text{CO}_3)_2^{2-}$  (species 2),  $\text{FeOH}^+$  (species 3), and the altered clay (species 11). In addition, based on evidence from the literature (Langmuir 1997), the dissolution of  $\text{CaCO}_3$  (rate constant  $k_{15}$ ) is also treated as a zero-order reaction, resulting in a change in the mass-balance equation for  $\text{HCO}_3^-$  (species 5) and  $\text{CaCO}_3$  (species 12).

The reaction rate  $R_H$  between dissolved and gaseous  $\text{H}_2$  is assumed to be fast so that equilibrium can be assumed

$$c_{13} = \tilde{H} c_4 \quad (12n)$$

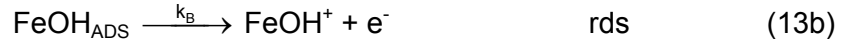
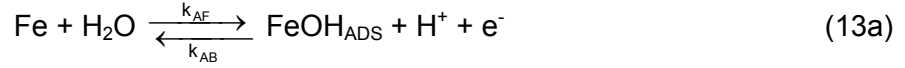
where  $\tilde{H}$  is the inverse Henry's law constant. This relation reduces the number of independent variables by one, and we can combine Equations (12d) and (12m) into a single equation for  $c_4$ :

$$\frac{\partial}{\partial t} \left( \varepsilon [S + (1-S)\tilde{H}] c_4 \right) = \frac{\partial}{\partial x} \left( \tau_f \varepsilon_e [S D_4 + (1-S)^3 D_{13} \tilde{H}] \frac{\partial c_4}{\partial x} \right) + k_4 c_7 \quad (12o)$$

Equations (12a-c), (12e-l), and (12o) are solved for the respective concentrations of the different species, with  $c_{13}$  subsequently calculated using Equation (12n).

## 2.2.2 Boundary Conditions

The anodic dissolution of C-steel is represented in the SCM by the following reaction scheme (Figure 1):

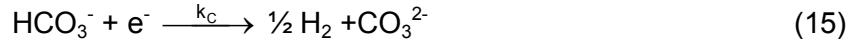


At steady-state, the current density (i)-potential (E) relationship for Reaction (13) is given by

$$\frac{i_A}{F} = \varepsilon_0 n_B \frac{k_{AF} k_B}{k_{AB}} \exp\left\{\frac{(1 + \alpha_B)F}{RT} (E - E^0)\right\} = \varepsilon_0 n_B k_A \exp\left\{\frac{\alpha_A F}{RT} (E - E_A^0)\right\} \quad (14)$$

where  $k_{AF}$ ,  $k_{AB}$ , and  $k_B$  are the interfacial electrochemical rate constants as defined by Equations (13a) and (13b),  $n_B$  and  $\alpha_B$  are the number of electrons transferred and the transfer coefficient for the rate-determining step (rds) Reaction (13b), F, R, and T are the Faraday constant, gas constant, and absolute temperature, respectively, and  $E_B^0$  is the standard potential.

Two possible reactions are considered for the accompanying cathodic process, the evolution of  $\text{H}_2$ . The reduction of bicarbonate ions ( $\text{HCO}_3^-$ ) is possible in carbonate-containing environments, via the reaction



for which the i-E relationship is

$$\frac{i_C}{F} = -\varepsilon_0 n_C k_C [\text{HCO}_3^-]_0 \exp\left\{-\frac{\alpha_C F}{RT} (E - E_C^0)\right\} \quad (16)$$

where  $[\text{HCO}_3^-]_0$  is the interfacial concentration of  $\text{HCO}_3^-$  ions and the other symbols have an analogous meaning to those for Equation (14).

The direct reduction of  $\text{H}_2\text{O}$  is also possible, via



for which the i-E relationship is

$$\frac{i_D}{F} = -\varepsilon_0 n_D k_D \exp\left\{-\frac{\alpha_D F}{RT} (E - E_D^0)\right\} \quad (18)$$

The reduction of  $\text{H}^+$  is another possible cathodic reaction, but is not specifically considered in the SCM as the concentration of  $\text{H}^+$  ions is low at the assumed pH of the system of pH 7.5-8. Any  $\text{H}^+$  reduction is effectively included in Reaction (17).

At the corrosion potential ( $E_{\text{CORR}}$ ), the sum of the anodic and cathodic currents (and, for a uniformly corroding surface, the current densities) is equal to zero

$$i_A + i_C + i_D = 0 \quad (19)$$

with this equality serving as an additional left-hand bc. At  $E_{\text{CORR}}$ , the anodic current density equals the corrosion current density  $i_{\text{CORR}}$ .

The electrochemical current densities are also equal to the interfacial diffusive fluxes of the respective dissolved reactants and products. Thus,

$$i_A = -n_A F S \tau_f \varepsilon_e D_3 \frac{\partial c_3}{\partial x} \quad (20)$$

$$i_C = -n_C F S \tau_f \varepsilon_e D_5 \frac{\partial c_5}{\partial x} \quad (21)$$

and

$$\frac{i_C}{n_C} + \frac{i_D}{n_D} = F S \tau_f \varepsilon_e D_4 \frac{\partial c_4}{\partial x} \quad (22)$$

### 2.2.3 Model Geometry

Since the SCM V1.0 code is a 1-D model, the complex 3-D geometry of the actual repository must be transformed into a one-dimensional representation for modelling purposes. As for the copper corrosion model developed previously (King et al. 2008, King and Kolar 2000), the various mass-transport barriers in the near- and far-fields are represented by a series of layers of varying width and unit cross-sectional area. In the current model, these layers represent (i) the bentonite buffer material directly in contact with the container, (ii) the excavation-damaged zone (EDZ) around the periphery of the tunnel, and (iii) the host rock itself.

The cross-sectional and longitudinal section views for the in-room repository design are shown in Figures 4 and 5, respectively. The C-steel containers (1195 mm diameter, 3.88 m length) are placed on a highly compacted bentonite (HCB) pedestal and the remainder of the 2.5-m-diameter tunnel filled with bentonite pellets. The containers are spaced on 8-m centres along the length of the placement tunnel. The as-placed dry density and saturation are  $1610 \text{ kg}\cdot\text{m}^{-3}$  and 65% and  $1410 \text{ kg}\cdot\text{m}^{-3}$  and 6% for the HCB and bentonite pellets, respectively (NWMO 2011).

Because the 1-D SCM V1.0 cannot simulate the spatially variable properties of the HCB and bentonite pellets, volume-averaged buffer properties are used in the model. The volumes of HCB and bentonite pellets in an 8-m-long section of placement tunnel are  $2.38 \text{ m}^3$  and  $32.54 \text{ m}^3$ , respectively. The volume averaged as-placed dry density and initial saturation are, therefore,  $1424 \text{ kg}\cdot\text{m}^{-3}$  and 10%, respectively. (The input parameter used in the code is the total porosity, rather than the dry density, which corresponds to 0.48 on a volume-averaged basis, Appendix A.2).

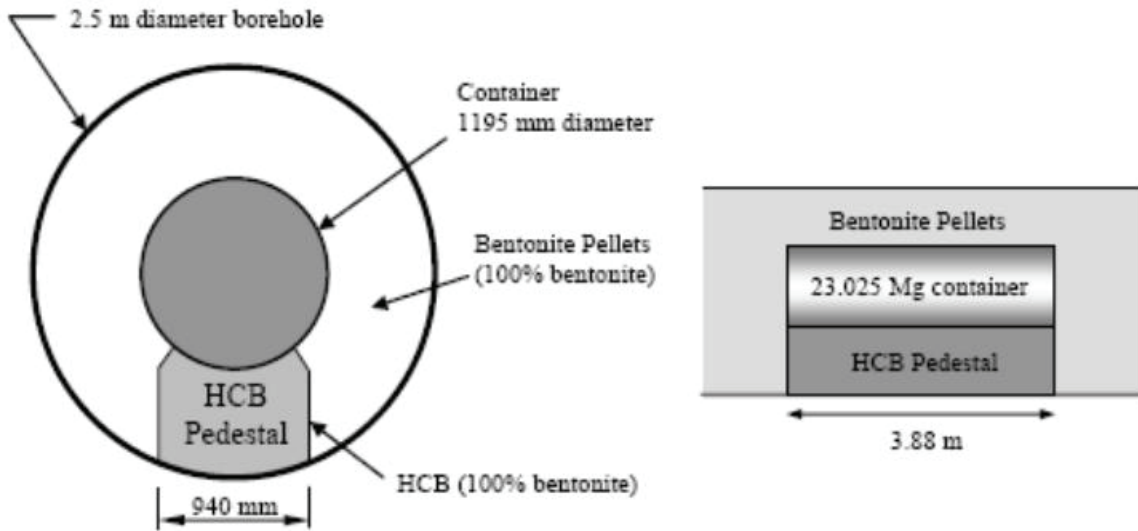


**Figure 4: Cross-sectional Views of the In-room Disposal Repository Design (NWMO 2011)**

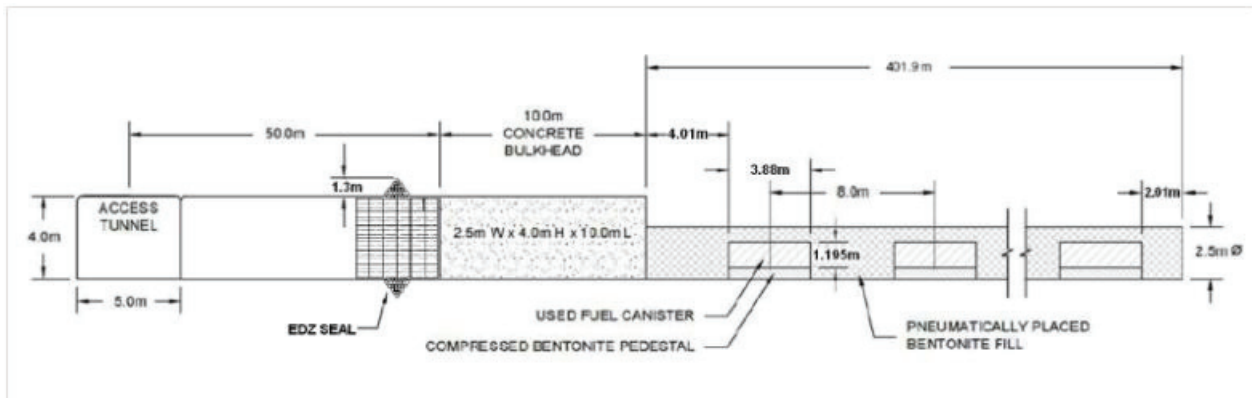


**Figure 5: Placement Room Longitudinal Section (NWMO 2011)**

In common with the earlier copper corrosion models, the thickness of the buffer material is determined by the bentonite volume:container surface area ratio. This protocol was developed in order to properly account for all of the initially trapped  $O_2$  in the buffer material. Although this is of less importance for the SCM V1.0 as the model accounts for anaerobic corrosion only, the same procedure has been retained here. The total bentonite thickness, is therefore, 2.4 m (Appendix A.2). In order to simulate the spatial (and temporal) distribution of the degree of saturation of the bentonite, the buffer layer is divided into three sub-layers of thickness 0.4 m, 1.0 m, and 1.0 m (from the surface of the containers outwards). This division is arbitrary, except that the layer of buffer closest to the container is thinner as the moisture content gradients tend to be steeper closest to the container surface. Figure 6 shows a schematic of the 1-D geometry used for the SCM V1.0 simulations.

The thicknesses of the EDZ and host rock layers in the model are determined by the repository and site characteristics. The EDZ layer thickness is defined as 2.0 m based on Nagra (2002). The thickness of the host rock layer is defined as 30 m based on the assumption of a 60-70-m-thick sedimentary horizon in which the repository is located and the assumption that the adjacent sedimentary horizon exhibits a higher hydraulic conductivity.

The only other “layer” included in the model simulates the porous corrosion product ( $\text{Fe}_3\text{O}_4$ ) that precipitates on the container surface (Figure 6). The thickness of this layer is not formally defined in the model. Instead, it is assumed that a layer of mixed corrosion product and bentonite forms (referred to as a “transformed” layer in the French program (Féron et al. 2009; Neff et al. 2005, 2006)), the thickness of which is defined by the spatial (and temporal) variation in the porosity of the bentonite which is calculated within the code.

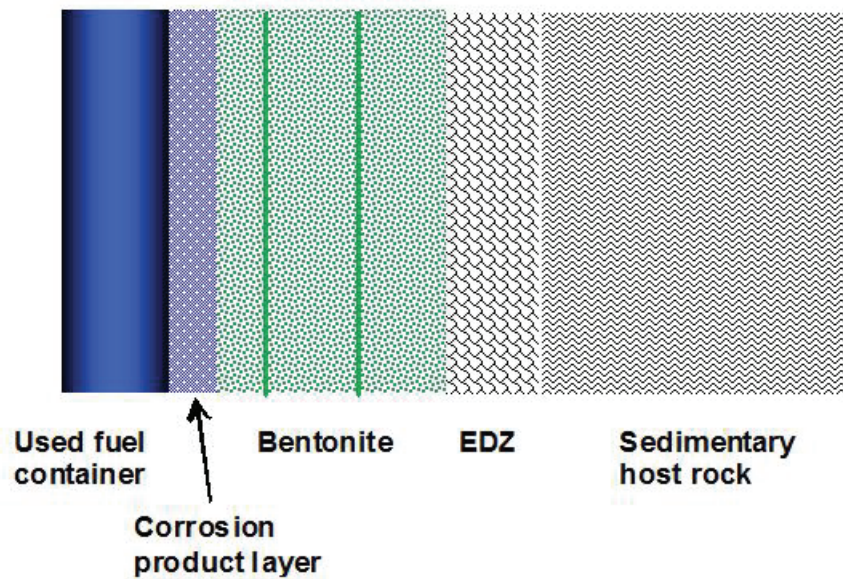


**Figure 6: Series of Mass-transport Layers Used for the SCM V1.0 Geometry**

The container will most likely fail as a result of mechanical overload once the wall thickness has been reduced by corrosion. The corrosion allowance is a design parameter that has yet to be defined. Here, “lifetimes” are calculated for corrosion allowances of between 1 cm and 10 cm, with a value of 2 cm taken as a reference value in this study to compare the effect of varying input parameters as part of a sensitivity analysis. Calculations are continued until the entire container wall (assumed here to be 10 cm thick) has been consumed by corrosion.

### **2.3 ASSUMPTIONS**

The major assumptions underlying the SCM V1.0 are summarised in Table 2 along with a discussion of their implications and validity.

**Table 2: List of Assumptions for the SCM V1.0**

<b>Assumption</b>	<b>Comments</b>
The reaction scheme in Figure 1 adequately represents the anaerobic corrosion behaviour of C-steel UFC.	The reaction scheme includes 13 species and incorporates all relevant processes of interest for the anaerobic corrosion of C-steel UFC, including interaction of Fe(II) with bentonite and the generation and release of H <sub>2</sub> . The selection of dissolved Fe(II) species is appropriate for the expected repository and host rock environments.
There is no effect of a pre-existing corrosion product film.	An Fe(III)-rich corrosion product film will be formed during the initial aerobic phase, comprising various forms of FeOOH (goethite, lepidocrocite) and green rust. As the repository environment becomes anoxic, it is expected that this film will undergo auto-reductive dissolution, in which reduction of the Fe(III) species in the film is coupled to oxidation of the underlying steel. At the start of the anaerobic period, therefore, there is likely to be a pre-existing film comprising a porous layer of Fe(II) corrosion products (and, possibly, Fe <sub>3</sub> O <sub>4</sub> ). This pre-existing film will have the same effects on the corrosion behaviour as the porous film that develops due to anaerobic corrosion. If the major function of this film is to block surface sites then, as soon as the initial anaerobic corrosion film is deposited, there will be no impact of not considering the pre-existing film. However, if the major effect of the corrosion product film is to restrict mass transport of species towards or away from the surface then not considering the pre-existing film will underestimate the total thickness of the film and, hence, overestimate the corrosion rate.
Mass transport occurs by diffusion only.	Given the low hydraulic conductivity of both the highly compacted bentonite surrounding the container and that expected in the host rock (King 2005), the assumption of diffusive transport only is reasonable.
The repository sealing materials and host rock can be treated as equivalent porous media.	Neither the bentonite-based sealing materials nor the host rock are expected to exhibit discrete fractures. Therefore, their treatment as equivalent porous media is appropriate.
Pore water pH is constant in the range pH 7-9.	This assumption is reasonable provided CaCO <sub>3</sub> is present in the buffer and host rock. However, if the carbonate in the system is converted to FeCO <sub>3</sub> then the pore-water pH will no longer be buffered. It is unlikely that all calcite in the system will be consumed, although local depletion in the buffer material may be possible.

continued ....

**Table 2: List of Assumptions for the SCM V1.0 (continued)**

<b>Assumption</b>	<b>Comments</b>
There is a minimum porosity for the precipitated corrosion product layer.	The assumption of a minimum porosity for the corrosion product layer, especially at the interface, is consistent with local acidification inside the pores of the deposit (e.g., due to the hydrolysis of dissolved Fe(II) species). Local acidification, in turn, is consistent with the constant long-term corrosion typically observed experimentally (King 2008). If there was no minimum interfacial porosity, the corrosion rate would drop to zero as the entire interface became blocked by precipitate, which is inconsistent with experimental evidence.
Reference corrosion allowance of 2 cm	The corrosion allowance is a design parameter that has yet to be defined. Container lifetimes are given for assumed corrosion allowances of between 1 cm and 10 cm, with a value of 2 cm used as a reference in this study for the purpose of sensitivity analyses.
Maximum surface temperature of container will be 120°C.	Through a combination of UFC spacing and repository design, it is assumed that the maximum container temperature will be 120°C. This temperature limit precludes thermal alteration of bentonite, so that the design properties of the bentonite or bentonite/sand buffer can be assumed.

### 3. SIMULATIONS PERFORMED USING SCM V1.0

#### 3.1 BASE CASE SIMULATIONS

Two Base Case simulations were performed, one for shale and one for limestone host rock. The choice of host rock affects the thermal properties (the specific heat and thermal conductivity), mass-transport properties (effective and storage porosities), and the initial calcite  $\text{CaCO}_3$  content of that layer. The layer-dependent properties for the Base Case simulations for shale and limestone are shown in Tables 3(a) and 3(b), respectively. Descriptions of the basis for these values, along with the respective sources, are given in Appendix A.2.

As noted in Section 2.2.2.5, the saturation period for the Base Case simulations is assumed to be 10,000 a. Figure 7 shows the temporal variation in the degree of saturation for the various layers considered in the model.

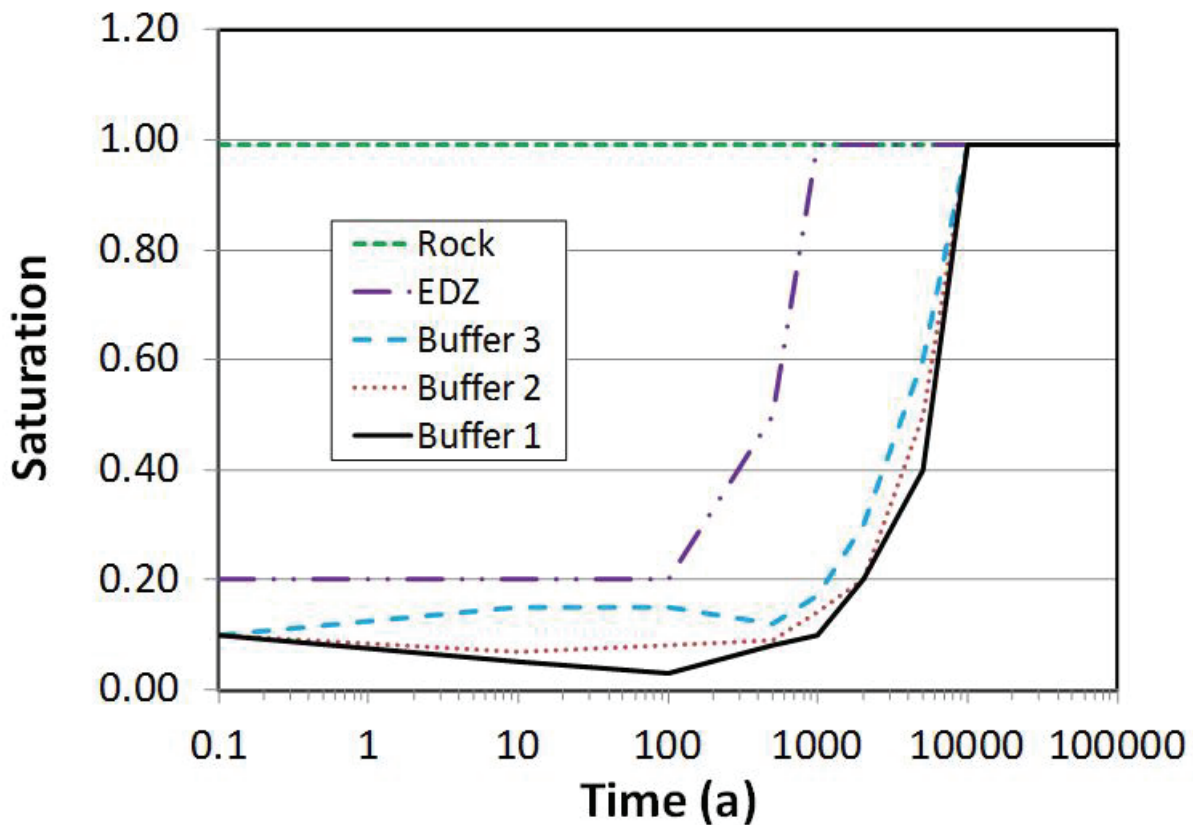


Figure 7: Temporal Variation of the Degree of Saturation in the Various Layers for the Base Case SCM V1.0 Simulations

**Table 3: Layer-dependent Properties for the Base Case Simulations**

**(a) Shale Host Rock**

	<b>Units</b>	<b>Layer 1 Buffer 1</b>	<b>Layer 2 Buffer 2</b>	<b>Layer 3 Buffer 3</b>	<b>Layer 4 EDZ</b>	<b>Layer 5 Shale</b>
Length of layer	dm	4	10	10	20	300
Effective diffusion porosity	-	0.24	0.24	0.24	0.11	0.055
Storage porosity	-	0.24	0.24	0.24	0.11	0.055
Non-accessible porosity	-	0	0	0	0	0
Tortuosity factor	-	0.05	0.05	0.05	0.05	0.05
(Particle) density	kg·dm <sup>-3</sup>	2.7	2.7	2.7	2.6	2.6
Sorption capacity for Fe(II)	mol·kg <sup>-1</sup>	0.4	0.4	0.4	0.2	0.2
Initial HCO <sub>3</sub> <sup>-</sup> concentration	mol·dm <sup>-3</sup>	0.001	0.001	0.001	0.001	0.001
Initial Cl <sup>-</sup> concentration	mol·dm <sup>-3</sup>	0.015	0.015	0.015	4.75	4.75
Initial CaCO <sub>3</sub> concentration	mol·dm <sup>-3</sup>	0.28	0.28	0.28	2.6	2.6
Thermal conductivity	W·K <sup>-1</sup> ·dm <sup>-1</sup>	f(S)*	f(S)*	f(S)*	0.21	0.21
Specific heat	J·K <sup>-1</sup> ·kg <sup>-1</sup>	845	845	845	975	975

\* The thermal conductivity of compacted bentonite is a function of the degree of saturation.

**(a) Limestone Host Rock**

	<b>Units</b>	<b>Layer 1 Buffer 1</b>	<b>Layer 2 Buffer 2</b>	<b>Layer 3 Buffer 3</b>	<b>Layer 4 EDZ</b>	<b>Layer 5 Shale</b>
Length of layer	dm	4	10	10	20	300
Effective diffusion porosity	-	0.24	0.24	0.24	0.02	0.01
Storage porosity	-	0.24	0.24	0.24	0.02	0.01
Non-accessible porosity	-	0	0	0	0	0
Tortuosity factor	-	0.05	0.05	0.05	0.05	0.05
(Particle) density	kg·dm <sup>-3</sup>	2.7	2.7	2.7	2.6	2.6
Sorption capacity for Fe(II)	mol·kg <sup>-1</sup>	0.4	0.4	0.4	0.2	0.2
Initial HCO <sub>3</sub> <sup>-</sup> concentration	mol·dm <sup>-3</sup>	0.001	0.001	0.001	0.001	0.001
Initial Cl <sup>-</sup> concentration	mol·dm <sup>-3</sup>	0.015	0.015	0.015	4.75	4.75
Initial CaCO <sub>3</sub> concentration	mol·dm <sup>-3</sup>	0.28	0.28	0.28	13	13
Thermal conductivity	W·K <sup>-1</sup> ·dm <sup>-1</sup>	f(S)*	f(S)*	f(S)*	0.23	0.23
Specific heat	J·K <sup>-1</sup> ·kg <sup>-1</sup>	845	845	845	830	830

\* The thermal conductivity of compacted bentonite is a function of the degree of saturation.

## **3.2 SENSITIVITY ANALYSES**

### **3.2.1 Saturation Time**

Two simulations were performed to investigate the effect of faster or slower saturation of the repository. Instead of complete saturation of the repository in 10,000 a as in the Base Case simulations, saturation was assumed to occur in either 1,000 a or 100,000 a. The corresponding saturation profiles were developed by simply dividing or multiplying the times shown in Figure 7 by a factor of 10.

All other parameter values were the same as those for the Base Case simulation with shale host rock.

### **3.2.2 Minimum Porosity**

The minimum porosity ( $\epsilon_{\text{MIN}}$ ) defines both the minimum interfacial porosity of precipitated corrosion products (and, hence, the rates of interfacial electrochemical reactions via Equations 14, 16, and 18) and the minimum porosity in the buffer, EDZ and rock layers (which, along with the time-dependent saturation, impacts the accumulation and release of gaseous  $\text{H}_2$ ).

The minimum porosity for this sensitivity analysis was increased to 0.05 (from 0.01 for the Base Case simulations).

All other parameter values were the same as those for the Base Case simulation with shale host rock.

### **3.2.3 Threshold Relative Humidity**

The threshold relative humidity values determine the onset of corrosion (when the interfacial buffer relative humidity  $h_k$  is greater than the lower threshold  $h_{k,\text{min}}$ ) and the value of the interfacial rate constant (pro-rated between  $h_{k,\text{min}}$  and  $h_{k,\text{max}}$  and equal to that in bulk solution for  $h_k \geq h_{k,\text{max}}$ ) (Section 2.2.2.5).

For the Base Case simulations, values of 0.6 and 1.0 are used for  $h_{k,\text{min}}$  and  $h_{k,\text{max}}$ , respectively.

In one sensitivity analysis, the value of  $h_{k,\text{max}}$  was set at 0.7, resulting in higher values of the electrochemical rate constant between the time when the surface first becomes wetted and complete saturation of the bentonite closest to the container.

In a second sensitivity analysis, the value of  $h_{k,\text{min}}$  was reduced to 0.2, resulting in the earlier onset of corrosion compared with the Base Case.

All other parameter values were the same as those for the Base Case simulation with limestone host rock.

## 4. RESULTS OF SIMULATIONS

In order to speed up execution of the code, the simulations were split into two phases. Phase 1 corresponds to the period during which  $h_k \leq h_{k,\min}$  and Phase 2 corresponds to the period for which  $h_k > h_{k,\min}$ . Interfacial electrochemical reactions do not occur during Phase 1, so that the only processes in the model are:

1. saturation of the buffer and EDZ,
2. dissolution and precipitation of  $\text{CaCO}_3$ ,
3. the ingress of  $\text{HCO}_3^-$  and  $\text{Cl}^-$  ions as the buffer and EDZ saturate with groundwater,
4. transport of  $\text{HCO}_3^-$  and  $\text{Cl}^-$  ions, and
5. the evolution of the container surface temperature and temperature distribution in the repository.

### 4.1 BASE CASE SIMULATIONS

#### 4.1.1 Shale Host Rock

##### 4.1.1.1 Phase 1

For the Base Case simulation, no corrosion is predicted to occur for the first 4998 a. At that time, the degree of saturation of the first layer of buffer equals 0.425 which corresponds to a relative humidity of 0.6 or 60%. The container surface temperature at that time is  $77^\circ\text{C}$ , having decreased from the peak temperature of approximately  $118^\circ\text{C}$  attained after 10 a.

Figure 8 shows the predicted time dependence of the pore-water  $\text{Cl}^-$  content integrated over each of the five layers in the model. This increase in  $\text{Cl}^-$  content is largely the result of the ingress of groundwater saturating the bentonite rather than the diffusion of  $\text{Cl}^-$  ions from the host rock, as is apparent from the similarity in shape with the saturation profiles during this same period (Figure 9). As a consequence of the ingress of  $\text{Cl}^-$  from the groundwater, the interfacial  $\text{Cl}^-$  concentration increases from an initial value of  $0.015 \text{ mol}\cdot\text{dm}^{-3}$  (determined by the salt impurity content of bentonite and the initial buffer moisture content, Appendix A.2) to a value of  $3.49 \text{ mol}\cdot\text{dm}^{-3}$  at the onset of corrosion. Thus, anaerobic corrosion occurs in a saline environment.

There is no corresponding increase in  $\text{HCO}_3^-$  content of the pore water during Phase 1 because the bicarbonate concentration is determined by the solubility of calcite. Thus, the small changes predicted in the  $\text{HCO}_3^-$  pore water concentration (not shown) are a result only of the temperature-dependence of the solubility product of  $\text{CaCO}_3$ .

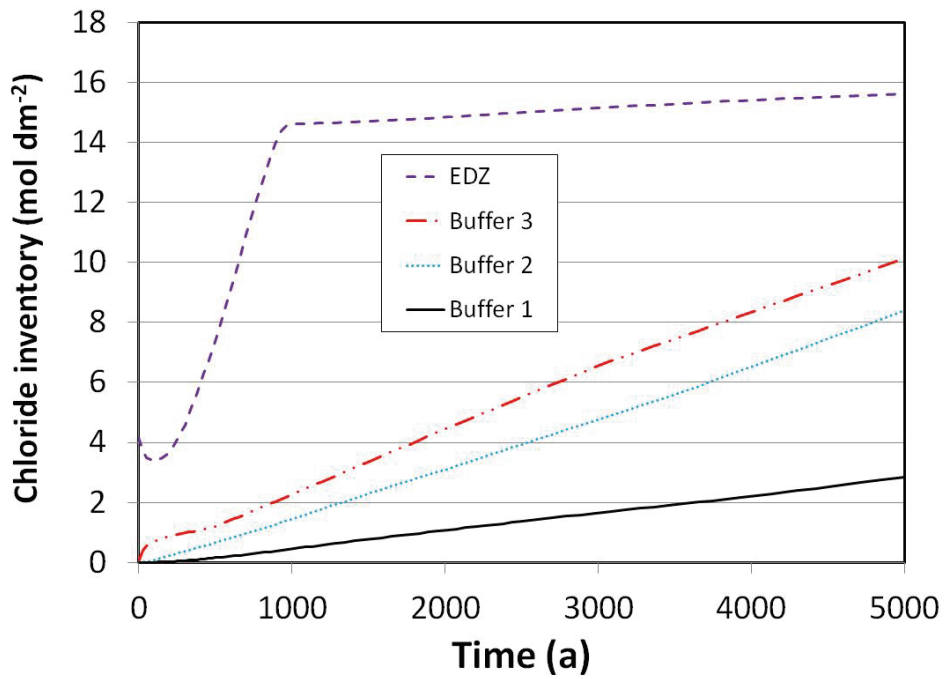


Figure 8: Time Dependence of the Pore-water Chloride Ion Inventory During Phase 1 of the Base Case Simulation for Shale Host Rock

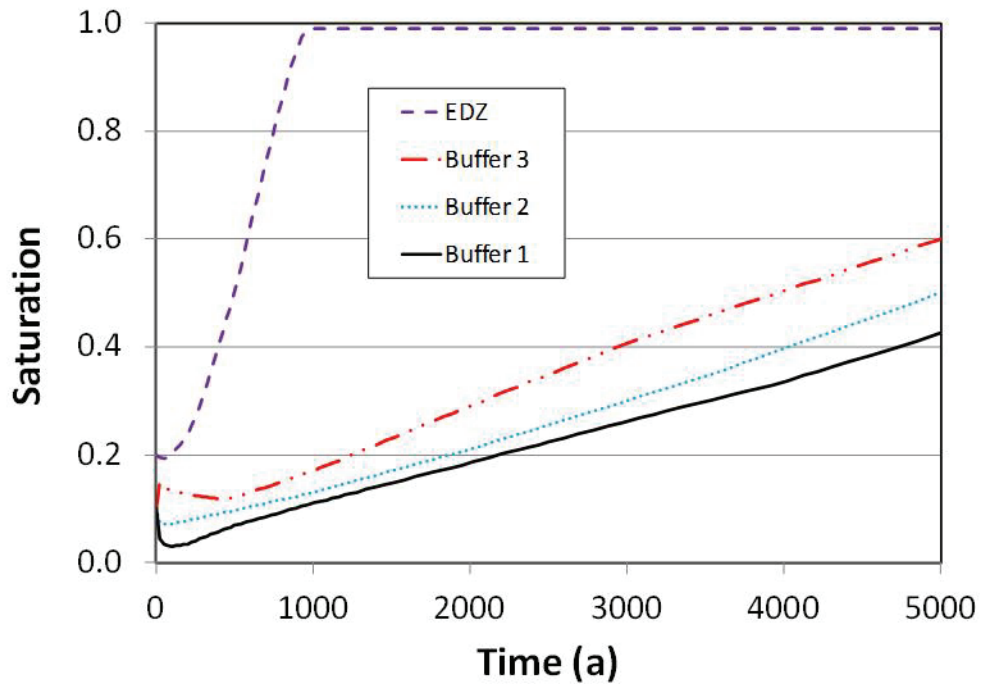
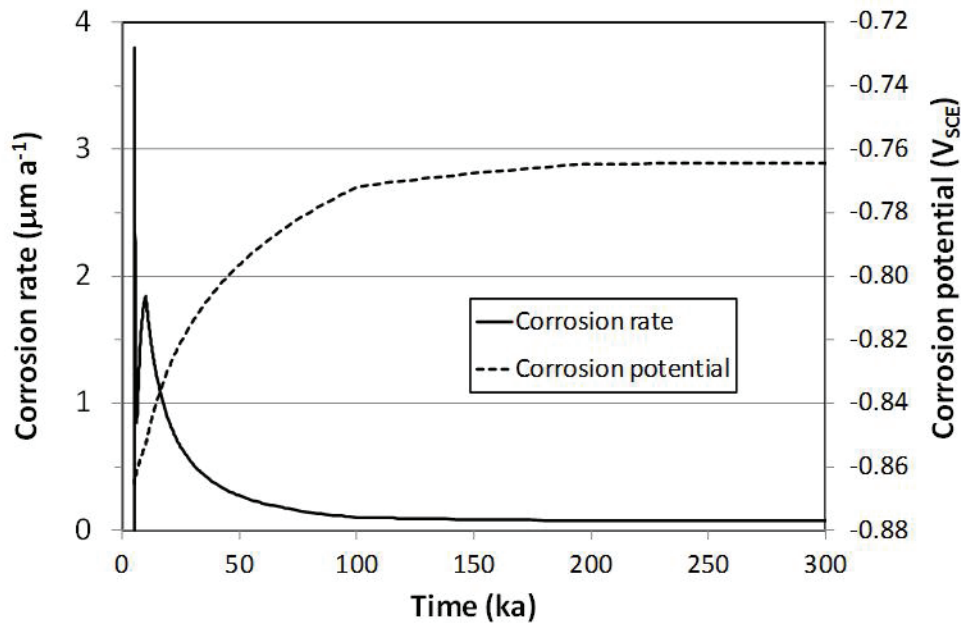


Figure 9: Saturation Profiles for the Buffer and EDZ During Phase 1 of the Base Case Simulation for Shale Host Rock

#### 4.1.1.2 Phase 2

Anaerobic corrosion of the container commences at approximately 5000 a after emplacement resulting in consumption of the assumed 2-cm corrosion allowance in 19,500 a. Figure 10 shows the predicted time dependence of the corrosion rate and corrosion potential over an extended period of time. The peak corrosion rate is of the order of  $4 \mu\text{m}\cdot\text{a}^{-1}$ , with a long-term steady-state rate (after 100,000 a) of  $\sim 0.1 \mu\text{m}\cdot\text{a}^{-1}$ . These rates are in good agreement with those measured experimentally in compacted bentonite and in bulk solution (King 2008). The corrosion potential is of the order of  $-0.80 V_{\text{SCE}}$ , typical of the value observed under anaerobic conditions (Qin et al. 2005). Dissolution of the container is supported by the cathodic reduction of  $\text{H}_2\text{O}$ , with the reduction of  $\text{HCO}_3^-$  accounting for  $<0.1\%$  of the total current density (Figure 11).

In the model, the corrosion rate is influenced by a number of factors, which leads to distinct stages in the evolution of the corrosion behaviour (Figure 12). The controlling factors are (i) the interfacial porosity of the corrosion product film, (ii) the availability of water, and (iii) temperature. Neither the anodic dissolution reaction nor the cathodic reduction of  $\text{H}_2\text{O}$  are influenced by mass transport of reactants to, or of corrosion products away from, the corroding surface.<sup>1</sup> Four stages in the time dependence of the corrosion rate can be identified. Stage I corresponds to Phase 1 prior to the wetting of the container surface. In Stage II, the initially high rate of dissolution of the (assumed) bare steel surface decreases with time as a protective surface film (of  $\text{Fe}_3\text{O}_4$ ) develops. This can be seen by comparing the time dependences of the corrosion



**Figure 10: Predicted Time Dependence of the Corrosion Rate and Corrosion Potential of a Carbon Steel Container for the Base Case Simulation with Shale Host Rock**

<sup>1</sup> The anodic dissolution reaction is considered to be irreversible, so that the rate of the forward reaction is not affected by the interfacial concentration of corrosion products, i.e.,  $\text{H}_2$  and  $\text{Fe(II)}$ . The availability of  $\text{H}_2\text{O}$  limits the rates of all interfacial reactions equally, but is assumed to not specifically limit the rate of  $\text{H}_2\text{O}$  reduction.

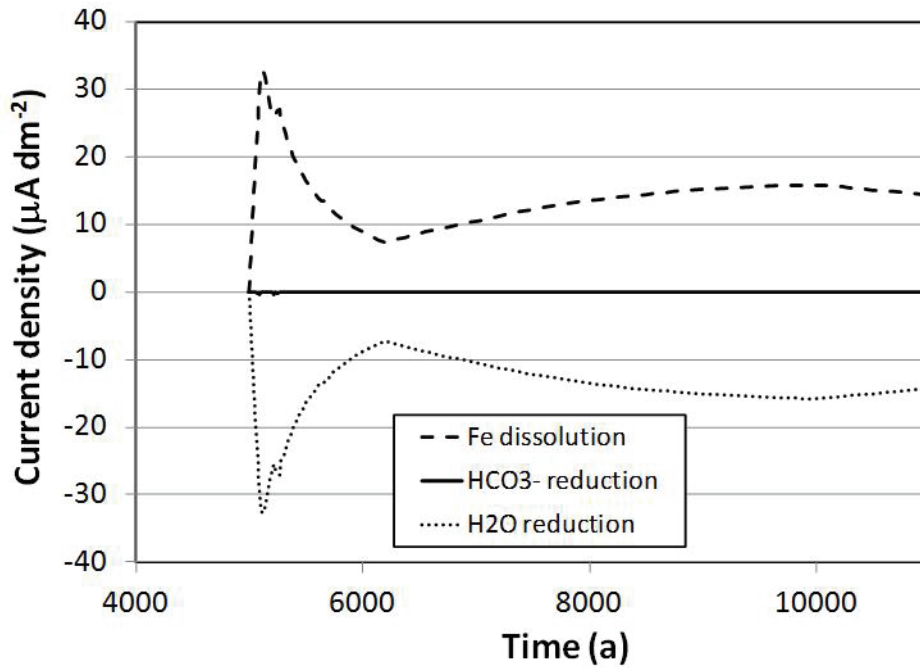


Figure 11: Predicted Time Dependence of the Anodic and Cathodic Current Densities for the Base Case Simulation with Shale Host Rock

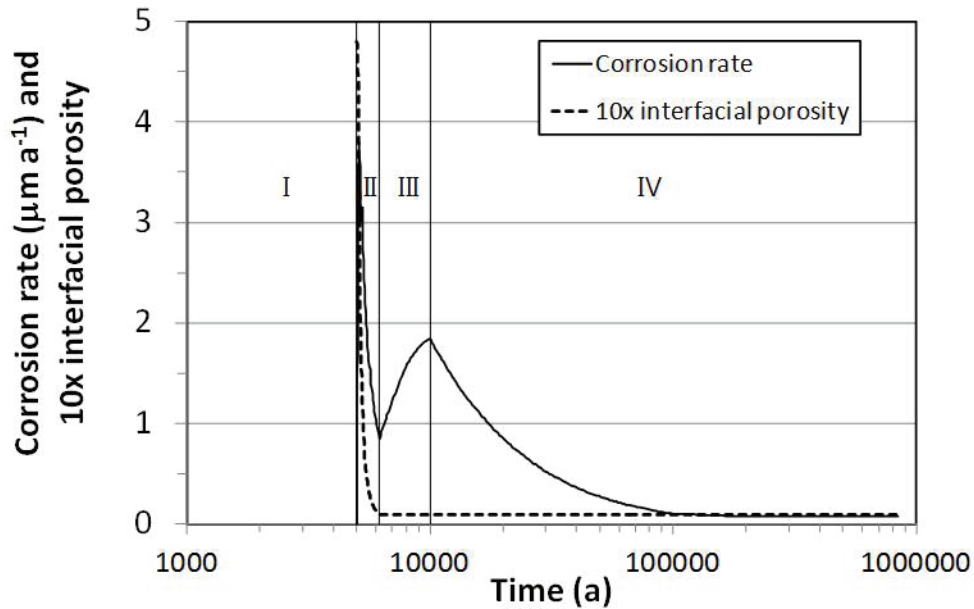
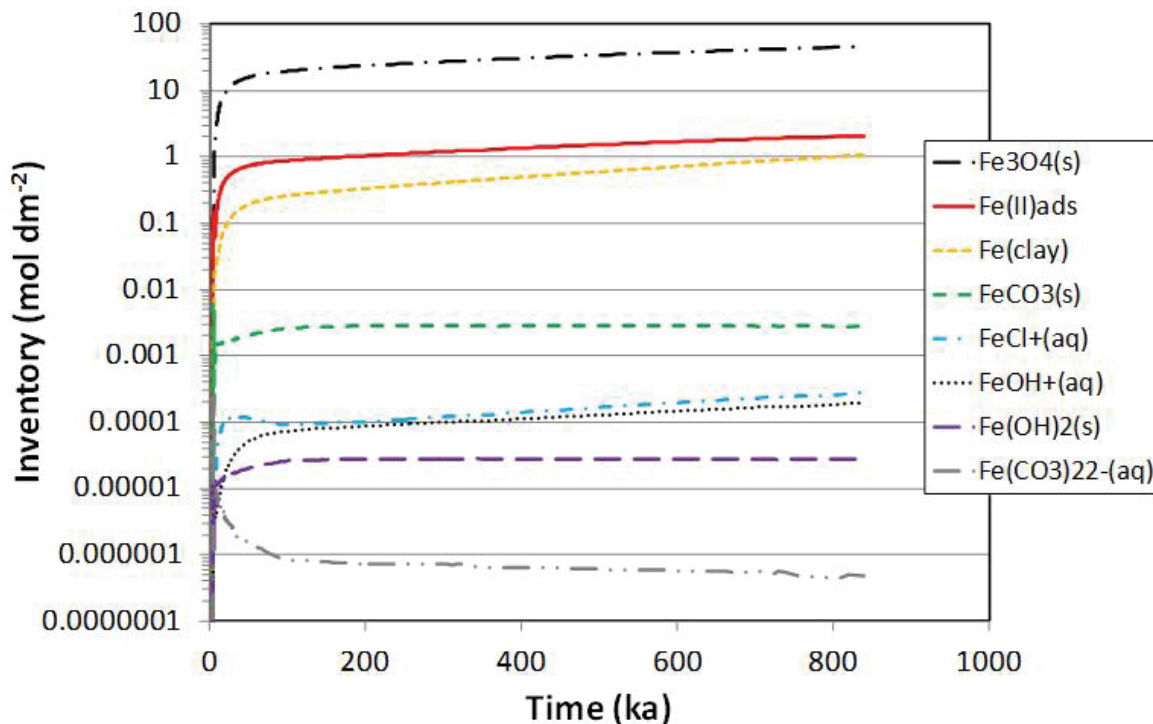


Figure 12: Time Dependence of the Corrosion Rate and Interfacial Porosity Illustrating Various Stages in the Evolution of the Corrosion Behaviour (Base Case Simulation with Shale Host Rock)

rate and of the interfacial porosity in Figure 12. The inhibiting effect of the build up of a corrosion product layer during Stage II is more significant than the increase in rate due to the progressive saturation of the buffer material. However, once the minimum interfacial porosity is attained, the corrosion rate increases as a result of the continued increase in the degree of saturation and, hence, of the rates of the interfacial electrochemical reactions (Stage III). Finally, once the repository is fully saturated after 10,000 a, the corrosion rate decreases with time during Stage IV as the container continues to cool.

In contrast to the complex time dependence of the corrosion rate,  $E_{CORR}$  exhibits a gradual shift to more-positive values before reaching an apparent steady state after several hundred thousand years (Figure 10). There is no effect of the interfacial porosity or the buffer saturation on  $E_{CORR}$  because both parameters affect the rates of the anodic and cathodic reactions equally. Thus, the gradual positive shift in  $E_{CORR}$  is due solely to the decrease in container temperature with time.

Eight different Fe-based corrosion products are treated in the SCM V1.0 and the predicted amounts of each are quite different. Figure 13 shows the time dependence of the inventory (the spatially integrated concentration) of each of the eight species as a function of time. Most of the corroded Fe is present in the form of various solids, either precipitated  $Fe_3O_4$ ,  $FeCO_3$ , or  $Fe(OH)_2$ ; adsorbed Fe(II); or altered bentonite clay. Figure 14 shows the accumulation of the three main solid species in more detail, illustrating the linear increase in the inventories as the corrosion rate attains a steady-state value. The inventory of dissolved species is small because of the limited solubility of Fe(II) in neutral to slightly alkaline solution, with approximately equal proportions of dissolved  $FeCl^+$  and  $FeOH^+$  (Figure 13)



**Figure 13: Predicted Time Dependence of the Inventories of Iron-based Corrosion Products for the Base Case Simulation with Shale Host Rock**

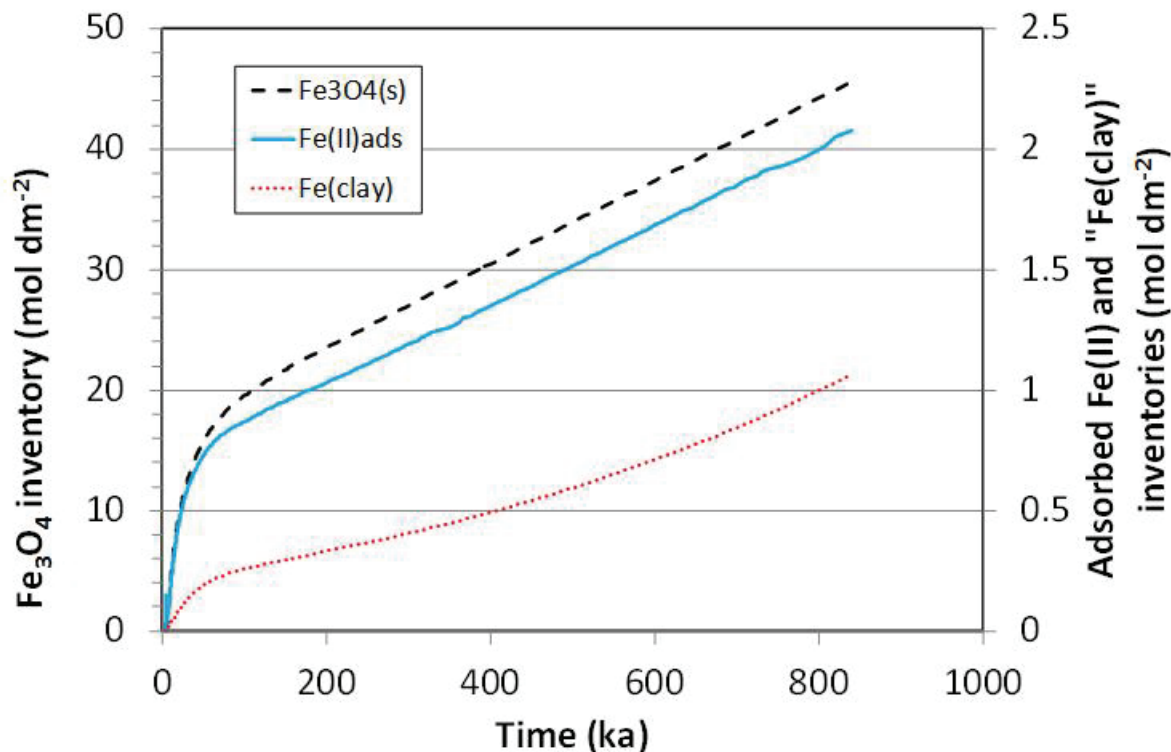


**Figure 14: Time Dependence of the Accumulation of Magnetite, Adsorbed Iron, and Altered Clay for the Base Case Simulation with Shale Host Rock. Note the smaller scale for the latter two species**

By far the most prevalent Fe-based corrosion product is  $\text{Fe}_3\text{O}_4$ . Magnetite is predicted to precipitate in the pores of the bentonite and to create a front of bentonite mixed with  $\text{Fe}_3\text{O}_4$  that moves outwards from the container surface (Figure 15). By the time the container has completely corroded (after 840,000 a), this moving front has penetrated approximately 0.4 m into the buffer material. The maximum  $\text{Fe}_3\text{O}_4$  “concentration” of approximately  $10.5 \text{ mol}\cdot\text{dm}^{-3}$  is the amount of magnetite that accumulates in the bentonite pore space for the assumed minimum porosity of 0.01 based on a  $\text{Fe}_3\text{O}_4$  density of  $5.18 \text{ g}\cdot\text{cm}^{-3}$  (Appendix A.2). The impact of accumulating  $\text{Fe}_3\text{O}_4$  on the porosity of the various mass-transport layers considered in the model is illustrated in Figure 16.

Although smaller amounts of dissolved Fe(II) interact with the clay, the extent of clay alteration near the container surface is not insignificant. Figures 17 and 18 show the concentration profiles for adsorbed Fe(II) and “Fe-clay”, respectively, for various simulated times. The maximum adsorption capacity of the bentonite for Fe(II) (based on an assumed cation exchange capacity CEC of  $80 \text{ meq}\cdot 100 \text{ g}^{-1}$ ) is  $0.4 \text{ mol}\cdot\text{kg}^{-1}$ . It is apparent from Figure 17 that the bentonite adsorption sites are ~95% occupied by Fe(II) near the interface and that the adsorption “front” moves further from the container surface with increasing time, in a similar manner and to a similar extent as the  $\text{Fe}_3\text{O}_4$  “front” (Figure 15). Thus, once the container has completely corroded and radionuclides are released, there will be competitive adsorption between Fe(II) and cationic radionuclides for sorption sites on the bentonite.

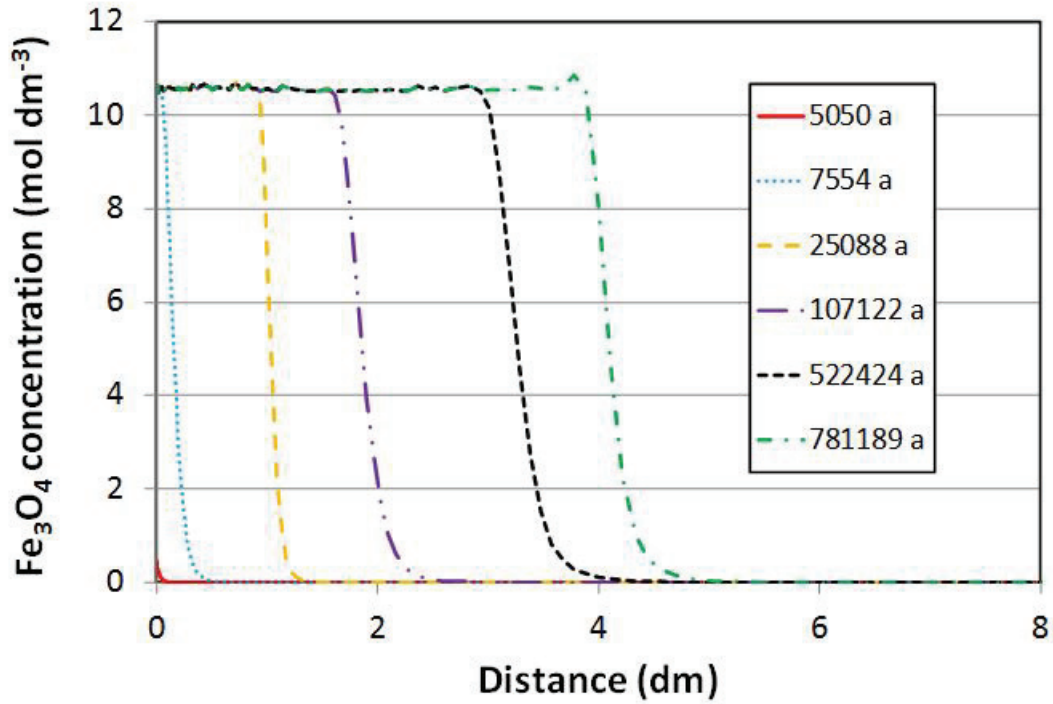


Figure 15: Progression of the Magnetite “Front” for the Base Case Simulation with Shale Host Rock

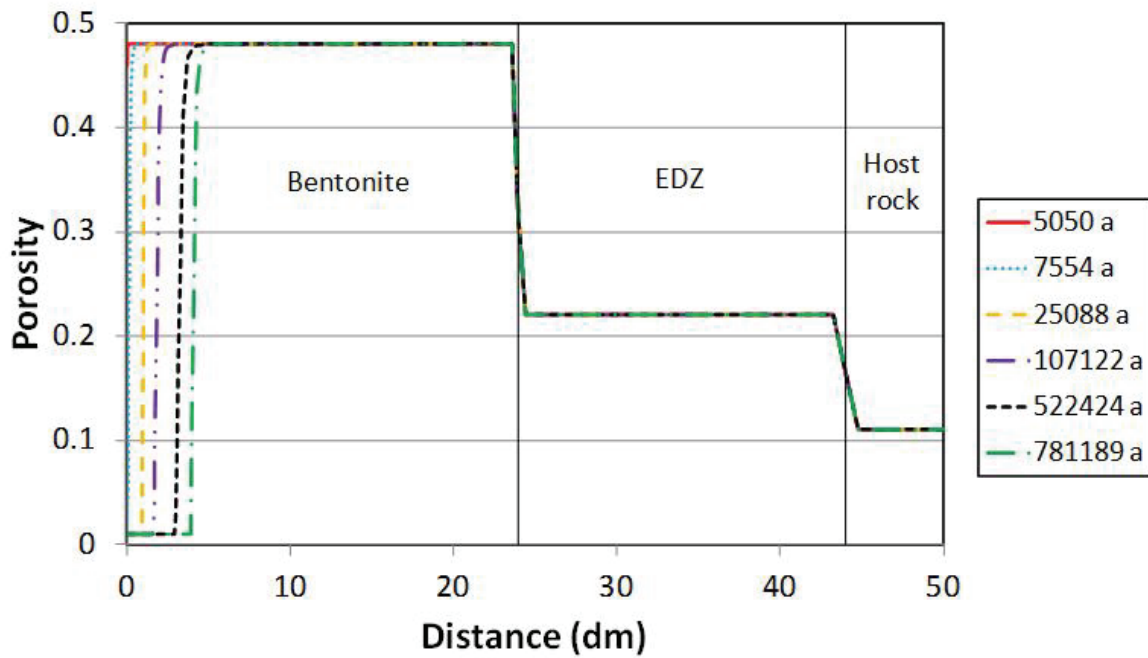


Figure 16: Predicted Time Dependence of the Porosity of the Bentonite, EDZ, and Host Rock Layers for the Base Case Simulation with Shale Host Rock

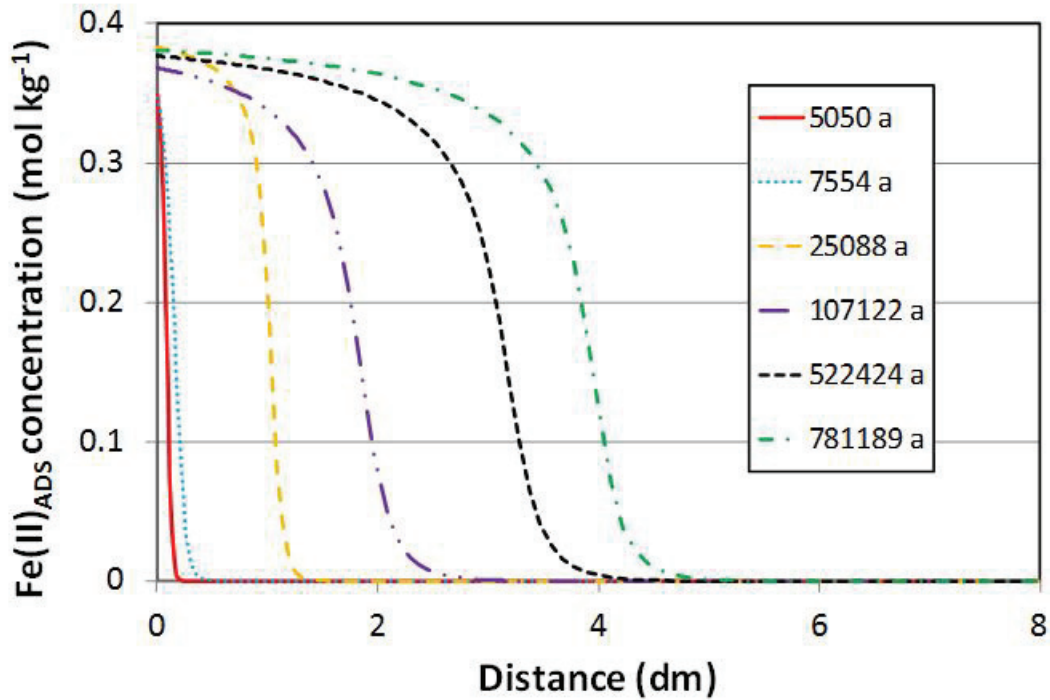


Figure 17: Concentration Profiles for Adsorbed Fe(II) as a Function of Time for the Base Case Simulation with Shale Host Rock

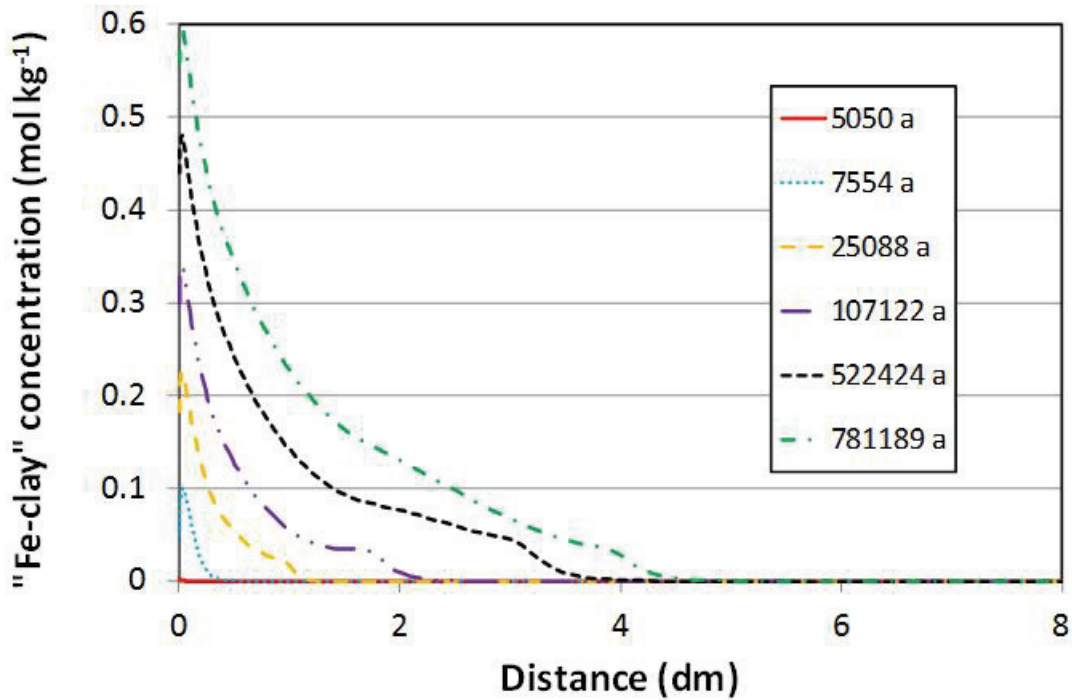


Figure 18: Predicted Distribution of Altered Bentonite Clay as a Function of Time for the Base Case Simulation with Shale Host Rock

In addition to saturating nearly all of the adsorption sites on the bentonite, dissolved Fe(II) also promotes alteration of the clay (Wersin and Snellman 2008). In SCM V1.0, the rate of clay alteration is assumed to be limited by the temperature-dependent dissolution of montmorillonite (Wersin et al. 2007). The maximum predicted concentration of “Fe-clay” (i.e., the concentration of Fe(II) in the altered clay) of  $\sim 0.6 \text{ mol}\cdot\text{kg}^{-1}$  represents approximately 13% alteration of the bentonite.<sup>2</sup> Thus, especially after long times, the swelling capacity of the bentonite within a few cm of the container may be compromised.

The other corrosion product of interest is hydrogen. Hydrogen will exist as dissolved  $\text{H}_2$  in the aqueous phase and as gaseous  $\text{H}_2$  in the unsaturated pores of the buffer, EDZ, and host rock. The capacity of the buffer and EDZ for  $\text{H}_2$ , especially in the gaseous form, prior to repository saturation by incoming groundwater exceeds that following saturation. Because the rate of  $\text{H}_2$  generation by anaerobic corrosion is expected to exceed that rate at which dissolved  $\text{H}_2$  can diffuse through the host rock (Nagra 2004), it is likely that a gaseous  $\text{H}_2$  phase will form and that hydrogen transport will occur by two-phase flow, resulting in periodic advection of pore water. Detailed modelling of such complex hydrogeological-mechanical (H-M) processes is outside the scope of the current model so these effects are treated in a simplified manner. To simulate the likely presence of both aqueous and gaseous phases in the repository as a result of gas formation from anaerobic corrosion, a maximum degree of saturation of 0.99 is defined for the buffer, EDZ, and host rock. The assumed 1% of unsaturated pore space allows for the continued accumulation of gaseous  $\text{H}_2$  that would be expected in the actual repository.

Figure 19 shows the predicted  $\text{H}_2$  partial pressure throughout the repository and host rock for selected times during the simulation. The  $\text{H}_2$  partial pressure is modest after 5050 a, which is approximately 50 a after the onset of anaerobic corrosion and prior to complete saturation of the repository (hence, there is still significant unsaturated porosity to “store” gaseous  $\text{H}_2$ ). The  $\text{H}_2$  partial pressure continues to increase up to 7376 a (profile not shown in Figure 19) at which time the pressure in the buffer exceeds the assumed 8 MPa breakthrough pressure and sufficient  $\text{H}_2$  is released to lower the pressure to 5 MPa at which point the buffer is assumed to re-seal. Gaseous  $\text{H}_2$  continues to accumulate and the pressure then varies between 5 MPa and 8 MPa as gas accumulates and is periodically released. The pressure distribution indicated by the profiles shown in Figure 19 depends on where that particular time occurs between these gas release events.

The build-up and periodic release of gas is more clearly seen in Figure 20 which shows the time dependence of the dissolved and gaseous  $\text{H}_2$  inventories in the repository (buffer, EDZ, and host rock). There is a significant inventory of gaseous  $\text{H}_2$  prior to saturation up to 10,000 a. Following saturation, the inventories of both dissolved and gaseous  $\text{H}_2$  oscillate as pressure builds up and is then released (the concentration of dissolved  $\text{H}_2$  and pressure of gaseous  $\text{H}_2$  are linked in the model via Henry’s Law). In total, there are predicted to be 164 such  $\text{H}_2$  release events prior to complete corrosion of the container (Figure 21).

---

<sup>2</sup> Based on a molecular mass of montmorillonite ( $\text{Na}_{0.25}(\text{Al}_{1.75}\text{Mg}_{0.25})\text{Si}_4\text{O}_{10}(\text{OH})_2$ ) of  $365.22 \text{ g}\cdot\text{mol}^{-1}$ , the assumption that the bentonite is 100% montmorillonite, and the fact that 1.7 mol Fe(II) reacts with 1 mol montmorillonite.

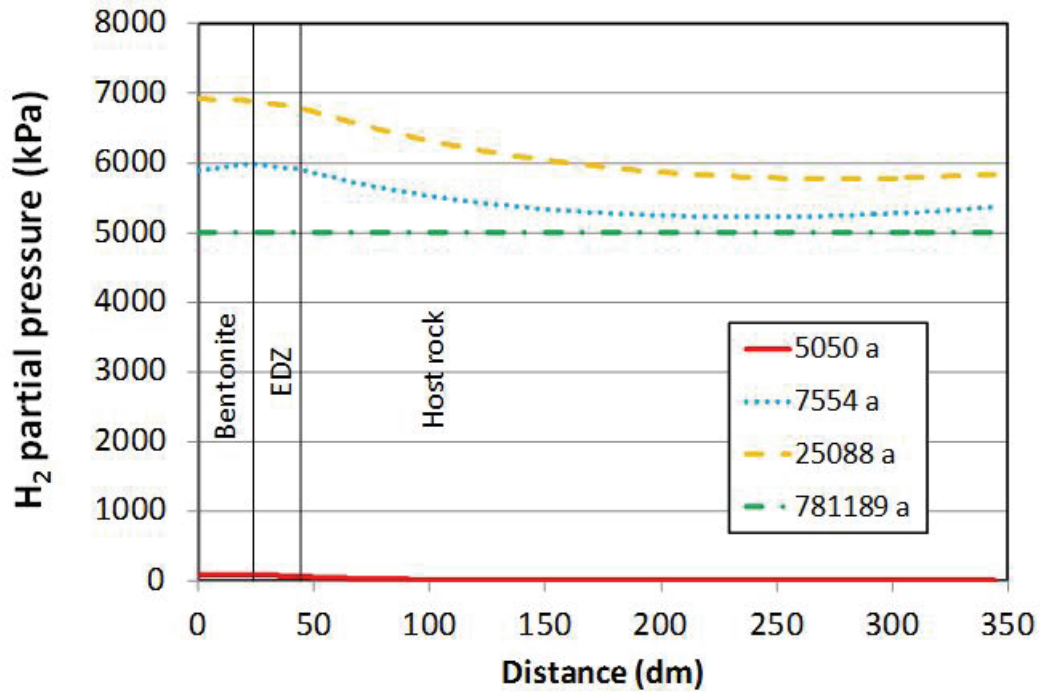


Figure 19: Predicted Hydrogen Partial Pressure in the Repository for Selected Times for the Base Case Simulation with Shale Host Rock

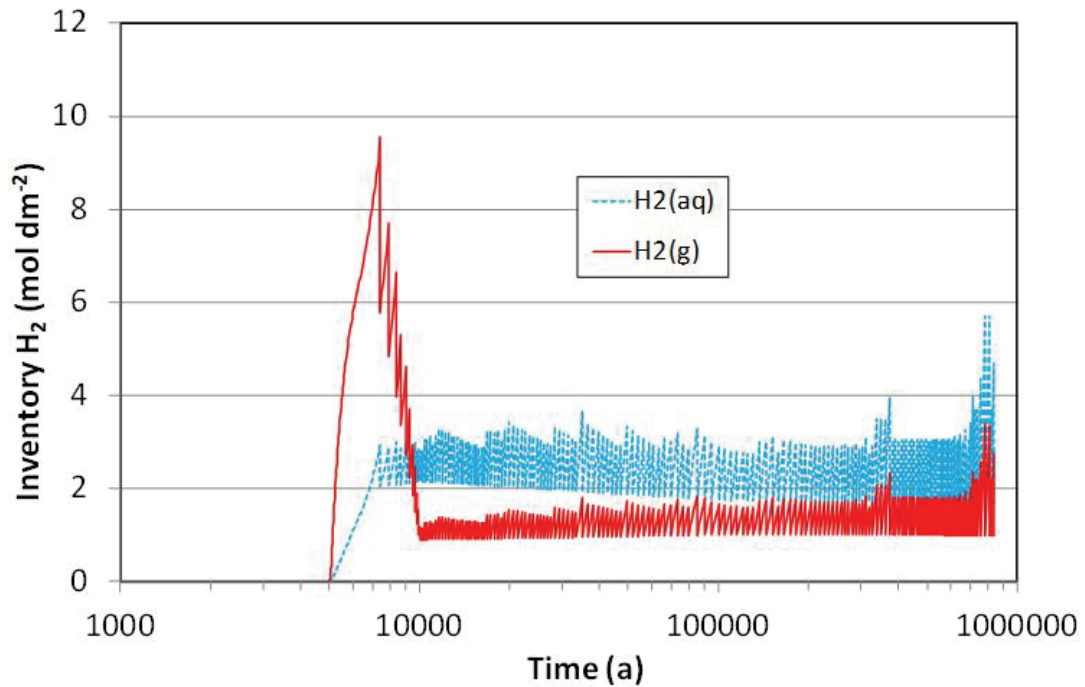
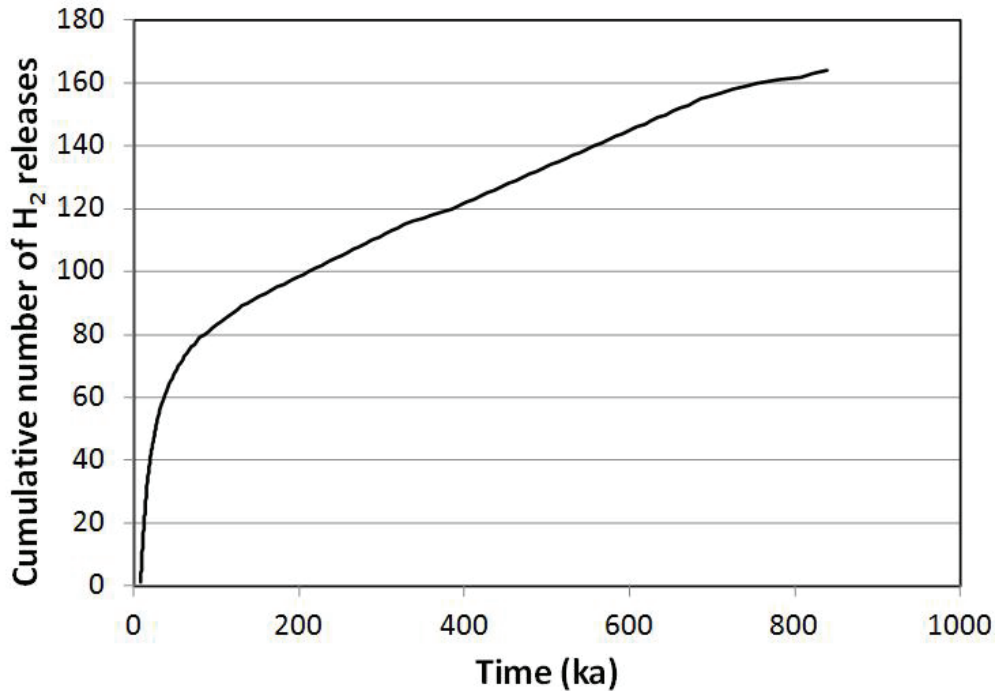


Figure 20: Inventory of Gaseous and Dissolved Hydrogen in the Repository as a Function of Time for the Base Case Simulation with Shale Host Rock



**Figure 21: Cumulative Number of Gas Release Events for the Base Case Simulation with Shale Host Rock**

#### 4.1.2 Limestone Host Rock

There are relatively few differences between the properties of the limestone and shale host rock in terms of the parameters in the model (Table 3). In addition to differences in the specific heat and thermal conductivity of the two materials, the only other differences are the higher calcite content of limestone and the lower porosity of the EDZ and host rock.

The evolution of the environment during Phase 1 in the case of limestone host rock is similar to that for shale. One minor difference, however, that does impact the corrosion behaviour of the container results from the difference in thermal properties of shale and limestone. Because of the lower specific heat and the higher thermal conductivity of limestone (Table 3), heat is conducted away faster and the repository and host rock are cooler than in the case of shale (Figure 22). Furthermore, because of the retrograde solubility of calcite (i.e., the  $\text{CaCO}_3$  solubility increases with decreasing temperature, see Appendix A.2), the pore-water concentration of  $\text{HCO}_3^-$  is higher in the host rock and the buffer material.<sup>3</sup> The consequences of the increased flux of  $\text{HCO}_3^-$  on corrosion of the container are discussed in more detail below.

<sup>3</sup> In fact, the predicted temperature of the container surface is slightly higher for the limestone host rock, leading to a higher pore-water  $[\text{HCO}_3^-]$  in the buffer closest to the container. However, the  $\text{HCO}_3^-$  concentration gradient is highest for the limestone case, which will result in faster supply of bicarbonate to the container surface.

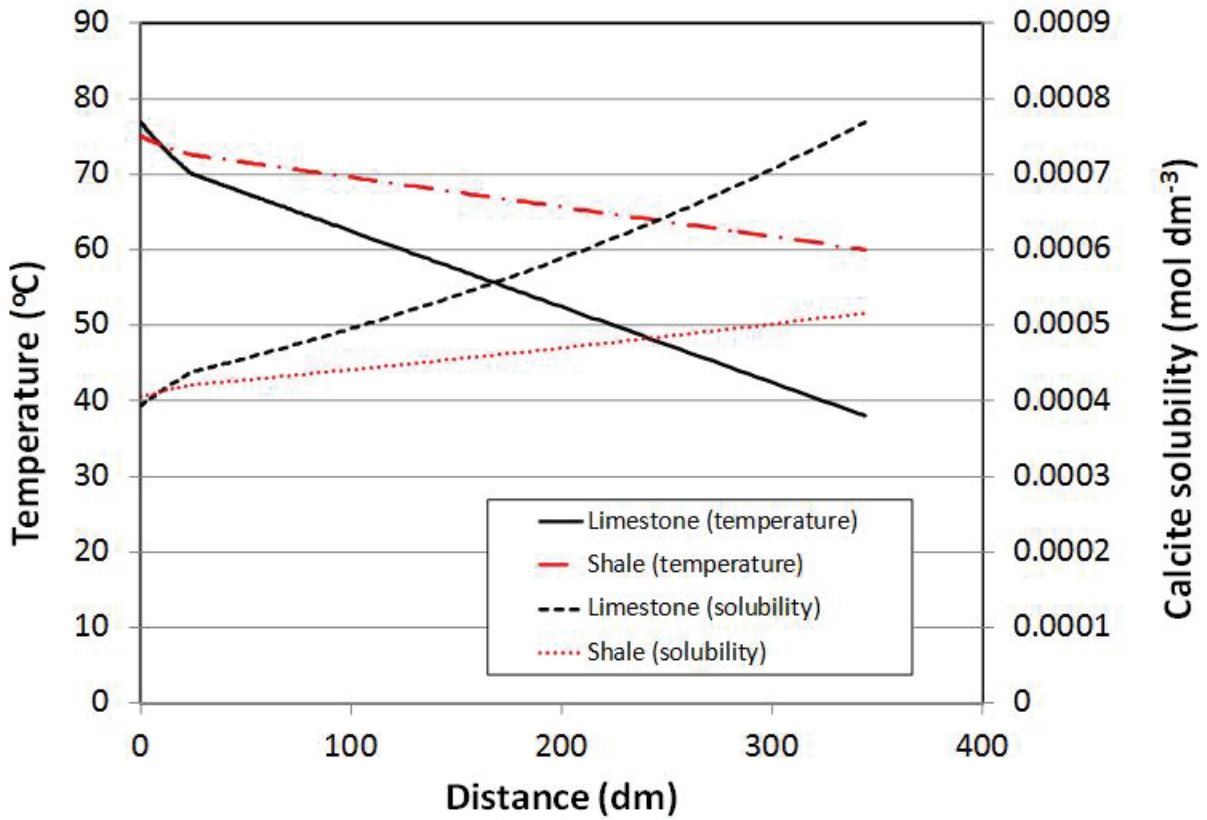


**Figure 22: Comparison of the Distribution of Temperature and Calcite Solubility in the Buffer and Host Rock at the End of Phase 1 (4998 a) for the Base Case Simulations with Shale and Limestone Host Rock**

Figures 23-25 show comparisons of the time dependence of the corrosion potential, corrosion rate, and the depth of corrosion, respectively, for the Base Case simulations for limestone and shale host rocks. The time dependences of the corrosion potential for the limestone and shale host rocks are identical (Figure 23) since the variation in  $E_{CORR}$  is largely determined by the variation in container surface temperature which is the same for the two host rocks. However, there is a slight difference in the respective corrosion rates (Figure 24), with a slightly higher peak value predicted for limestone followed by a more rapid decrease due to film formation (Figure 24, Table 4). Overall, however, there is little difference in the predicted container lifetime (Table 4) or the time dependence of the depth of corrosion (at least on the scale used in Figure 25).

The higher peak corrosion rate in the limestone case is the result of the differences in calcite solubility illustrated in Figure 22. Figure 26 shows the time dependences of the corrosion rate (Figure 26(a)) and of the interfacial porosity (Figure 26(b)) for a period of 1000 a immediately following the onset of corrosion after 5000 a. The higher corrosion rate for the limestone host rock between times of approximately 5100 a and 5400 a is a result of (i) a higher rate of  $HCO_3^-$  reduction (not shown) and, more importantly, (ii) the higher interfacial porosity (Figure 26(b)).

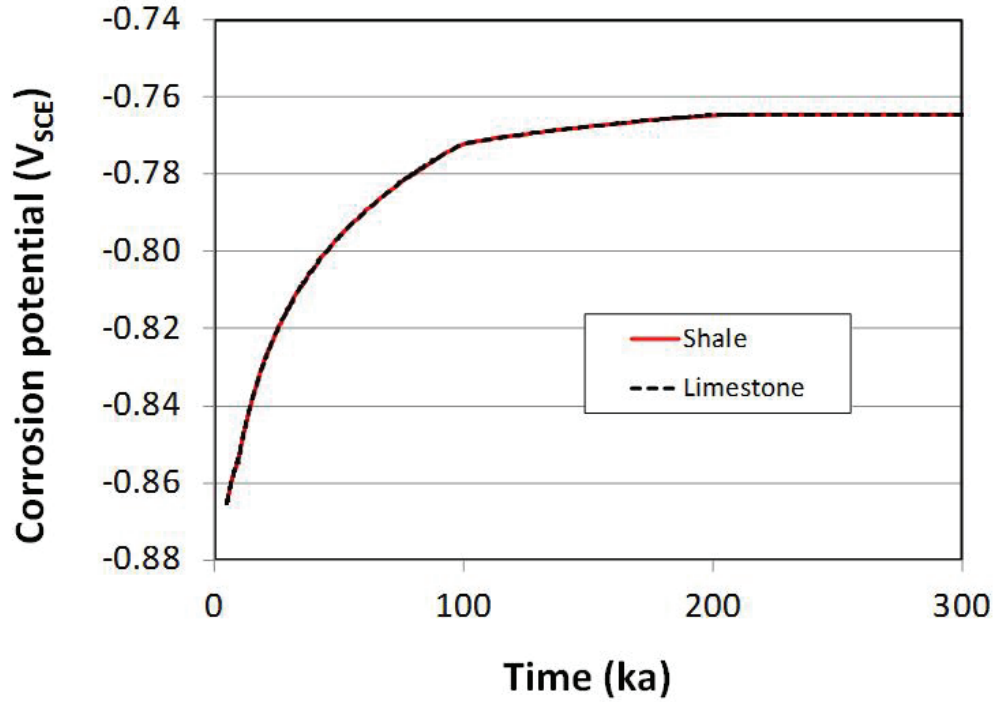


Figure 23: Comparison of the Predicted Time Dependence of the Corrosion Potential for the Base Case Simulations with Limestone and Shale Host Rocks

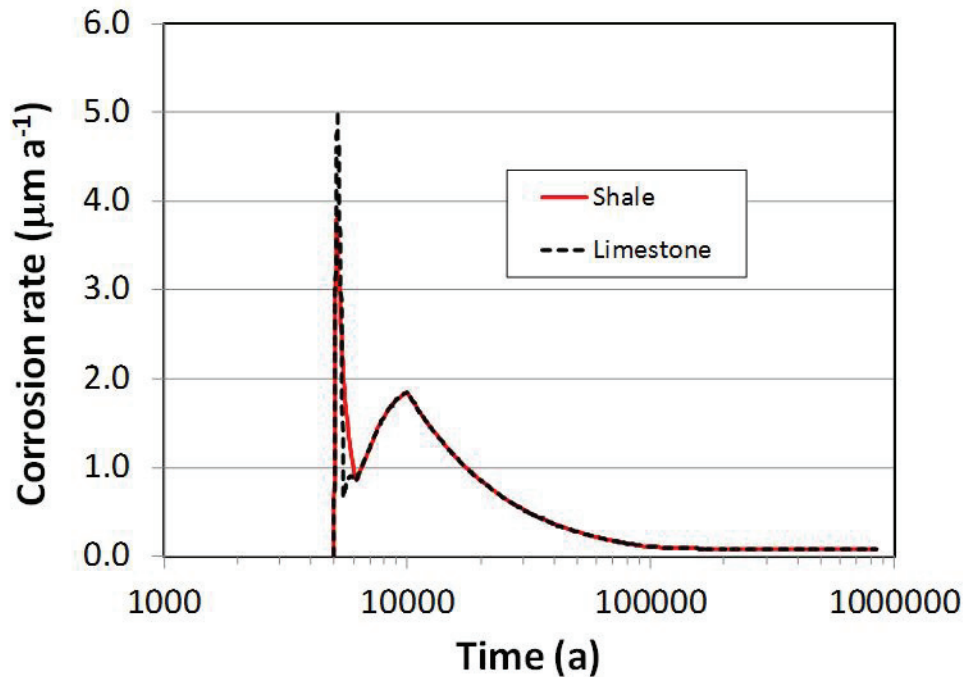
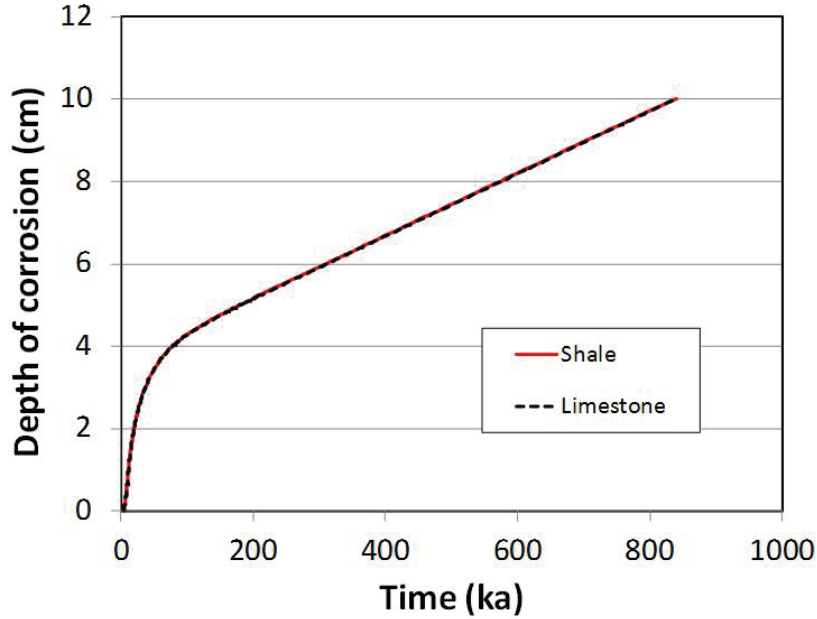


Figure 24: Comparison of the Predicted Time Dependence of the Corrosion Rate for the Base Case Simulations with Limestone and Shale Host Rocks

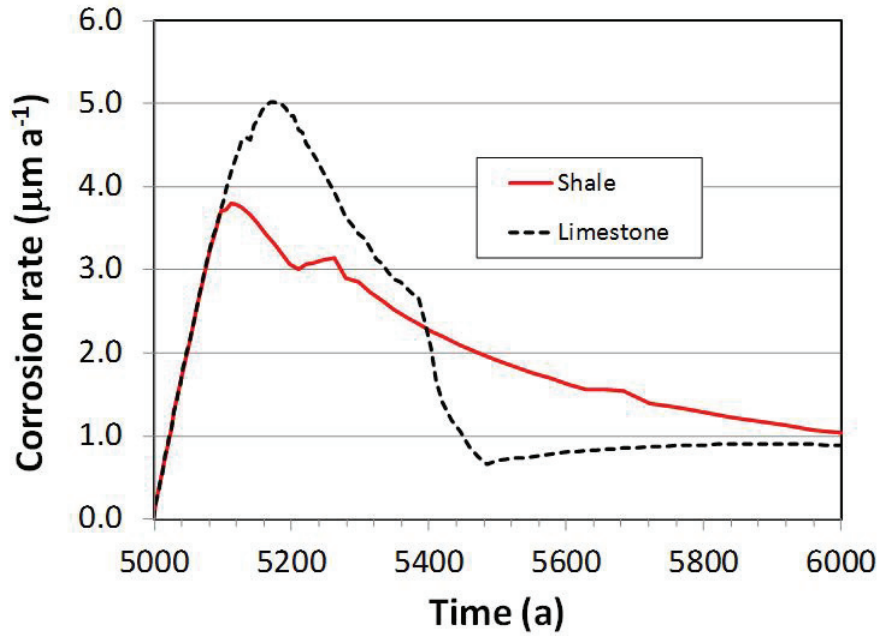


**Figure 25: Comparison of the Predicted Time Dependence of the Depth of Corrosion for the Base Case Simulations with Limestone and Shale Host Rocks**

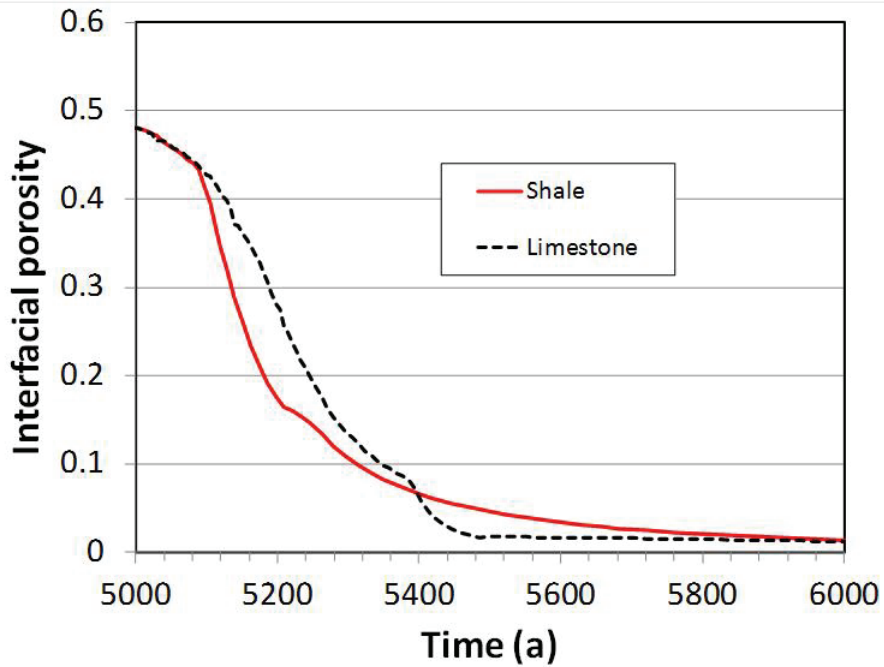
**Table 4: Summary of the Predicted Container Corrosion Performance for the Base Case Simulations and Sensitivity Analyses**

Simulation	Onset of corrosion (a)	Container lifetime (a)*	Mean corrosion rate ( $\mu\text{m}\cdot\text{a}^{-1}$ )		Maximum corrosion rate ( $\mu\text{m}\cdot\text{a}^{-1}$ )
			Since deposition	Since onset of corrosion	
Base case – shale	5,000	19,500	1.0	1.4	3.8
Base Case – limestone	5,000	19,800	1.0	1.4	5.0
Faster saturation	500	8,200	2.4	2.6	6.9
Slower saturation	50,000	190,000	0.11	0.14	0.83
Higher minimum porosity	5,000	8,700	2.3	5.4	9.2
Lower maximum threshold RH	5,000	14,200	1.4	2.2	7.6
Lower minimum threshold RH	950	13,800	1.4	1.6	2.5

\* Based on 2-cm corrosion allowance.



(a) Corrosion rates



(b) Interfacial porosity

Figure 26: Comparison of the Predicted Corrosion Rate and Interfacial Porosity for the Period Between 5000 a and 6000 a for the Base Case Simulations with Shale and Limestone Host Rocks

The latter is the result of the higher  $[\text{HCO}_3^-]$  which results in less precipitation and a higher concentration of dissolved  $\text{Fe}(\text{CO}_3)_2^{2-}$  species. However, the effect is small and disappears once the  $\text{HCO}_3^-$  is depleted near the container surface.

Of more significance is the predicted difference in the number of gas release events for the Base Case shale and limestone simulations. Figure 27 shows the comparison of the number of gas releases for the two Base Case simulations. The number of gas releases is related to the amount of  $\text{H}_2$  generated (which is the same for the two simulations based on the predicted time-dependent depths of corrosion in Figure 25) and the storage capacity of the buffer and host rock (a function of the porosity and degree of saturation). Since the time dependence of the degree of saturation is the same in both cases, the higher number of gas releases for the limestone simulation is due solely to the lower porosity of limestone compared with shale. Although there is a five-fold difference in porosity between the two host rocks (Table 3), much of the storage capacity is associated with the buffer, so the difference in the number of gas releases is only about a factor of two.

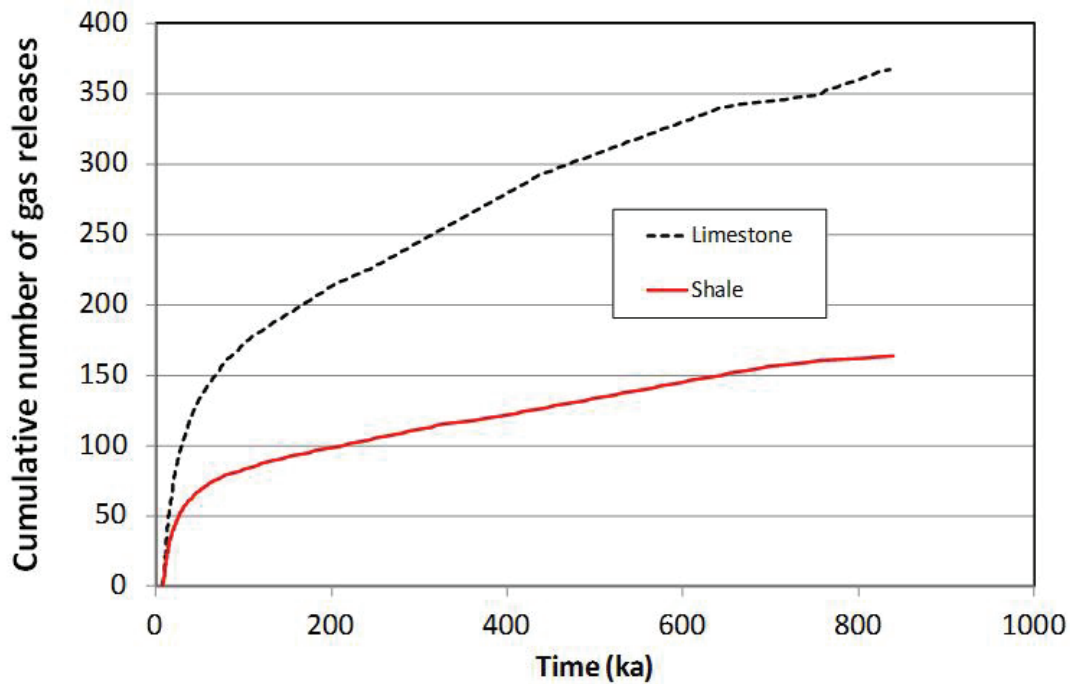


**Figure 27: Comparison of the Number of Gas Releases for the Base Case Simulations with Limestone and Shale Host Rocks**

## 4.2 SENSITIVITY ANALYSES

### 4.2.1 Saturation Time

The exact saturation time of a DGR in sedimentary rock is uncertain. The saturation time will affect the time for the onset of aqueous corrosion and, until full saturation is achieved, the rates of the interfacial reactions. Furthermore, the gas storage capacity of the DGR is greater the lower the degree of saturation. The degree of saturation also affects the thermal conductivity of the bentonite.

Two simulations were performed to explore the relative importance of the saturation time, one with a ten times faster saturation rate than assumed for the Base Case and the other with a ten times slower saturation rate, both assuming shale host rock.

The saturation time influences the corrosion rate and, ultimately, the predicted container failure time (Table 4). Figure 28 compares the predicted time dependence of the corrosion rate for the Base Case simulation (saturation time 10,000 a) discussed in detail above and the corrosion rates for the faster and slower saturation rate simulations (saturation times of 1,000 a and 100,000 a, respectively). As described above (see Figure 12), the time dependence of the corrosion rate can be characterised by four stages:

- Stage I: No corrosion as the RH is less than the threshold value for aqueous corrosion
- Stage II: Corrosion rate decreases with time due to the build up of a protective corrosion product layer
- Stage III: Once the minimum interfacial porosity has been established, the corrosion rate increases as the DGR progressively saturates
- Stage IV: Once the maximum threshold RH has been attained, the corrosion rate decreases with time as a result of the decreasing temperature

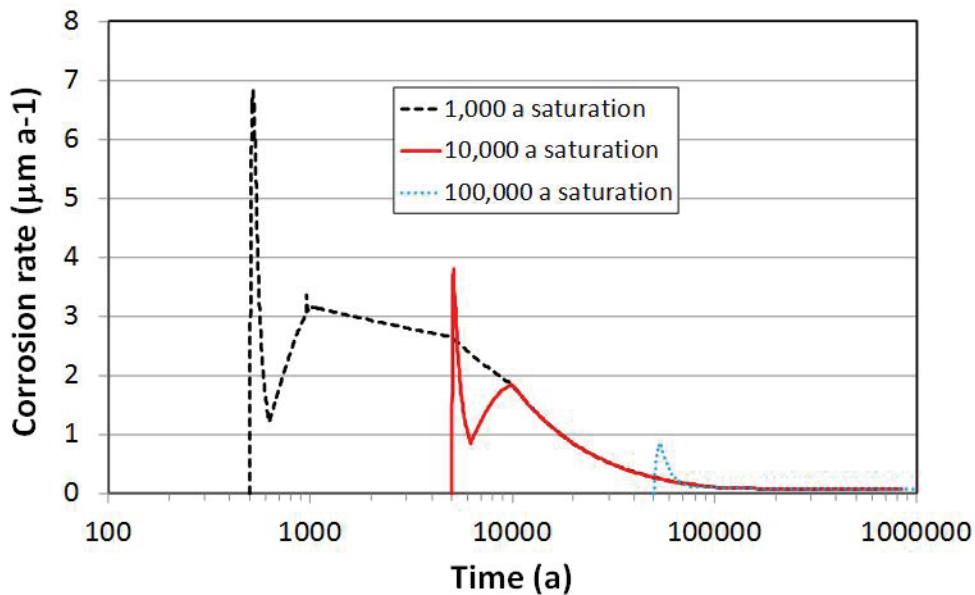


**Figure 28: Effect of Saturation Time on the Predicted Time Dependence of the Corrosion Rate for Shale Host Rock**

The predicted time-dependent corrosion rates for the 1,000-a and 10,000-a saturation periods clearly show these four distinct stages. The peak corrosion rate for the shortest assumed saturation time is higher because the container temperature is higher when the surface first becomes wetted after 500 a.<sup>4</sup> Because of the very slow rate of saturation in the case of the 100,000-a saturation simulation, Stages II and III are not distinguishable and the time-dependent corrosion rate exhibits a single peak.

The different time-dependent corrosion rates result in different predicted container lifetimes (Table 4). Figure 29 shows that the predicted times for penetration of the 2-cm-thick corrosion allowance are 8,200 a, 19,500 a, and 190,000 a, for assumed saturation times of 1,000 a, 10,000 a, and 100,000 a, respectively.

The saturation time also affects the number and rate of gas release events (Figure 30). Based on the simplified treatment of gas release in the SCM V1.0, two to three times as many gas releases are predicted for the fastest saturation time compared with the slowest. The smaller number of gas releases for the slower saturation is primarily a result of the lower corrosion rate rather than any increased gas storage capacity in unsaturated buffer or rock.

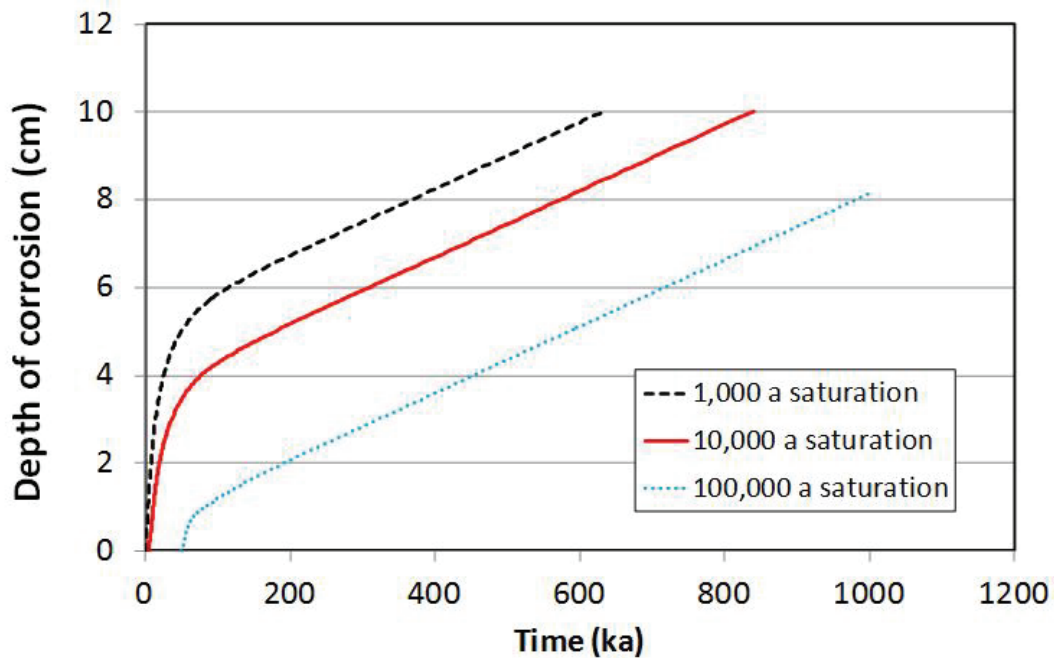


**Figure 29: Effect of Saturation Time on the Predicted Time Dependence of the Depth of Corrosion for Shale Host Rock**

<sup>4</sup> It is interesting to note that, once the DGR is fully saturated in these two cases (at a time of 10,000 a), the predicted corrosion rates are identical, which represents a good check on the reproducibility of the model predictions.

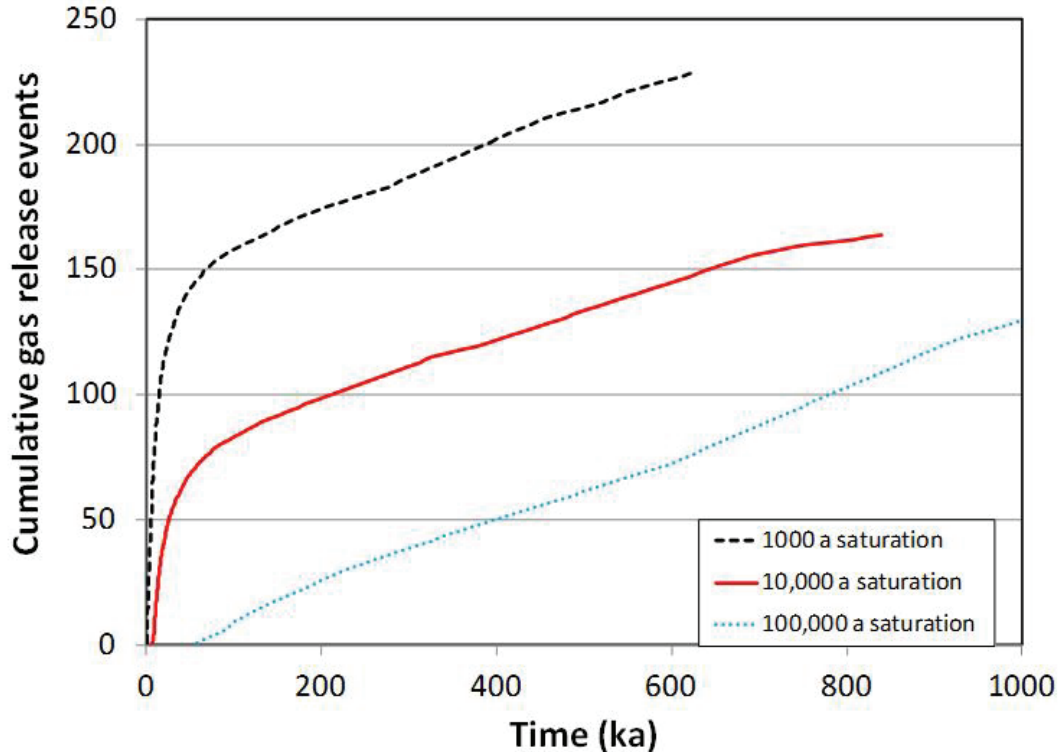


**Figure 30: Predicted Time Dependence of the Release of Hydrogen Gas as a Function of Repository Saturation Time for Shale Host Rock**

#### 4.2.2 Minimum Porosity

The minimum porosity is a modelling construct to simulate the growth of a protective corrosion product layer with a degree of open porosity. An open pore structure can result from hydrolysis and acidification of dissolved metal cations and is consistent with film growth at the film/solution interface. Magnetite films grown on C-steel in simulated repository environments typically exhibit a duplex structure in which an epitaxially grown inner layer is covered by a porous precipitated outer layer (Smart et al. 2001). Long-term steady-state corrosion rates, as commonly observed for C-steel (King 2008), are consistent with the presence of a protective layer of constant porosity. Without this mathematical construct, precipitate (in the model  $\text{Fe}(\text{OH})_2$ ,  $\text{Fe}_3\text{O}_4$ , and/or  $\text{FeCO}_3$ ) would accumulate in the pores until the interfacial porosity dropped to zero and corrosion would stop. Because the precipitated surface film is assumed to be non-conducting it blocks the interfacial electrochemical reactions so that the rate of corrosion is directly impacted by the assumed value for the minimum porosity. The porous layer will also restrict the mass transport of reactants to, and of dissolved corrosion products away from the metal/film interface, thus impacting the formation of  $\text{FeCl}^+$ ,  $\text{FeCO}_3$ , and  $\text{Fe}(\text{CO}_3)_2^{2-}$  and the cathodic reduction of  $\text{HCO}_3^-$ .<sup>5</sup> Because water is not explicitly included in the model, the effect of  $\text{H}_2\text{O}$  availability on the rate of the cathodic reduction of  $\text{H}_2\text{O}$  and the formation of  $\text{FeOH}^+$  and

<sup>5</sup> The minimum porosity is applied throughout the model domain, not just at the corroding interface. Therefore, the value of the minimum porosity will affect the rates of mass transport and other processes throughout the repository but the major effect, and that focussed on here, is the impact on the corrosion rate and associated processes.

$\text{Fe}(\text{OH})_2$  is not specifically modelled, except through the threshold RH for interfacial electrochemical reactions.

In general, the assumption of a higher minimum porosity results in a higher predicted corrosion rate (Table 4). Thus, the predicted container lifetime is reduced to 8,700 a from 19,500 a when the minimum porosity is increased from 0.01 to 0.05. Figure 31 shows the time dependence of the corrosion rates and the ratio of the rates for minimum porosities of 0.05 and 0.01. The peak corrosion rate for the higher porosity is predicted to be  $9.2 \mu\text{m}\cdot\text{a}^{-1}$  and occurs at the point of complete saturation of the DGR, whereas that for the Base Case simulation ( $\epsilon_{\text{MIN}} = 0.01$ ) is  $3.8 \mu\text{m}\cdot\text{a}^{-1}$  and corresponds to the time at which surface precipitation begins. The mean corrosion rate for the high  $\epsilon_{\text{MIN}}$  case (averaged over the predicted container lifetime of 8,700 a) is  $2.3 \mu\text{m}\cdot\text{a}^{-1}$ , compared with the value of  $1.0 \mu\text{m}\cdot\text{a}^{-1}$  averaged over the longer container lifetime for the Base Case simulation.

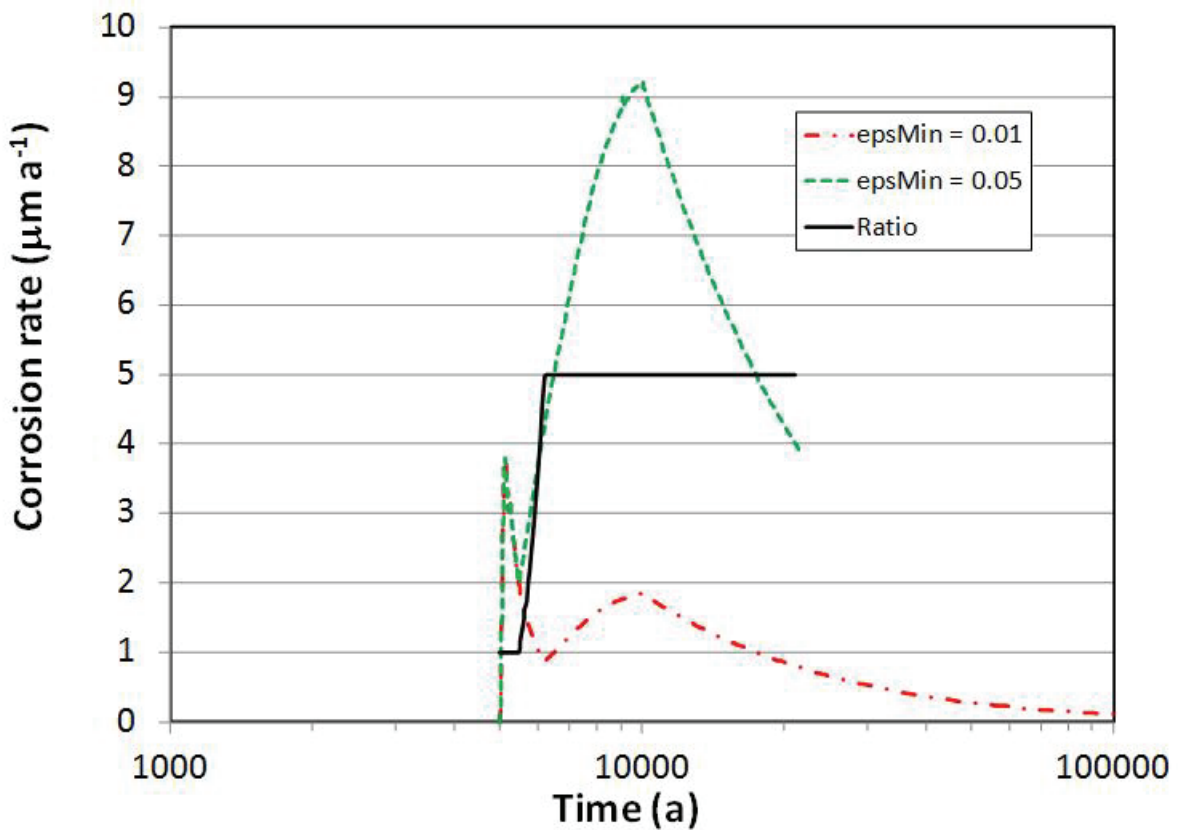


**Figure 31: Comparison of the Predicted Corrosion Rate for the Base Case Simulation for Shale Host Rock ( $\epsilon_{\text{Min}} = 0.01$ ) and the Variant Case With Higher Minimum Porosity ( $\epsilon_{\text{Min}} = 0.05$ ). The ratio of the time-dependent rates is also shown.**

The time dependence of the ratio of the predicted corrosion rates suggests that, in the model, the most important impact of surface film formation is the blocking of the surface electrochemical reactions. The ratio of the rates is equal to one until the minimum porosity of 0.05 is reached for the variant case after 5481 a (Figure 31). This ratio subsequently increases as the interfacial porosity for the Base Case simulation continues to decrease until the minimum value of 0.01 is reached after 6194 a, at which point the ratio of the rates is equal to five and remains at that value for all subsequent times. If film formation affected the corrosion rate by limiting the transport of reactants to, or of corrosion products away from, the corroding surface then the corrosion rate would be expected to be smaller for the high  $\varepsilon_{\text{MIN}}$  variant (i.e., the ratio would be less than one) since the film is much thicker at a given time in that case. The fact that the ratio of the rates is, after the respective values of  $\varepsilon_{\text{MIN}}$  have been attained, equal to the ratio of the minimum porosity values indicates that it is the surface blocking effect that dominates. Furthermore, the interfacial electrochemical reactions (except for the first anodic electron transfer step) are assumed to be irreversible, so that the supply or removal of species would not be expected to have an effect on their rates.

In comparison to the differences in corrosion rate, the time dependence of  $E_{\text{CORR}}$  is identical regardless of the value of  $\varepsilon_{\text{MIN}}$  (not shown). Since the change in surface area due to the precipitation of corrosion products affects the rates of the anodic and cathodic reactions equally, an effect on  $E_{\text{CORR}}$  of the value of  $\varepsilon_{\text{MIN}}$  would not be expected.

#### 4.2.3 Threshold Relative Humidity

Both minimum and maximum threshold relative humidity values are defined in the model. The minimum threshold value defines the RH above which electrochemical reactions are assumed to occur, with no corrosion at lower RH values. The maximum threshold value defines the RH at which the interfacial rate constants are assumed to be equal to those in bulk solution. The values of the interfacial rate constants are pro-rated for RH values between the minimum and maximum, so that the difference between the two threshold values determines the rate of change of the interfacial rate constants with increasing RH.

Two variant simulations were performed for limestone host rock, one with a lower value of the minimum threshold RH and the other with a lower value of the maximum threshold RH. In the case of the lower minimum threshold RH ( $h_{k,\text{min}} = 0.2$ , instead of 0.6 for the Base Case simulation), corrosion can be expected to occur earlier but with a slower increase in the interfacial rate constants. The lower value of  $h_{k,\text{min}}$  is consistent with the presence of a highly deliquescent salt (e.g.,  $\text{MgCl}_2$  or  $\text{CaCl}_2$ ) on the container surface, rather than a less-deliquescent salt, such as  $\text{NaCl}$ , implicitly assumed for the Base Case. A lower maximum threshold RH ( $h_{k,\text{max}} = 0.7$ , instead of 1.0 for the Base Case) simulates rapid wetting of the surface, as might occur for a salt-contaminated porous surface where condensation occurs due to both deliquescence and capillary effects. In this case, once corrosion starts, the transition to the maximum rate of the interfacial rate constants (defined by the end of Stage III, Figure 12) will occur sooner than for the Base Case simulation.

Changes in the threshold RH values have a number of effects on the predicted corrosion behaviour (Table 4). As expected, lowering either the minimum RH at which corrosion can occur or the value of  $h_{k,\text{max}}$  both result in higher mean corrosion rates and shorter container lifetimes than for the Base Case simulation. Figure 32 shows the predicted time dependence of the corrosion rate for the limestone host rock Base Case simulations and for the two threshold RH variants, for times up to 20,000 a. The lower  $h_{k,\text{max}}$  value results in not only a higher peak

corrosion rate but also a higher corrosion rate after attainment of the maximum interfacial rate constants (equivalent to Stage IV in Figure 12) because of the higher temperature at shorter times compared with the equivalent Stage IV period for the Base Case simulation.

Figure 33 shows the predicted time-dependent depths of corrosion for the three simulations, illustrating the shorter container lifetimes discussed above (based on complete penetration of the assumed 2-cm wall thickness).

Since the threshold RH values do not affect the relative anodic and cathodic surface areas, the time-dependent  $E_{CORR}$  values are identical for all three simulations (Figure 34).

Lastly, Figure 35 shows a comparison of the number of predicted gas release events for the three simulations.

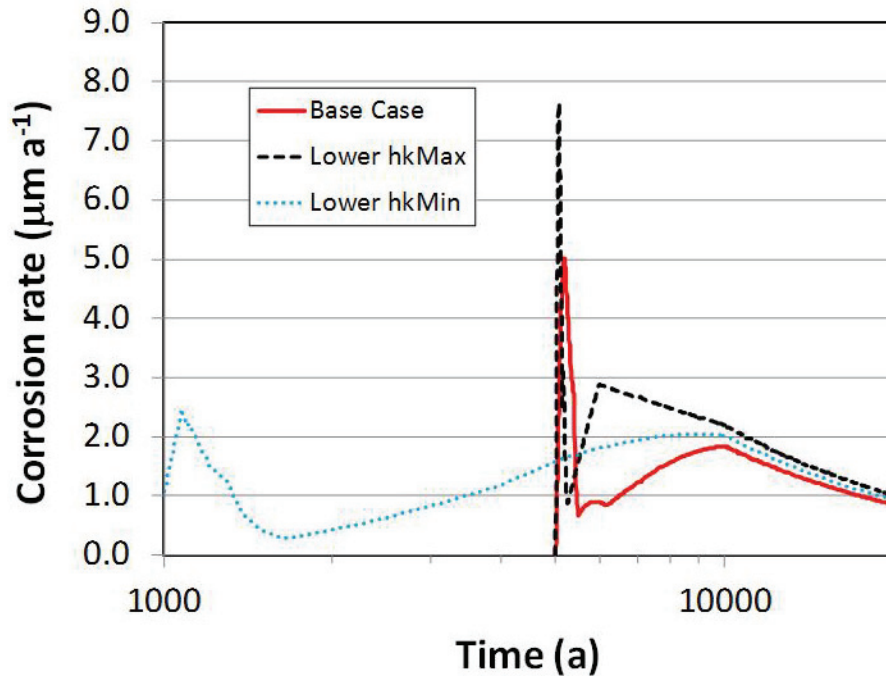


**Figure 32: Comparison of the Effect of Threshold Relative Humidity for the Interfacial Electrochemical Reactions on the Predicted Time Dependence of the Corrosion Rate for Limestone Host Rock**

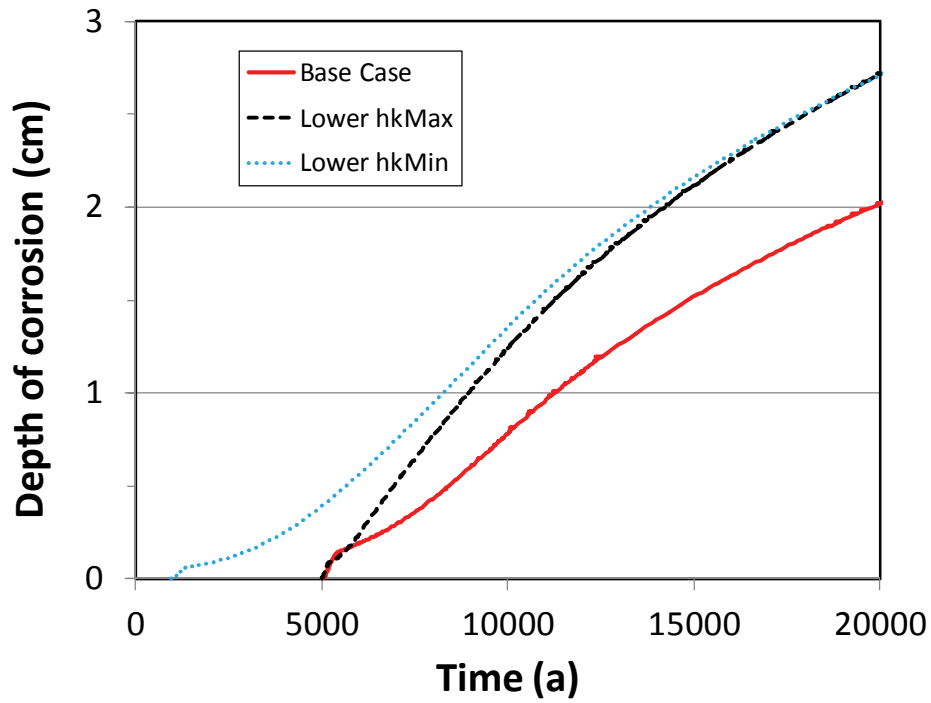


Figure 33: Comparison of the Effect of Threshold Relative Humidity on the Predicted Depth of Corrosion for Limestone Host Rock

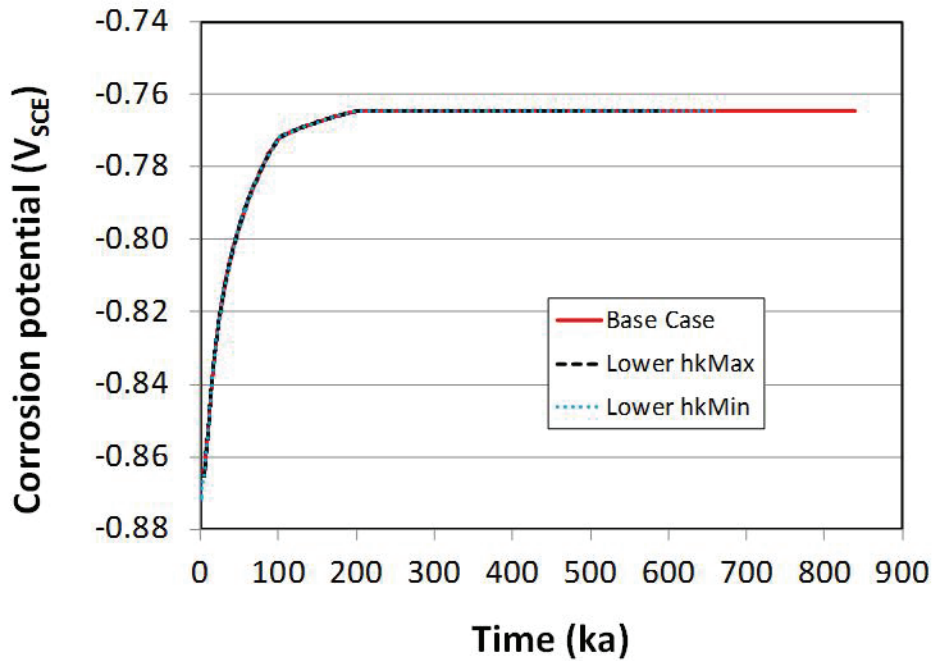
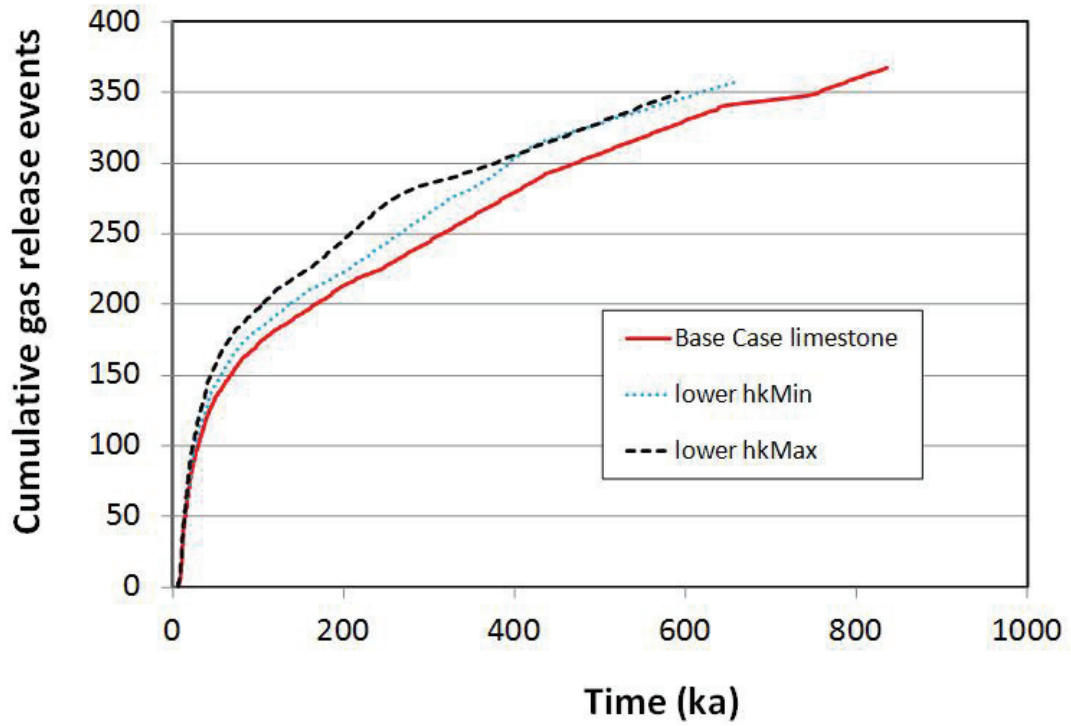


Figure 34: Comparison of the Effect of Threshold Relative Humidity on the Predicted Time Dependence of the Corrosion Potential for Limestone Host Rock



**Figure 35: Effect of Relative Humidity Thresholds on the Predicted Time Dependence of Gas Release Events for Limestone Host Rock**

## 5. DISCUSSION

Although primarily developed as a model to predict the long-term anaerobic corrosion behaviour of the container, the SCM V1.0 can also be used to predict other features of the repository environment, in particular the production and release of H<sub>2</sub> gas and the alteration of the clay by reaction with Fe(II). Here the results of the simulations performed are first discussed, followed by a more detailed discussion of the prediction of the corrosion behaviour of the container. Next, the SCM is compared with other models designed to predict the interaction between C-steel containers and the near-field and far-field environments. Finally, potential future developments and improvements to the model are discussed.

### 5.1 GENERAL OBSERVATIONS

#### 5.1.1 Effect of Host Rock Type

Based on the results of the two Base Case simulations performed here, the corrosion behaviour of the container is expected to be similar regardless of whether the repository is located in shale or limestone host rock. In the SCM simulations, the only differences between the two types of host rock are (i) slight differences in the respective thermal properties, (ii) lower porosity of the limestone, and (iii) a significantly higher CaCO<sub>3</sub> content in limestone than in shale. In the absence of information to the contrary, the pore-water composition and the DGR saturation times for the two types of rock were assumed to be the same.

Based on these differences, it is not surprising that the model predicted similar container corrosion behaviour for the two host rocks. In general, the corrosion behaviour of the container is determined more by the properties of the near field (i.e., the bentonite) than the far field. The bentonite controls the concentration of HCO<sub>3</sub><sup>-</sup> (through equilibrium with calcite) and the supply of Cl<sup>-</sup> ions. In turn, dissolved Fe(II) is retarded from migrating into the far-field (even over the extended time periods of interest here) by the low porosity of the bentonite, adsorption of corrosion products, and (in the case of Fe(II)), reaction with and alteration of the clay. The assumption that the rate of saturation is the same for both host rock types is perhaps the major factor that results in similar predicted corrosion behaviour in shale and limestone host rocks. If saturation times are different for shale and limestone, for example, due to differences in hydraulic conductivity, then the model would predict different corrosion behaviour. In contrast, the fact that limestone has a higher calcite content than shale is irrelevant as the availability of calcite in the host rock does not impact the pore-water HCO<sub>3</sub><sup>-</sup> concentration at the container surface.

#### 5.1.2 Effect of Saturation Time

The DGR saturation time is an uncertain parameter and for that reason was treated as a variable in the sensitivity analyses performed here. Saturation times (defined as the time to achieve 99% saturation of the bentonite closest to the container) of 1,000 a, 10,000 a, and 100,000 a were assumed. Clearly, if the saturation time is delayed then so too is the onset of corrosion which in turn will result in longer container lifetimes. The greatest impact of delayed saturation results if the container surface remains dry for the period corresponding to the thermal pulse (of the order of 100,000 a, Appendix A.2). Based on the data in Table 4, a 100-fold increase in saturation time from 1,000 a to 100,000 a results in an approximate 20-fold increase in the predicted container lifetime (based on a 2-cm corrosion allowance).

### 5.1.3 Effect of Minimum Porosity

It is well known that the corrosion rate of C-steel under repository conditions decreases with time due to the formation of a protective surface film (King 2008, Smart et al. 2001). It is also apparent that a near-constant corrosion rate is established in long-term experiments, consistent with a protective film that retains some open porosity to permit continued corrosion (Bignold et al. 1972). In the SCM V1.0, that film growth process is modelled by allowing corrosion product to precipitate (largely in the form of  $\text{Fe}_3\text{O}_4$ ) where it is created.<sup>6</sup> Precipitation results in a reduction in the porosity of the bentonite into which the precipitated corrosion product penetrates, subject to an assumed minimum porosity  $\epsilon_{\text{MIN}}$ . If a minimum porosity is not imposed precipitation continues until the interfacial reactions on the surface are blocked by precipitated corrosion product.<sup>7</sup>

Because the minimum porosity defines the maximum extent to which the container surface can be blocked, the value of  $\epsilon_{\text{MIN}}$  is a key modelling parameter. For the Base Case simulations, a default value for  $\epsilon_{\text{MIN}}$  of 0.01 was used, with an increased value of 0.05 used in a variant simulation. As shown in Figure 31 and in Table 4, the value of  $\epsilon_{\text{MIN}}$  has a significant effect on the predicted corrosion rate and, for the assumed saturation time and temperature profile and container thickness, an even greater impact on the predicted lifetime. Once the container surface is completely covered by corrosion product (subject to the minimum interfacial porosity), the corrosion rate is proportional to the value of  $\epsilon_{\text{MIN}}$  resulting in a five-fold higher corrosion rate for the variant case.

Clearly, therefore, for the assumed conditions used here, the value of the minimum porosity has a significant impact on the predicted container lifetime. There are few measurements of the porosity of precipitated corrosion product films in the literature. Stroes-Gascoyne et al. (2000) attempted to measure the porosity of Fe corrosion products formed at 95°C using mercury intrusion porosimetry on samples removed from the test environment. However, the reported porosity of 50% probably reflects artifacts introduced during the removal and drying of the specimens rather than the actual porosity of the corrosion products. Deposits formed in steam generators are reported to exhibit a porosity of 5-10% (Baum and Evans 2005), to as high as 50% (Uhle 1997). Such porous deposits are not consistent with the exponential decrease in corrosion rate of C-steel exposed to simulated groundwater solutions reported by Smart et al. (2001). Instead, the similarity between the predicted corrosion rates in the Base Case simulations and those reported experimentally (King 2008) imply that a more-realistic value of the minimum porosity is of the order of 0.01.

### 5.1.4 Effect of Threshold RH Values

It is well established that corrosion in unsaturated conditions occurs above a threshold RH that depends primarily on the nature of the surface contaminant (Cole et al. 2004). This threshold

---

<sup>6</sup> An alternative approach, used in some earlier models (King and Kolar 1999, 2001), is to collect all precipitate regardless of where it is formed and deposit it at the film/solution interface. This approach is appropriate if it is known that film growth occurs at this location.

<sup>7</sup> An explicit assumption is that the corrosion product is electrically insulating and does not support electrochemical reactions.

RH corresponds to the point at which an aqueous phase forms on the surface capable of supporting electrochemical reactions. With increasing RH, the thickness and, if the surface contaminants are not extensively distributed, the surficial extent of this water layer increases. At some value of the RH, the surface water layer is sufficiently thick that it is essentially equivalent to a bulk liquid environment.

In order to represent the effect of these changes in the degree of wetness on the rates of surface electrochemical processes, a minimum and a maximum threshold RH are defined in the SCM. The minimum threshold RH represents the point at which the surface wets, so that the rate of electrochemical reactions is zero at lower humidity values. The maximum threshold RH represents the point at which the surface environment is equivalent to a bulk solution, so that the electrochemical rate constants are assigned values equal to those in solution. Between these two threshold RH values, the values of electrochemical rate constants are varied linearly. This linear decrease in electrochemical rate constant with decreasing RH simulates the potential limitation of the interfacial reactions due to the availability of water.

Varying the minimum and maximum threshold RH values results in subtle changes to the predicted time dependence of the corrosion rate (Figure 32), but makes relatively little difference to the predicted container lifetimes (Table 4). Thus, uncertainty in the nature of the surface salt contaminants (which will affect the value of the minimum threshold RH) or of the degree of surface roughness and porosity as a result of a prior period of aerobic corrosion (which will affect the extent of capillary condensation and, therefore, the maximum threshold RH) is relatively unimportant (for the particular modelling assumptions made here).

## 5.2 PREDICTION OF CONTAINER CORROSION

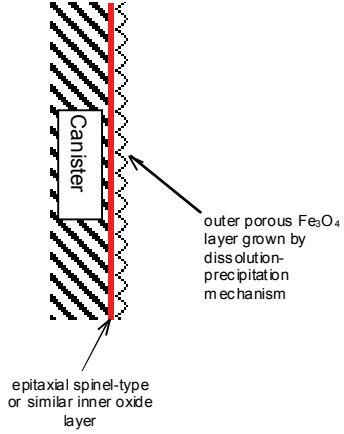
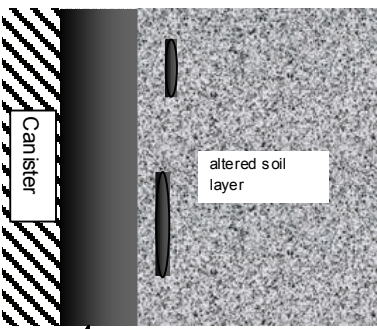
As noted above, the SCM has been primarily developed to predict the anaerobic corrosion behaviour of C-steel containers in a DGR. As such, it is interesting to compare the predicted corrosion behaviour with that observed experimentally in the laboratory and with information derived from long-term analog studies.

The characteristics of the predicted corrosion behaviour can be summarised as follows:

- After full saturation of the bentonite, the corrosion rate decreases with time as a result of the formation of a protective surface film and the decrease in container surface temperature.
- The mean corrosion rate for the Base Case simulations is  $1.0 \mu\text{m}\cdot\text{a}^{-1}$ , resulting in a container lifetime of 19,500 a (based on a 2-cm corrosion allowance).
- The maximum corrosion rate is of the order  $5\text{-}10 \mu\text{m}\cdot\text{a}^{-1}$ , depending upon the modelling assumptions.
- The principal solid corrosion product is  $\text{Fe}_3\text{O}_4$ , with only small amounts of  $\text{FeCO}_3$  and  $\text{Fe}(\text{OH})_2$ .
- Anodic dissolution of C-steel is supported primarily by the cathodic reduction of  $\text{H}_2\text{O}$ , with the reduction of  $\text{HCO}_3^-$  accounting for only 0.03% of the total amount of corrosion.
- The corrosion potential is characteristic of corrosion under anaerobic conditions.
- The value of  $E_{\text{CORR}}$  shifts to more-positive potentials with time as a result of the decrease in temperature.
- The principal effect of the precipitated corrosion product on the corrosion behaviour is to block the interfacial dissolution reactions.

- A  $\text{Fe}_3\text{O}_4$  “front” extends some tens of cm into the bentonite buffer after a period of several hundred thousand years, reducing the porosity in the near field.
- Ferrous ions are sorbed on the bentonite and promote alteration of montmorillonite for a distance of some tens of cm from the canister surface after a period of several hundred thousand years.
- Hydrogen gas is generated and periodically released from the repository.

The anaerobic corrosion behaviour of C-steel under conditions similar to those expected in the repository have been studied in the laboratory (King 2008, Smart et al. 2001) and through the use of archaeological analogs (Crossland 2005; Féron et al. 2009; Neff et al. 2005, 2006; Saheb et al. 2008; Yoshikawa et al. 2008). King (2008) has compared the observed corrosion behaviour in bulk solution and compacted bentonite (Figure 36). In both cases, the corrosion rate decreases with time, although the rate of decrease is faster in bulk solution and results in lower corrosion rates (of the order of  $0.1 \mu\text{m}\cdot\text{a}^{-1}$ , Kreis and Simpson 1992, Smart et al. 2001) than in the presence of compacted bentonite (of the order of  $1 \mu\text{m}\cdot\text{a}^{-1}$ , Papillon et al. 2003, Taniguchi et al. 2004). The main corrosion product in bulk solution is a duplex  $\text{Fe}_3\text{O}_4$  film with an outer porous layer over an inner compact film. In bentonite environments,  $\text{FeCO}_3$  is observed, which can also contain cations from the pore solution. The bentonite in contact with the steel surface is typically discoloured and found to contain precipitated corrosion products (Papillon et al. 2003, Xia et al. 2005).

	Bulk solution	Compacted clay
Corrosion rate and time dependence	$\sim 0.1 \mu\text{m y}^{-1}$ Steady-state after 4-6 months	$\sim 1 \mu\text{m y}^{-1}$ Still decreasing after 4 y
Corrosion products: composition and structure	Duplex spinel-type/ $\text{Fe}_3\text{O}_4$ structure 	Corrosion product layer containing $\text{FeCO}_3$ /(Fe,Ca) $\text{CO}_3$ and adjoining altered soil layer 

**Figure 36: Comparison of the Anaerobic Corrosion Behaviour of Carbon Steel in Bulk Solution and Compacted Bentonite (Johnson and King 2008, King 2008)**

Analysis of archaeological artifacts shows similar behaviour. Corrosion rates are approximately an order of magnitude higher in soil environments than in solution, being of the order of 1-10  $\mu\text{m}\cdot\text{a}^{-1}$  and 0.1-1  $\mu\text{m}\cdot\text{a}^{-1}$ , respectively (Figures 37 and 38). Furthermore, in addition to a layer of corrosion products (referred to by Neff et al. 2005 as a “dense product layer”), the soil closest to the objects contains precipitated corrosion products (referred to by Neff et al. 2005 as “transformed medium”) (Figure 39).

The results of the SCM simulations are in good agreement with the laboratory observations and analog studies. The predicted corrosion rates fall within the range observed for laboratory coupons and archaeological artifacts in contact with compacted bentonite or soil. The formation of a corrosion product layer which limits the rate of corrosion is also observed, although a carbonate-based film is generally reported as opposed to the  $\text{Fe}_3\text{O}_4$  film predicted to form in the SCM simulations. Transformation of the soil or bentonite layer is also commonly observed in experimental and analog studies. Xia et al. (2005) also report evidence of gas transport through compacted bentonite in contact with corroding C-steel.

A fundamental feature of the manner in which the anaerobic corrosion of C-steel is modelled in the SCM V1.0 is the treatment of the corrosion product film as a porous layer with a minimum porosity. Electrochemical reactions are assumed to occur at the metal/film interface, with the dual roles of the precipitated layer being to restrict mass transport and to reduce the area available for electrochemical reactions. In bulk solution, there is some evidence to suggest that the corrosion rate is limited by transport (of either cationic or anionic species) across the inner thin oxide layer, but it is unclear whether the same mechanism holds in bentonite systems

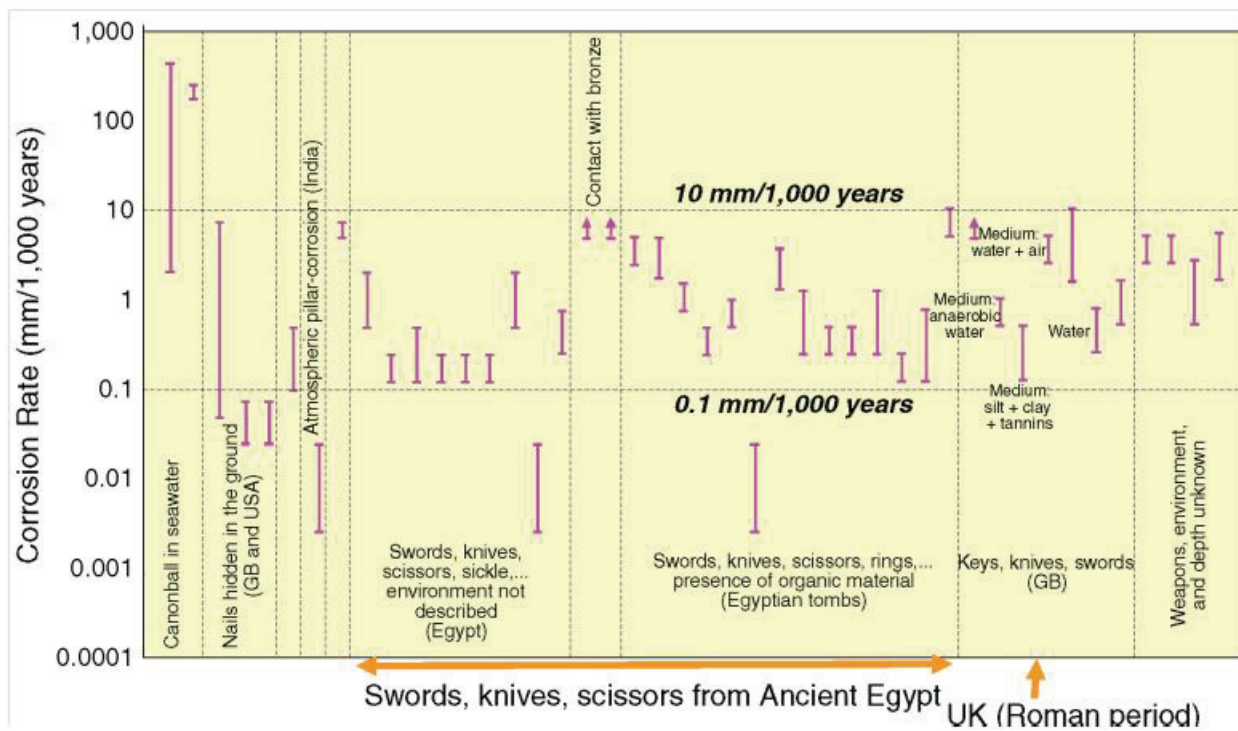
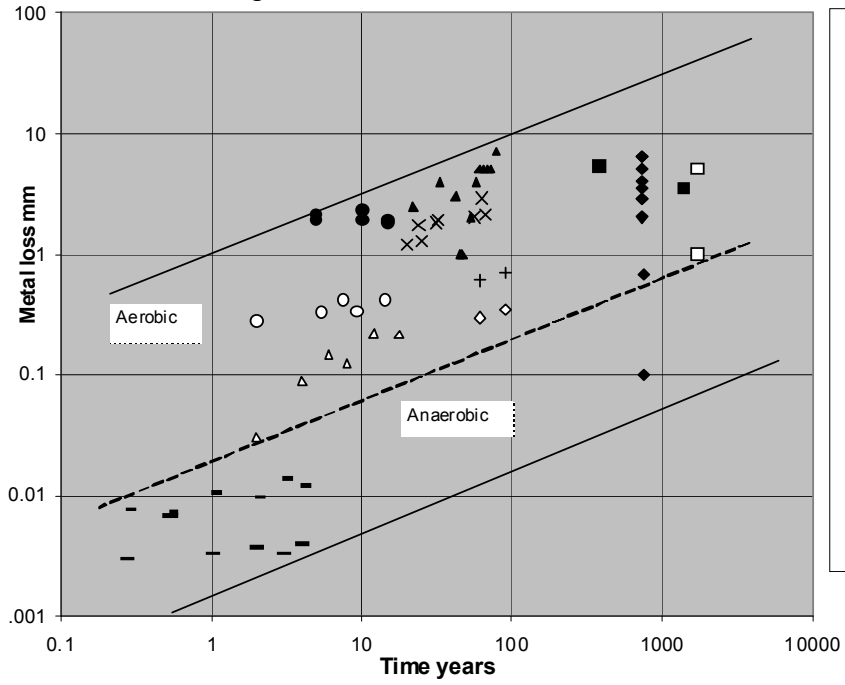
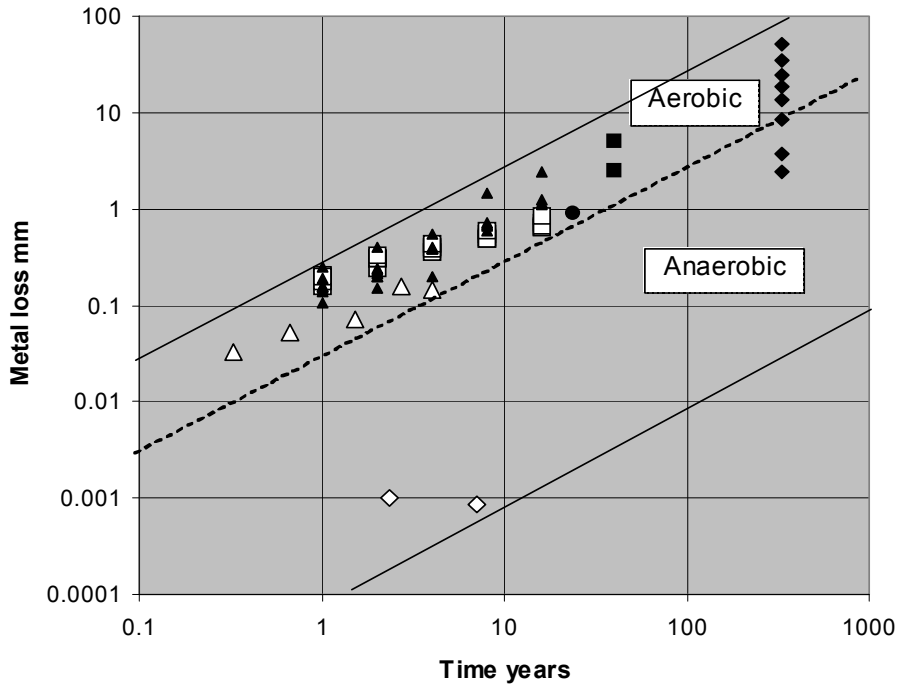


Figure 37: Corrosion Rates of Buried Archaeological Iron Objects (Féron et al. 2009)



(a) Soil



(b) Bulk solution

Figure 38: Corrosion Rates of Carbon Steel and Cast Iron from Archaeological Analogs (Crossland 2005)

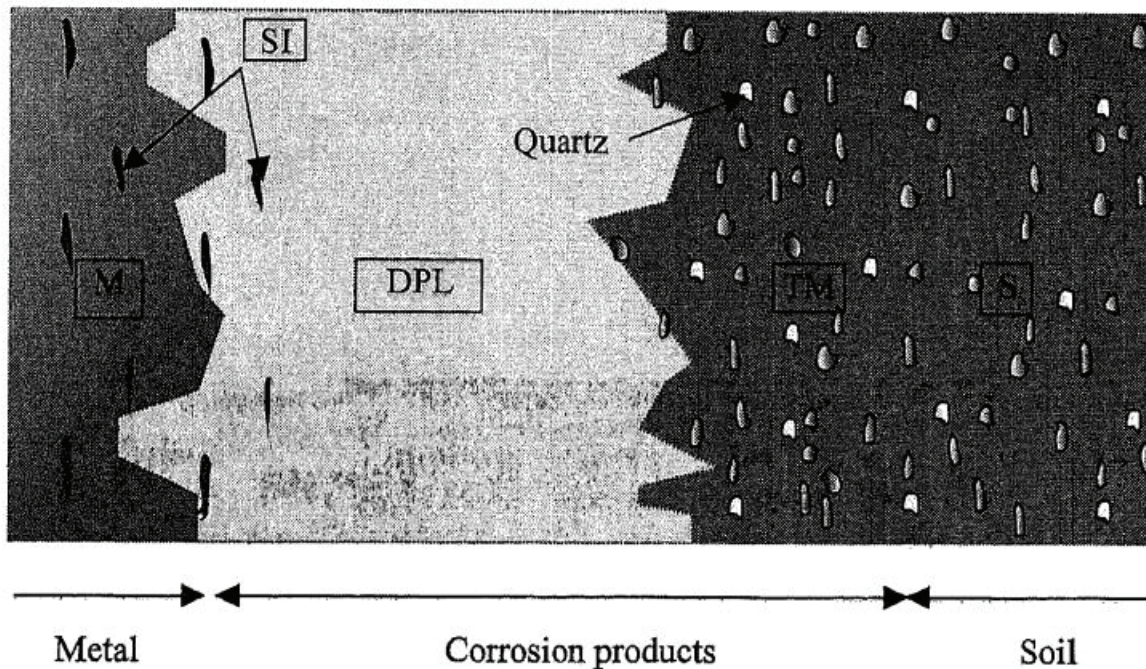


**Figure 39: Schematic Illustration of the Characteristics of Corroded Archaeological Iron Objects in Soil (Neff et al. 2005). M: metal, SI: slag inclusions, DPL: dense product layer, TM: transformed medium, S: soil.**

because the nature of the corrosion product film is fundamentally different. The observation that the predicted corrosion rates are similar to those observed in the laboratory (or inferred from analog studies) is not sufficient evidence to claim that the corrosion rate is controlled by the blocking effect of the precipitated corrosion product (as indicated by the modelling studies). However, it is interesting to note that combining electrochemical kinetics from studies on bare surfaces with reasonable estimates for the porosity of surface films leads to predicted corrosion rates that are similar to those observed experimentally.

In addition to being a predictive tool, the SCM model can also be used to identify key pieces of missing information for future experimental studies. First, there is a clear need to establish the reaction mechanism and the nature of the rate-determining step for the corrosion of C-steel in compacted bentonite. Second, additional work is required to establish the temperature dependence of the anaerobic corrosion rate in compacted bentonite systems. The model predicts a significant effect of temperature but there are no systematic studies in compacted bentonite systems reported in the literature (King 2008). Finally, should the use of a porous layer model be found suitable to describe the corrosion mechanism, further work is required to measure the porosity of such films.

### 5.3 CONTAINER LIFETIMES

The predicted container lifetime depends on the assumed corrosion allowance. Typically, the corrosion allowance is that part of the container wall thickness not required to provide structural strength. Container failure is assumed to occur due to mechanical overload once the corrosion allowance has been consumed.

Table 5 summarises the predicted container lifetimes for the Base Case simulation with shale host rock for a range of corrosion allowances from 1 cm to 10 cm. Because the corrosion rate decreases with time, very long lifetimes are predicted with the larger corrosion allowances. The mean corrosion rates given in Table 5 are estimated based on the time since emplacement of the containers. Because no corrosion occurs for the first 5,000 a (because the surface RH is below the threshold value for corrosion), the mean corrosion rate does not vary systematically with the corrosion allowance.

**Table 5: Predicted Container Lifetime as a Function of the Corrosion Allowance\***

Corrosion allowance (cm)	Container lifetime (a)	Mean corrosion rate ( $\mu\text{m}\cdot\text{a}^{-1}$ )
1	11,200	0.89
2	19,500	1.0
3	36,500	0.82
10	840,000	0.12

\* For the Base Case simulation with shale host rock assuming insignificant corrosion during the aerobic phase.

### 5.4 COMPARISON WITH PREVIOUS MODELLING STUDIES

Whilst the best test of the validity of the SCM V1.0 simulations is a comparison with the corrosion behaviour observed in laboratory experiments and derived from the study of archaeological analogs, it is also interesting to compare the model predictions with those from other modelling studies.

There have been a number of previous modelling studies of DGR systems comprising a C-steel container, bentonite buffer, and either sedimentary or granite host rock. These studies have been primarily performed in support of the French (Bildstein et al. 2006, de Combarieu et al. 2007, Marty et al. 2010) and Spanish (Lu et al. 2011, Samper et al. 2008) national programs, although work has also been done to analyse the possible impact of a C-steel supercontainer shell for the Finnish KBS-3H repository design (Wersin et al. 2007). The key aspects of these models are compared with those of the SCM V1.0 in Table 6.

Each of these models exhibits particular strengths and weaknesses depending on the primary focus of the model and the background of the model developer(s). Many of the models are derived from or use thermodynamically based geochemical models such as PHREEQ and EQ3/6. As a consequence, all of the models (except the SCM) incorporate detailed thermodynamic modelling of the pore-water chemistry and of mineral dissolution-precipitation processes (Bildstein et al. 2006, de Combarieu et al. 2007, Lu et al. 2011, Marty et al. 2010, Samper et al. 2008, Wersin et al. 2007). This modelling approach is useful if the primary focus of the model is to predict clay alteration.

All of the models except the SCM consider fully saturated, isothermal systems. Thus, although it is acknowledged in some of the models that anaerobic corrosion results in H<sub>2</sub> generation, the SCM is the only model to predict the development of H<sub>2</sub> overpressures and the transport of gas through the repository. The SCM is also the only model that treats the effect of thermal gradients.

There are significant differences between the models in their treatment of corrosion processes. Apart from the SCM, all of the other models assume either a constant corrosion rate or treat the corrosion process in a similar manner to a mineral dissolution reaction resulting in a quasi time dependence. For example, Lu et al. (2011) assumed that the reaction



proceeded to the right (i.e., that corrosion occurred) until the ion activity product  $a_{\text{Fe}^{2+}} a_{\text{OH}^-}^2 / a_{\text{H}_2\text{O}}^2$  (where  $a_i$  is the activity of species  $i$ ) equals the corresponding equilibrium constant. Presumably because H<sub>2</sub> was not included in the model, Lu et al. (2011) (and Samper et al. 2008 in their earlier version of this model) re-wrote Reaction (23) as



which makes no mechanistic sense. Regardless of the adopted stoichiometry, the result of this approach is that corrosion is predicted to stop once the product of the activities of the corrosion products reaches equilibrium. The mistake that Lu et al. (2011) make is in using reversible equilibrium expressions to treat an irreversible kinetic phenomenon. The anaerobic corrosion of C-steel does not occur anywhere near equilibrium conditions and is, in fact, an irreversible process. As a consequence of this unusual treatment of the corrosion process, Lu et al. (2011) predicted a mean corrosion rate of 0.007  $\mu\text{m}\cdot\text{a}^{-1}$ .

A common prediction of these thermodynamically based reactive-transport models is that the pH at the container surface becomes alkaline (Bildstein et al. 2006, de Combarieu et al. 2007, Lu et al. 2011, Marty et al. 2010, Samper et al. 2008). For example, Figure 40 shows the time dependence of the interfacial pH predicted by Bildstein et al. (2006). The increase in pH is reported to be a consequence of the OH<sup>-</sup> ions produced by the reduction of H<sub>2</sub>O (Reaction (23)). However, in bulk solution at least, the dissolved Fe<sup>2+</sup> precipitates as some form of solid corrosion product resulting in no net change in pH, for example,



or



Because much of the dissolved Fe(II) is predicted to precipitate as Fe<sub>3</sub>O<sub>4</sub> in the various models, it is somewhat surprising that an alkaline interfacial pH is predicted. This prediction is also inconsistent with the experimental observation that C-steel corrodes actively in compacted bentonite (JNC 2000), since an interfacial pH >10 would be expected to induce passivity of C-steel. Because of the implications of a passive container surface in terms of the increased probability of localised corrosion or stress corrosion cracking, it is important to establish whether alkaline conditions are generated at the container surface.

**Table 6: Comparison of Features of Various Models for the Carbon Steel-Bentonite System**

	<b>SCM (this report)</b>	<b>Bildstein et al. (2006)</b>	<b>de Combarieu et al. (2007)</b>	<b>Wersin et al. (2007)</b>	<b>Samper et al. (2008), Lu et al. (2011)</b>	<b>Marty et al. (2010)</b>
Code	Custom-designed finite difference code based on TRANSIENT solver	CRUNCH	CHESS	CRUNCHFlow	Custom-designed CORE <sup>2D</sup> V4 finite element code, thermodynamic data from EQ3/6	KIRMAT
Dimensionality	1-D	1-D	Single compartment model	1-D	1-D and 2-D axisymmetric	1-D
Duration of simulation	Up to 1 Ma	10,000 a	200 d	0.5 Ma	0.3 Ma	0.1 Ma
Barriers included	Container, bentonite, EDZ, sedimentary host rock	Container, bentonite, argillaceous host rock	Container, bentonite	Container, bentonite	Container, bentonite, EDZ, granite host rock	Container, bentonite
Number of nodes/elements	392	Not stated	1	20	200 (1-D) 1820 (2-D)	20
Corrosion processes	Electrochemical boundary conditions, mixed-potential model, corrosion rate predicted by code, effect of surface films	Assume constant rate ( $4.3 \mu\text{m}\cdot\text{a}^{-1}$ )	Assume constant rate ( $1.3 \mu\text{m}\cdot\text{a}^{-1}$ )	Constant [Fe(II)] or time-dependent rate	Constant rate of $0.2 \mu\text{m}\cdot\text{a}^{-1}$ (Samper et al. 2008), time-dependent rate (Lu et al. 2011)	Initial rate of $5 \mu\text{m}\cdot\text{a}^{-1}$ , time-dependent due to assumption of equilibrium and limited mass transport
Mass transport	Diffusion	Diffusion	None	Diffusion	Diffusion (plus advection in host rock for 2-D case)	Diffusion

	<b>SCM (this report)</b>	<b>Bildstein et al. (2006)</b>	<b>de Combarieu et al. (2007)</b>	<b>Wersin et al. (2007)</b>	<b>Samper et al. (2008), Lu et al. (2011)</b>	<b>Marty et al. (2010)</b>
Reaction kinetics/ equilibrium	Kinetic, equilibrium for solubility only	Combination of kinetics and equilibrium	Combination of kinetics and equilibrium	Combination of kinetics and equilibrium	Equilibrium	Combination of kinetics and equilibrium
Pore-water chemistry	Limited to Cl <sup>-</sup> , HCO <sub>3</sub> <sup>-</sup> , and corrosion products only	Comprehensive thermodynamic speciation modelling				
Temperature	Fully coupled	Isothermal (50°C)	Isothermal (90°C)	Isothermal (25°C)	Isothermal (25°C)	Isothermal (100°C)
Saturation	Time-dependent saturation (external input)	Fully saturated				
Gas phase	Yes	No	No	No	No	No
Porosity changes	Yes	Yes	No	Yes	Yes	Yes
Adsorption of Fe(II)	Yes	Unclear	No	Yes	Yes (and other cations)	No
Clay alteration	Yes	Yes	Yes	Yes	No	Yes
Hydrogen issues	Generation and transport	Not considered	Not considered	No	H <sub>2</sub> not included in model	Not considered

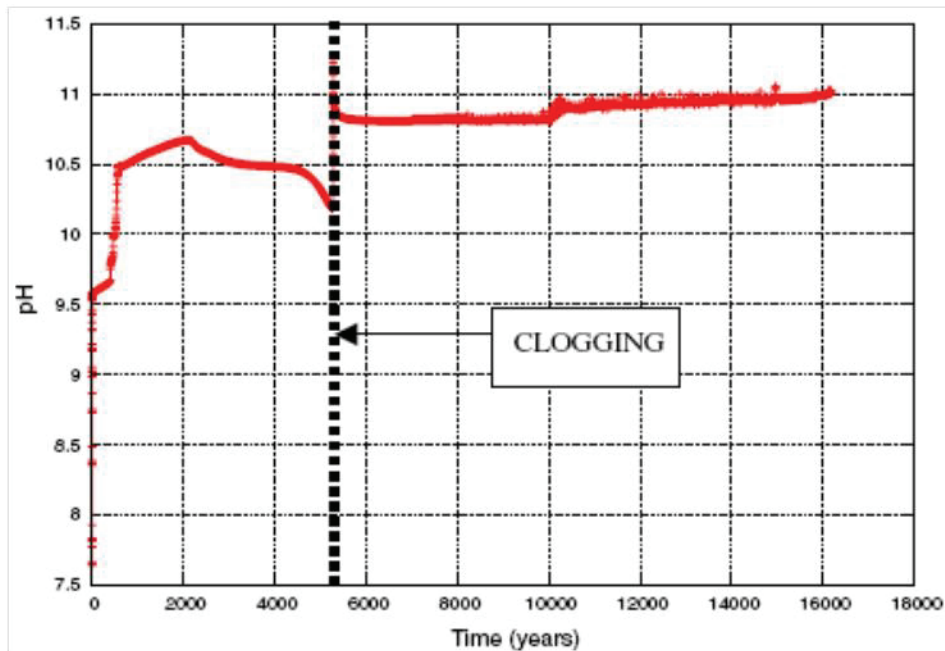


**Figure 40: Predicted Time Dependence of the pH at the Container-Bentonite Interface (Bildstein et al. 2006)**

Many of the models, including the SCM, predict a decrease in porosity of the bentonite due to the precipitation of  $\text{Fe}_3\text{O}_4$  and other corrosion products (the term “clogging” in Figure 40 refers to the time at which the pore space at the container surface becomes filled with corrosion product). Figure 41 shows the spatial distribution of the volume fraction of the original montmorillonite (and quartz) and of various corrosion and alteration products for various times predicted by Marty et al. (2010). (In these simulations, the container is located at the right-hand side of the figures, with a constant ground water composition maintained at the left-hand boundary). The region of reduced porosity extends some 15 cm from the container surface after a period of 100,000 a, compared with a distance of ~20 cm after the same period in the SCM V1.0 Base Case simulation (Figure 16). Whilst the reduction in porosity in the SCM simulation was due mainly to  $\text{Fe}_3\text{O}_4$  formation (Figure 15), Marty et al. (2010) also predict volume changes due to extensive mineral alteration processes near the container surface. Marty et al. (2010) also predict extensive illitisation of the bentonite near the ground water-bentonite interface. The extensive nature of the clay alteration processes is a result, in large part, to the assumption of a constant temperature of  $100^\circ\text{C}$  throughout the simulation. At lower temperatures, or with the time-dependent temperature predicted by the SCM, the extent of mineral alteration is much less. For example, Wersin et al. (2007) predicted  $<1\%$  alteration of the montmorillonite to berthierine after 500,000 a at a constant temperature of  $25^\circ\text{C}$ . For comparison, a maximum of approximately 13% conversion of montmorillonite to berthierine was predicted for the Base Case SCM V1.0 simulation for a maximum container surface temperature of  $118^\circ\text{C}$  (Figure 18).

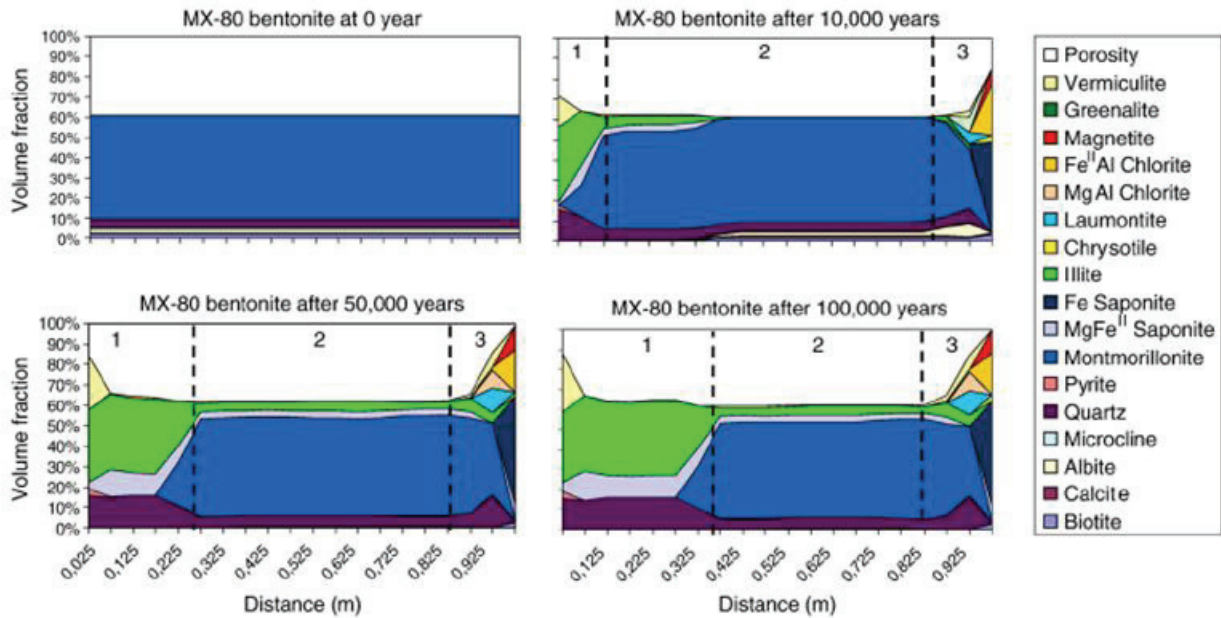


**Figure 41: Predicted Spatial Variation of the Volume Fraction of Original Clay Components and Corrosion and Alteration Products (Marty et al. 2010)**

With the exception of the SCM, none of the other models listed in Table 6 treat the generation or transport of  $H_2$  gas. The SCM V1.0 treats the generation and transport of  $H_2$  based on a number of simplifying assumptions. For example, the transport of  $H_2$  is based on the known transport mechanisms for compacted bentonite (Harrington and Horseman 1999, 2003; Horseman et al. 1999) in which gas is released once a pressure equivalent to the sum of the bentonite swelling pressure (assumed here to be 3 MPa) and hydrostatic head (assumed to be 5 MPa) is exceeded. An amount of gas sufficient to reduce the pressure to 5 MPa is removed from the system, at which point the gas pathways created in the bentonite are assumed to reseal and the procedure repeats. Thus, the  $H_2$  partial pressure in the repository varies between 5 and 8 MPa. In order to be able calculate a  $H_2$  pressure, it is assumed that the bentonite and host rock saturate to a maximum of 99%, with the remaining 1% of the pore volume representing gas-filled pores. In reality, the gas-phase pore volume would be a complex function of the rate of  $H_2$  generation and the hydrogeological-mechanical conditions in the bentonite and host rock. However, such detailed calculations are beyond the scope of the SCM, requiring the simplified treatment that has been adopted. In addition, because the gas transport properties of the host rock are not known (particularly the gas entry pressure) the same mechanism (and same pressure thresholds) are assumed to apply to the sedimentary host rock as well. This treatment could be modified once the gas transport properties of the host rock are known.

It is clear that none of the models briefly discussed above provides a complete simulation of all processes occurring in the repository. However, the SCM is, possibly, the most comprehensive in its treatment of corrosion, gas generation and transport, clay alteration, and the overall simulation of actual repository conditions.

## 5.5 FURTHER DEVELOPMENT AND IMPROVEMENTS TO THE MODEL

A number of areas of possible further development of the SCM can be identified based on the results of the simulations and the comparison with laboratory data and information from analog studies, as well as by comparison with other similar modelling efforts.

In terms of the treatment of the anaerobic corrosion process, the following improvements could be made:

- Incorporation of a thermodynamic speciation code to better predict the nature of the pore-water chemistry and the relative stabilities of a wider range of solid phases and clay minerals. In particular, it is important to establish (in conjunction with an experimental program) whether the pH at the container surface is alkaline. In addition, an improved treatment of the pore-water speciation would identify the conditions under which  $\text{Fe}_3\text{O}_4$  is the stable corrosion product (as currently predicted by the SCM) and when  $\text{FeCO}_3$  could be expected to form (as indicated by laboratory tests and observations from archaeological analog studies).
- If, based on the above studies, the interfacial pH is expected to increase to a value  $>\text{pH}$  8-9 then the expression for the dissolution rate of C-steel will need to be modified to account for the likelihood of passivation of the container surface. Currently, dissolution kinetics are based on data for C-steel in concentrated  $\text{Cl}^-$  solutions for which the surface is non-passive.
- Because of the slow saturation time expected for a DGR in sedimentary host rock, it is possible that the supply of  $\text{H}_2\text{O}$  could be rate limiting. The availability of water is implicitly accounted for through the use of threshold relative humidity values for the onset of corrosion, but the supply and consumption of  $\text{H}_2\text{O}$  is not explicitly accounted for in the model.

There are also a number of code-related improvements that could be made to the model, including:

- As the container corrodes the metal surface recedes effectively creating volume into which corrosion product can precipitate. Since the recession of the container surface is not currently taken into account, it is possible that the extent of  $\text{Fe}_3\text{O}_4$  precipitation in the bentonite (and the consequent reduction in porosity) is over-estimated.
- As knowledge of the gas transport mechanism(s) through the sedimentary rock becomes available, the treatment of gas transport should be improved. Currently, the mechanism for gas transport in compacted bentonite is applied to both the buffer and host rock. By analogy with the gas transport processes for Opalinus clay (Nagra 2004), the mechanism(s) is(are) likely to be different for the sedimentary rock.

Finally, although the SCM was always designed as a model to predict the anaerobic corrosion behaviour of C-steel, the mechanistic information required to assess the extent of corrosion during the aerobic phase is available and could be incorporated into an extended model. However, the mechanism of the transitional phase between aerobic and anaerobic conditions (which involves the transformation of Fe(III)-rich corrosion products to Fe(II) species) is currently incompletely understood and requires further study before it could be implemented in a revised model.

## 6. CONCLUSIONS

Preliminary simulations have been performed using the Steel Corrosion Model Version 1.0 (SCM V1.0) to predict the anaerobic corrosion behaviour of C-steel used fuel containers in a deep geologic repository in sedimentary host rock. The model also predicts the effect of corrosion products, namely Fe(II) and H<sub>2</sub>, on the properties of the bentonite barrier and the overall evolution of the repository environment.

The results of the preliminary simulations of the repository system can be summarised as follows:

- After full saturation of the bentonite, the corrosion rate decreases with time as a result of the formation of a protective surface film and the decrease in container surface temperature.
- The mean corrosion rate for the Base Case simulations is 1.0  $\mu\text{m}\cdot\text{a}^{-1}$ , resulting in a container lifetime of 19,500 a (based on a 2-cm corrosion allowance).
- The maximum corrosion rate is of the order 5-10  $\mu\text{m}\cdot\text{a}^{-1}$ , depending upon the modelling assumptions.
- The principal solid corrosion product is Fe<sub>3</sub>O<sub>4</sub>, with only small amounts of FeCO<sub>3</sub> and Fe(OH)<sub>2</sub> predicted to form.
- Anodic dissolution of C-steel is supported primarily by the cathodic reduction of H<sub>2</sub>O, with the reduction of HCO<sub>3</sub><sup>-</sup> accounting for only 0.03% of the total amount of corrosion.
- The corrosion potential is characteristic of corrosion under anaerobic conditions.
- The value of E<sub>CORR</sub> shifts to more-positive potentials with time as a result of the decrease in temperature.
- The principal effect of the precipitated corrosion product on the corrosion behaviour is to block the interfacial dissolution reactions.
- A Fe<sub>3</sub>O<sub>4</sub> "front" extends some tens of cm into the bentonite buffer after a period of several hundred thousand years, reducing the porosity in the near field.
- Ferrous ions are sorbed on the bentonite and promote alteration of montmorillonite for a distance of some tens of cm from the canister surface after a period of several hundred thousand years. However, the maximum extent of clay alteration is less than 13% of the original smectite content.
- Hydrogen gas is generated and periodically released from the repository.

The predicted corrosion rate is in good agreement with values measured experimentally and those inferred from the study of archaeological artifacts. Furthermore, the predicted precipitation of corrosion product in the adjacent clay layer is consistent with observations from the study of archaeological artifacts exposed to soils for long periods of time.

The SCM combines a detailed electrochemical treatment of the container corrosion process with the capability to predict the long-term evolution of the repository environment and the impacts of corrosion products on the other barriers in the system. In this regard, the SCM exhibits a number of unique features compared with other similar models in the literature.

## REFERENCES

- Andra. 2005. Dossier 2005 Argile. Andra (Châtenay-Malabry, France, December 2005).
- Baum, A. and K. Evans. 2005. Modelling concentrated solution transport and accumulation in steam generator tube support plate crevices. *In* Proc. 12<sup>th</sup> Int. Conf. Environmental Degradation Materials in Nuclear Power Systems, T.R. Allen, P.J. King, and L. Nelson (eds.), The Minerals, Metals & Materials Society (Warrendale, PA), pp. 1155-1162.
- Bignold, G.J., R. Garnsey, and G.M.W. Mann. 1972. High temperature aqueous corrosion of iron. Development of theories of equilibrium solution phase transport through a porous oxide. *Corros. Sci.* 12, 325-332.
- Bildstein, O., L. Trotignon, M. Perronnet, and M. Jullien. 2006. Modelling iron-clay interactions in deep geological disposal conditions. *Phys. Chem. Earth* 31, 618-625.
- Cole, I.S., W.D. Ganther, J.D. Sinclair, D. Lau, and D.A. Paterson. 2004. A study of the wetting of metal surfaces in order to understand the processes controlling atmospheric corrosion. *J. Electrochem. Soc.* 151, B627-B635.
- Collin, M. and A. Rasmuson. 1988. A comparison of gas diffusivity models for unsaturated porous media. *Soil Sci. Soc. Am. J.* 52, 1559-1565.
- Crossland, I. 2005. Long term corrosion of iron and copper. *In* ICEM'05: 10<sup>th</sup> International Conference on Environmental Remediation and Radioactive Waste Management, September 4-8, 2005 (American Society of Mechanical Engineers, New York, NY), paper ICEM05-1272.
- de Combarieu, G., P. Barboux, and Y. Minet. 2007. Iron corrosion in Callovo-Oxfordian argillite: from experiments to thermodynamic/kinetic modelling. *Phys. Chem. Earth* 32, 346-358.
- Féron, D., D. Crusset, and J.-M. Gras. 2009. Corrosion issues in the French high-level nuclear waste program. *Corrosion* 65, 213-223.
- Graham, J., N.A. Chandler, D.A. Dixon, P.J. Roach, T. To, and A.W.L. Wan. 1997. The buffer/container experiment: results, synthesis, issues. Atomic Energy of Canada Limited Report, AECL-11746, COG-97-46-I.
- Harrington, J. F. and S.T. Horseman. 1999. Gas transport properties of clays and mudrocks. *In*: Muds And Mudstones: Physical And Fluid Flow Properties (eds A.C.Aplin, A.J. Fleet, and J.H.S. Macquaker). Geological Society of London, Special Publication No. 158, 107-124.
- Harrington, J.F. and S.T. Horseman. 2003. Gas migration in KBS-3 buffer bentonite. Swedish Nuclear Fuel and Waste Management Company Report, TR-03-02.
- Horseman, S. T., J.F. Harrington, and P. Sellin. 1999. Gas migration in clay barriers. *Engineering Geology*, Vol. 54, 139-149.

- JNC. 2000. H12: Project to establish the scientific and technical basis for HLW disposal in Japan. Japan Nuclear Cycle Development Institute, Supporting Report 2, Repository Design and Engineering Technology.
- Johnson, L.H. and F. King. 2008. The effect of the evolution of environmental conditions on the corrosion evolutionary path in a repository for spent fuel and high-level waste in Opalinus Clay. *J. Nucl. Mater.* 379, 9-15.
- Karnland, O., T. Sanden, L.-E. Johannesson, T.E. Eriksen, M. Jansson, S. Wold, K. Pedersen, M. Motamedi, and B. Rosborg. 2000. Long term test of buffer material. Final report on the pilot parcels. Swedish Nuclear Fuel and Waste Management Company Report, SKB TR 00-22.
- King, F. 2005. Evolution of environmental conditions in a deep geological repository in the sedimentary rock of the Michigan Basin, Ontario. Ontario Power Generation Nuclear Waste Management Division Report 06819-REP-01300-10102-R00.
- King, F. 2007. Overview of a carbon steel container corrosion model for a deep geological repository in sedimentary rock. Nuclear Waste Management Organization Technical Report No.: NWMO TR-2007-01.
- King, F. 2008. Corrosion of carbon steel under anaerobic conditions in a repository for SF and HLW in Opalinus Clay. Nagra Technical Report 08-12. Nagra, Wetingen, Switzerland.
- King, F. 2012. Gaseous hydrogen issues in nuclear waste disposal. In *Gaseous Hydrogen Embrittlement of Materials in Energy Technologies*, R.P. Gangloff and B.P. Somerday (eds.), Volume 1, Woodhead Publishing (Oxford, UK), chap. 4.
- King, F. and M. Kolar. 1999. Prediction of the effects of  $\alpha$ -radiolysis, precipitation and redox reactions with Fe and Fe(II) on the dissolution of  $UO_2$  using the mixed-potential model of fuel dissolution (MPM Version 1.1). Ontario Power Generation Nuclear Waste Management Division Report No: 06819-REP-01200-10014.
- King, F., and M. Kolar. 2000. The copper container corrosion model used in AECL's second case study. Ontario Power Generation Nuclear Waste Management Division Report No: 06819-REP-01200-10041-R00.
- King, F. and M. Kolar. 2001. Mixed-potential model simulations of the effects of porous film formation on the dissolution of used fuel (MPM Version 1.3). Ontario Power Generation Nuclear Waste Management Division Report No: 06819-REP-01300-10019.
- King, F. and M. Kolar. 2009. Theory manual for the Steel Corrosion Model version 1.0. Nuclear Waste Management Organization Technical Report No.: NWMO TR-2009-07.
- King, F. and C. Padovani. 2011. Review of the corrosion performance of selected canister materials for disposal of UK HLW and/or spent fuel. *Corros. Eng. Sci. Technol.* 46, 82-90.
- King, F., M. Kolar, and D.W. Shoesmith. 1996. Modelling the effects of porous and semi-permeable layers on corrosion processes. In *Proc. CORROSION/96, NACE International* (Houston, TX), paper no. 380.

- King, F., M. Kolar, and P. Maak. 2008. Reactive-transport model for the prediction of the uniform corrosion behaviour of copper used fuel containers. *J. Nucl. Mater.* 379, 133-141.
- Kreis, P. and J.P. Simpson. 1992. Hydrogen gas generation from the corrosion of iron in cementitious environments. . *In* Corrosion Problems Related to Nuclear Waste Disposal, European Federation of Corrosion Publication Number 7 (Institute of Materials, London), 57-72.
- Kursten, B., F. Druyts, D.D. Macdonald, N.R. Smart, R. Gens, L. Wang, E. Weetjens, and J. Govaerts. 2011. Review of corrosion studies of metallic barrier in geological disposal conditions with respect to Belgian Supercontainer concept. *Corros. Eng. Sci. Technol.* 46, 91-97.
- Langmuir, D. 1997. *Aqueous Environmental Geochemistry*. Prentice Hall (Upper Saddle River, NJ).
- Lu, C., J. Samper, B. Fritz, A. Clement, and L. Montenegro. 2011. Interactions of corrosion products and bentonite: an extended multicomponent reactive transport model. *Phys. Chem. Earth* 36, 1661-1668.
- Maak, P. 1999. The selection of a corrosion-barrier primary material for used-fuel disposal containers. Ontario Power Generation, Nuclear Waste Management Division Report 06819-REP-01200-10020-R00.
- Marty, N.C.M., B. Fritz, A. Clément, and N. Michau. 2010. Modelling the long term alteration of the engineered barrier in an underground radioactive waste repository. *Appl. Clay Sci.* 47, 82-90.
- Nagra. 2002. Project Opalinus Clay. Safety Report. Nagra Technical Report NTB 02-05.
- Nagra. 2004. Effects of post-disposal gas generation in a repository for spent fuel, high-level waste and long-lived intermediate level waste sited in Opalinus Clay. Nagra Technical Report NTB 04-06.
- Neff, D., P. Dillmann, L. Bellot-Gurlet, and G. Beranger. 2005. Corrosion of iron archaeological artefacts in soil: characterisation of the corrosion system. *Corros. Sci.* 47, 515-535.
- Neff, D., P. Dillmann, M. Descostes, and G. Beranger. 2006. Corrosion of iron archaeological artefacts in soil: estimation of the average corrosion rates involving analytical techniques and thermodynamic calculations. *Corros. Sci.* 48, 2947-2970.
- NWMO. 2005. Choosing a way forward. The future management of Canada's used nuclear fuel. Final study. Nuclear Waste Management Organization, Toronto, Ontario.
- NWMO. 2011. Fifth case study engineering data. Nuclear Waste Management Organization Data Clearance Form, File No. APM-01901-P.

- Palandri, J.L. and Y.K. Kharaka. 2004. A compilation of rate parameters of water-mineral interaction kinetics for application to geochemical modeling. U.S. Geological Survey Open File Report 2004-1068.
- Papillon, F., M. Jullien, and C. Bataillon. 2003. Carbon steel behaviour in compacted clay: two long term tests for corrosion prediction. *In* Prediction of Long Term Corrosion Behaviour in Nuclear Waste Systems. European Federation of Corrosion Publication No. 36 (Institute of Materials, Minerals and Mining, London), p. 439-454.
- Qin, Z., B. Demko, J. Noël, D. Shoesmith, F. King, R. Worthingham, and K. Keith. 2004. Localized dissolution of millscale-covered pipeline steel surfaces. *Corrosion* 60, 906-914.
- Russell, S.B. and G.R. Simmons. 2003. Engineered barrier system for a deep geological repository in Canada. *In* Proc. 10th Int. High-Level Radioactive Waste Management Conf., Las Vegas, NV, March 30-April 2, 2003 (American Nuclear Society, La Grange Park, IL), pp. 563-570.
- Saheb, M., D. Neff, Ph. Dillmann, H. Matthieson, and E. Foy. 2008. Long-term corrosion behaviour of low-carbon steel in anoxic environment: characterisation of archaeological artefacts. *J. Nucl. Mater.* 379, 118-123.
- Samer, J., C. Lu, and L. Montenegro. 2008. Reactive transport model of interactions of corrosion products and bentonite. *Phys. Chem. Earth* 33, S306-S316.
- Shoesmith, D.W., M. Kolar, and F. King. 2003. A mixed-potential model to predict fuel (uranium dioxide) corrosion within a failed nuclear waste container. *Corrosion*, 59, 802-816.
- Shreir, L.L., R.A. Jarman, and G.T. Burstein. 1993. *Corrosion. Volume 1 Metal/Environment Reactions*, 3<sup>rd</sup> Edition. Butterworth-Heinemann. Oxford, UK.
- Smart, N.R., D.J. Blackwood, and L.O. Werme. 2001: The anaerobic corrosion of carbon steel and cast iron in artificial groundwaters. SKB Technical Report TR-01-22.
- Stroes-Gascoyne, S., J. Betteridge, and F. King. 2000. Characterization of corrosion products on carbon steel: porosity measurements and surface examinations. Ontario Power Generation Nuclear Waste Management Division Report No: 06819-REP-01200-10017.
- Taniguchi, N., M. Kawasaki, S. Kawakami, and M. Kubota. 2004. Corrosion behaviour of carbon steel in contact with bentonite under anaerobic condition. *In* Prediction of Long Term Corrosion in Nuclear Waste Systems. Proc. 2<sup>nd</sup> Int. Workshop, Nice, September 2004 (European Federation of Corrosion and Andra), p. 24-34.
- Torres, E., M.J. Turrero, and P.L. Martin. 2007. Geochemical processes at the carbon steel/bentonite interface in repository conditions. *Mater. Res. Soc. Symp. Proc.* 985, Materials Research Society (Warrendale, PA), paper 0985-NN11-14.
- Uhle, J.L. 1997. Boiling heat transfer characteristics of steam generator U-bend fouling deposits. Ph.D. thesis, Massachusetts Institute of Technology.

- Wersin, P. and M. Snellman. 2008. Impact of iron on the performance of clay barriers in waste disposal systems. Report on the status of research and development. Posiva Working Report 2008-07.
- Wersin, P., M. Birgersson, S. Olsson, O. Karnland, and M. Snellman. 2007. Impact of corrosion-derived iron on the bentonite buffer within the KBS-3H disposal concept – the Olkiluoto site as case study. Posiva Report, Posiva 2007-11.
- Xia, X., K. Idemitsu, T. Arima, Y. Inagaki, T. Ishidera, S. Kurosawa, K. Ijima, and H. Sato. 2005. Corrosion of carbon steel in compacted bentonite and its effect on neptunium diffusion under reducing condition. *Appl. Clay Sci.* 28, 89-100.
- Yoshikawa, H., E. Gunji, and M. Tokuda. 2008. Long term stability of iron for more than 1500 years indicated by archaeological samples from the Yamato 6<sup>th</sup> tumulus. *J. Nucl. Mater.* 379, 112-117.



**APPENDIX A: INPUT DATA FOR STEEL CORROSION MODEL VERSION 1.0**

**CONTENTS**

	<b><u>Page</u></b>
<b>A.1 CONTROL PARAMETERS .....</b>	<b>69</b>
<b>A.2 MODEL PARAMETERS .....</b>	<b>71</b>



## A.1 CONTROL PARAMETERS<sup>8</sup>

### **monitor = 1**

The amount of diagnostic on-screen output during the transient calculation:

- 1 - Only the value of t is printed at all "pr\_Other" output times.
- 0 - The values of t and cDiffM are printed at regular "pr\_Other" output times.
- 1 - Values of t, cDiffM=(MAX over j and e of |c[j][e]-c\_o[j][e]|)/cAVmax, # of attempts, and total # of runband Newton-Raphson (NR) iterations in all attempts are printed after EACH time step.
- 2 - During EACH time step a line with iter #, (fresidT), fresidM, node and equ # where fresidM occurs, (cresidT), cresidM, and the corresponding node and equ #, are printed after each iteration. Then a line which starts with t, cDiffM, tStep, Scale = next\_tStep/tStep ratio.  
Also some details about repeated attempts are given, and output to the two output files is marked by printing <outOTH> and <out>.
- 3 - In addition to 2, one more line is inserted on where cDiffM occurs, and giving cAVmax = (MAX of |c\_o| and |c| over all nodes j and equations e).

In the last 4 cases the (last) line continues with the cumulative #s of time steps, attempts (calls to runband), and NR iterations (incl. those in the unsuccessful attempts).

In the last 3 cases it ends with the value of cDiffM extrapolated to the time interval between two consecutive profiles-output times (gives an estimate of max relative change between the consecutive outputted c-profiles: e.g., 0.01 ~ change in the 3rd significant digit, etc.)

### **CmntC = #**

Character to mark the beginning of comment (i.e., not to be plotted) lines in the output files. May start a valid input line in input files.

### **steady = 0**

- 0 - The main purpose of this program: transient solution of coupled reaction-diffusion equations in one spatial variable; all control parameters listed below are used.
- 1 - Only the steady state is calculated using the same evalf() function as for transient solution, provided that it consistently uses the global variable 'tStepInv' to calculate the contribution of discretized time derivatives of concentrations to B[k][k] (tStepInv = 1/tStep); only monitor (1=2) and CmntC are used.
- 2 - Calculate steady state and then use it as the initial state for the transient calculation (e.g., to check its stability).

### **Tau = 0**

"Implicitness" of the differencing scheme (in time; 0 <= Tau <= 1):

- 0 fully implicit
- 0.5 Crank-Nicholson
- 1 explicit

Preferably use Tau = 0.5; if there are problems, try Tau < 0.5; in some cases, Tau = 0 may be the best.

### **NIG = 0.5**

New Initial Guess extrapolation factor (-0.5<=NIG<=1) for the next time step:

---

<sup>8</sup> For each parameter (in **bold font**), the first line of the entry defines the name of the parameter and, following the "=" sign, its default value. This is followed by a definition of the parameter and, where appropriate, a discussion of the basis for the default value.

$c\_New\_Initial\_Guess = c + NIG * scale * (c - c\_previous)$ ; where  $scale = (t\_new - t)/(t - t\_previous)$ , and  $t$  and  $c$  are the current time and concentration

**nIter = 10**

Desired number of NR iterations in runband() in each attempt

**tStart = 0 sec**

Initial time (start of integration)

**tEnd = 3.155692600000e+13 sec**

Final time (end of integration)

**tStepInit = 0.01 sec**

Magnitude of the initial time step tStep

**tStepMin = 0 sec**

If > 0: the smallest allowed magnitude of the time step tStep;

If = 0: no minimal time step set;

If < 0:  $|tStep| \geq -tStepMin * tt$ , where  $tt$  is the (always positive) time elapsed from the beginning of a run

**tStepMax = -0.1 sec**

If > 0: the largest allowed magnitude of the time step tStep;

If = 0:  $|tStep| \leq 0.1 * |tEnd - tStart|$ ;

If < 0:  $|tStep| \leq tStepInit - tStepMax * tt$ , where  $tt$  is the (always positive) time elapsed from the beginning of a run

**tOutInit = 3.600000000000e+03 sec**

Initial time (tOut) for c profiles output

**tOutMulF = 1.4**

Rate of increase of the time interval between subsequent c profiles outputs:

$Next\_tOut = tOut + (tOut - previous\_tOut) * tOutMulF$

**nOutOTH = -20**

pr\_Other() is called at  $|nOutOTH| - 1$  regularly spaced time instants between 2 consecutive tOut (can be used for additional output).

If  $nOutOTH < 0$ , pr\_Other calls need not be exactly equidistant in time.

**sepProf = 1**

0 - Concentration profiles for all output times will be placed into a single output file.

1 - Profiles for each time will be placed into a separate file.

-1 - No profiles file created. In addition, no diagnostic file created.

**strict = 0**

strict < 0: cDiffMxf(t) is not used at all to calculate next tStep which is determined only by nIter.

strict = 0: cDiffM does usually not exceed cDiffMxf(t) too much.

strict = 1:  $cDiffM \leq cDiffMxf(t)$  is strictly enforced.

Here cDiffM is the maximum magnitude of the change in all  $c[i]/cAVmax$  over the whole tStep (while cResidM is the same value over a single NR iteration only).

cDifMxf(t) is determined by input parameters cDifMxMode, cDifMxInit, and cDifMxEnd. Often strict<0 is good enough, and fast.

**cDifMxMode = 1**

Mode of interpolating between cDifMxInit and cDifMxEnd in cDifMxf(t):

0 - Max allowed change in c is constant and equal to cDifMxInit

1 - Linear interpolation

2 - Log-log linear:  $\ln(\text{cDifMxf}) = \text{linear function of } \ln(|t|)$

3 - Piecewise linear: In this case cDifMxMode = number of all time instants between each consecutive two of which a linear interpolation of cDifMxf will be done. These include the initial and final values, cDifMxInit and cDifMxEnd. The remaining cDifMxMode-2 inner points are entered as values of input parameters cDifMxP1, cDifMxP2, ..., cDifMxP{cDifMxMode-2}. Their values are the comma-separated (no spaces allowed around the comma) pairs of time and the corresponding value of cDifMxf. Example:

cDifMxInit = 1e-5

cDifMxP3 = 1e5,0.1

cDifMxP1 = 10.,1e-4

cDifMxEnd = 1.

cDifMxMode = 5

cDifMxP2 = 1e3,0.01

(Order of input lines does not matter, but times corresponding to cDifMxP{i} must increase with i if tEnd>tStart, and decrease with i if tEnd<tStart.)

**cDifMxInit = 1**

Value of cDifMxf at  $t = tStart + \text{sign}(tEnd - tStart) * tStepInit$

**cDifMxEnd = 0.001**

Value of cDifMxf at  $t = tEnd$  (needed only for cDifMxMode>0)

**init\_from\_file =**

Name of file containing the initial profiles; if non-null, the user supplied function read\_profiles() will be invoked just after Initialize(), and initial profiles set in Initialize() will be overwritten by those read in read\_profiles(). Can be used to continue an interrupted calculation (possibly after changing some parameters).

**A.2 MODEL PARAMETERS**

**tAnaerobic = 1577846300 s**

Time to the start of the anaerobic phase. A time delay is required in the code to account for the cooling of the containers during the initial aerobic and transition phases. A default period of 50 years is used. Prior to this time, the code only predicts the temporal and spatial distribution of the temperature and  $\text{Cl}^-$  and  $\text{HCO}_3^-$  concentrations. At later times, corrosion reactions and other processes are also modelled.

**Nmedia = 5**

Number of layers present in the model. A maximum of 11 layers can be specified in V1.0, allowing sub-division of various layers to provide greater spatial resolution of the time-dependent degree of saturation.

Five layers are specified for the default version of the SCM, three layers representing the buffer material, one layer representing the excavation disturbed and damaged zones, (EDZ), and one layer representing the host rock.

**par\_tUnit = Y**

Y M or D - units of time in the par`Output` file.

**EPS\_ZERO = 1e-25**

If  $c_5$  is  $\leq$  EPS\_ZERO, it is assumed to be 0 for the purpose of the corrosion potential calculation. The reduction of  $\text{HCO}_3^-$  (species 5, concentration  $c_5$ ) is one of the cathodic reactions considered in the model and a criterion is required for deciding when this reaction is no longer significant.

**EPS\_POT = 2e-16**

Terminating tolerance for the corrosion potential calculation.

**RefineInterfaces = 1**

If equal to 0: nothing is done

If > 1: grid is refined a lot down to dxInt around all interfaces

If = 1: grid is made finer (4 points added) around all interfaces

If < 0: grid is made coarser (2 points removed) around all interfaces

Permits optimization of the spatial grid to either increase accuracy or decrease execution time.

**dxInt = 1e-05 dm**

Refined grid interval used only with RefineInterfaces>1.

**IEndFine = 10 dm**

The RHS part of the thickness of the last medium:

If > 0: grid is refined in (xRHS-IEndFine,xRHS) so that the length of the last interval equals dxLast.

Ensures that the model comprises an integral number of intervals.

**dxLast = 5e-07 dm**

Refined grid interval at xRHS = L1+L2+...+L\_Nmedia.

**NMlayer1 = buffer\_1**

Name of medium in layer 1. The UFC is surrounded by a combination of highly compacted bentonite (HCB) (that serves as a pedestal for the container) and bentonite pellets that fills the remaining space in the disposal tunnel. For the V1.0 simulations, volume-averaged properties are used for the buffer which are assumed to be uniform throughout the tunnel. The compacted bentonite buffer is divided into three layers to provide greater spatial resolution of the time-dependent degree of saturation.

**L1 = 4.0 dm**

Thickness of medium 1.

The total thickness of the bentonite buffer is defined by the buffer volume: container surface area ratio for the specific repository design being considered. For the default geometry for SCM V1.0, it is assumed that the containers (1.195 m diameter by 3.88 m in length) are disposed of

horizontally in (circular cross section) tunnels with a diameter of 2.5 m and a container centre-centre spacing of 8.0 m. These dimensions produce a buffer volume:container surface area ratio of 2.40 m, which is arbitrarily divided into three sub-layers. The thickness of the buffer layer in contact with the container is smaller than that for the outer two layers (which are taken to be of equal thickness) as moisture content profiles and concentration gradients are steeper closer to the container. As a consequence, the spacing of the spatial grid is smaller for the first layer of buffer.

**dx1 = 1e-07 dm**

Grid interval at x=0.

**l1 = 0 dm**

Initial part of the thickness of medium 1:

If l1>0: grid is constructed separately in (0,l1) and (l1,L1) using dx1a

If l1<=0: dx1a is disregarded; subdivision made automatically by the code

**dx1a = 0.018 dm**

Grid interval at x=l1; optional - see l1

**dx2 = 0.11 dm**

Grid interval at x=L1

**eps1E = 0.24**

Maximum effective porosity of medium 1. The total porosity of the compacted bentonite is determined by the dry density and the specific gravity of the solids (Craig 1987). A combination of HCB (to act as a pedestal for the container) and pelletized bentonite (itself a mixture of dry bentonite pellets and bentonite powder) is assumed to be used for filling the disposal tunnels following container emplacement. These materials will have different initial moisture contents and densities. However, for the purposes of the SCM V1.0, it is assumed that the initial moisture and bentonite density have homogenized prior to the onset of anaerobic conditions.

The total porosity is divided equally between the effective porosity for mass transport and the storage porosity (see below). It is further assumed that the entire pore space is accessible (i.e., the non-accessible porosity is zero).

Based on data from Garisto et al. (2004), the porosity of the HCB is 0.41 and that of the bentonite pellets 0.49. The total volume of bentonite per container (volume of 8-m-long by 2.5-m diameter tunnel minus the volume of a 3.88-m-long by 1.195-m-diameter container) is 34.918 m<sup>3</sup>. Based on the cross-sectional diagram in Figure 4, the HCB pedestal is taken to be 0.6525 m high by 0.94 m wide by 3.88 m long, for a total volume of 2.380 m<sup>3</sup>. The volume averaged (total) porosity of the bentonite  $\epsilon_{ave}$  is, therefore, 0.4845  $\left( \epsilon_{ave} = \frac{32.538 \times 0.49 + 2.380 \times 0.41}{34.918} \right)$ .

**eps1S = 0.24**

Maximum storage porosity of medium 1. That fraction of the accessible porosity comprising dead-end pores and similar pore space that does not contribute to mass transport. For SCM V1.0 assumed to comprise 50% of the total porosity.

**eps1N = 0**

Porosity inaccessible to diffusant in medium 1. For SCM V1.0, all of the porosity is assumed to be accessible.

**rho1 = 2.7 kg/dm<sup>3</sup>**

Particle density of medium 1. This is the particle density (i.e., the density of the solids), not the dry or bulk density of the material.

**c10max1 = 0.4 mol/kg**

Maximum value of c10 in medium 1. Dissolved Fe(II) is assumed to be adsorbed by the bentonite clay (adsorbed Fe(II), species 10). The maximum concentration of adsorbed Fe(II) is determined by the cation-exchange capacity of the bentonite, assumed to be 80 meq/100g, a value typical of that for montmorillonites.

**tau1 = 0.05**

Tortuosity factor of medium 1. As specified for the reference highly compacted bentonite for the Third Case Study (Gierszewski et al. 2004).

**c51 = 0.001 mol/dm<sup>3</sup>**

Initial concentration of c5 in medium 1. Initial concentration of bicarbonate (species 5) in the bentonite buffer. The concentration of HCO<sub>3</sub><sup>-</sup> in the bentonite is determined by the presence of soluble carbonate mineral impurities in the clay, subject to solubility limits.

The primary source of HCO<sub>3</sub><sup>-</sup> in bentonite pore water is the dissolution of calcite (CaCO<sub>3</sub>). The calcite content of Avonlea bentonite is reported to be <5 wt.% (Oscarson and Dixon 1989). Posiva (2006) give the combined calcite plus siderite content of MX-80 bentonite as 0-1 wt.%. For the current purposes, therefore, it is assumed that the calcite content of the bentonite to be used for the HCB and pellets is 2 wt.%. If all of this calcite dissolved in the water initially present, then the concentration of HCO<sub>3</sub><sup>-</sup> would be given by:

$$[HCO_3^-] = \frac{[CaCO_3] \times \rho_d^{ave}}{\varepsilon_{ave} \times S_{ave}^{init} \times M_W} \quad (A-1)$$

where [CaCO<sub>3</sub>] is the concentration of calcite in the bentonite (2 wt.% or 20 kg·Mg<sup>-1</sup>), ρ<sub>d</sub><sup>ave</sup> is the average dry density, S<sub>ave</sub><sup>init</sup> is the average initial moisture content, and M<sub>W</sub> is the molecular mass of CaCO<sub>3</sub>. The values of ρ<sub>d</sub><sup>ave</sup> and S<sub>ave</sub><sup>init</sup> are given by:

$$\rho_d^{ave} = \frac{32.538 \times 1410 + 2.380 \times 1610}{34.918} = 1424 \text{ kg} \cdot \text{m}^{-3} \quad (A-2)$$

and

$$S_{ave}^{init} = \frac{32.538 \times 0.06 + 2.380 \times 0.65}{34.918} = 0.1002 \quad (A-3)$$

respectively, where the dry densities and the initial degrees of saturation of the HCB and bentonite pellets are 1610 kg·m<sup>-3</sup> and 1410 kg·m<sup>-3</sup> and 65% and 6%, respectively (G. Kwong, private communication (2010)). The molecular mass of CaCO<sub>3</sub> is 100.0869 g·mol<sup>-1</sup>.

The maximum concentration of HCO<sub>3</sub><sup>-</sup> based on the calcite inventory is, therefore,

$$[HCO_3^-] = \frac{[CaCO_3] \times \rho_d^{ave}}{\varepsilon_{ave} \times S_{ave}^{init} \times M_W} = \frac{20 \times 1.4236}{0.4845 \times 0.1002 \times 100.0869} = 5.86 \text{ mol} \cdot \text{dm}^{-3} \quad (A-4)$$

This concentration is clearly greater than the solubility of calcite (see notes for c5satroom below) and so the initial value for c5 is set equal to the solubility limit.

**c61 = 0.015 mol/dm<sup>3</sup>**

Initial concentration of chloride (species 6) in the bentonite buffer (medium 1). The initial concentration of Cl<sup>-</sup> in the bentonite pore water is determined by the amount of soluble halite present in the bentonite and the initial degree of saturation (on the assumption that potable water is used for the initial wetting of the bentonite).

Oscarson and Dixon (1989) measured the salinity of water contacted with Avonlea bentonite at various solution/clay (s/c) ratios. They reported the individual ionic compositions and ionic strength (Table 6, Oscarson and Dixon (1989)) and found that the ionic strength I increased with decreasing s/c ( $I = 0.319 - 0.073(s/c) \text{ mol}\cdot\text{dm}^{-3}$ , Figure 7). From the data in Table 6 of Oscarson and Dixon (1989), the ratio of the dissolved [Cl<sup>-</sup>] to the ionic strength increases with decreasing s/c ( $[Cl^-]/I = 0.0490-0.00164(s/c)$ ).

Based on these relationships and the average s/c ratio for the repository ( $(S_{ave}^{init} \epsilon_{ave})/\rho_d^{ave}$ ), the initial [Cl<sup>-</sup>] is 0.015 mol·dm<sup>-3</sup>.

**cCA1 = 0.28 mol/dm<sup>3</sup>**

Initial concentration of calcium carbonate (species 12) in the bentonite (medium 1). The initial concentration of CaCO<sub>3</sub> in the bentonite is determined by the mineral composition of the bentonite. The amount of CaCO<sub>3</sub> is tracked in the model because it is likely to be consumed during the anaerobic phase due to the precipitation of FeCO<sub>3</sub> corrosion products.

Based on the assumed calcite content of 2 wt.%, the initial calcite concentration is given by

$$cCA1 = \frac{[CaCO_3] \times \rho_d^{ave}}{M_W} = \frac{20 \times 1.4236}{100.0869} = 0.28 \text{ mol} \cdot \text{dm}^{-3} \quad (\text{A-5})$$

**S1\_in = S\_Bu\_1**

Name of file with degree of saturation of medium 1 as function of time (a). In the absence of more-detailed thermal-hydrogeological modelling using site-specific data, the time-dependent saturation of the various layers in the model is based on assumptions regarding the time to complete saturation and expert judgement regarding the initial re-distribution of the initial moisture content. See discussion under Section 2.2.2.5 of main text.

**K1\_in = K\_Bu**

Name of file with thermal conductivity (W/dm/K) of medium 1 as function of S. Garisto et al. (2004) provide values for the as-placed thermal conductivity for both the highly compacted bentonite (1.00 W m<sup>-1</sup> K<sup>-1</sup> for a dry density of 1.610 Mg·m<sup>-3</sup> at 65% saturation) and buffer pellets (0.40 W m<sup>-1</sup> K<sup>-1</sup> for a dry density of 1.410 Mg·m<sup>-3</sup> at 6% saturation). These values are similar to those for the inner buffer defined for the Third Case Study by Gierszewski et al. (2004) and shown in Figure A-1.

The saturation-dependence given in Figure A-1 is used for the current simulations.

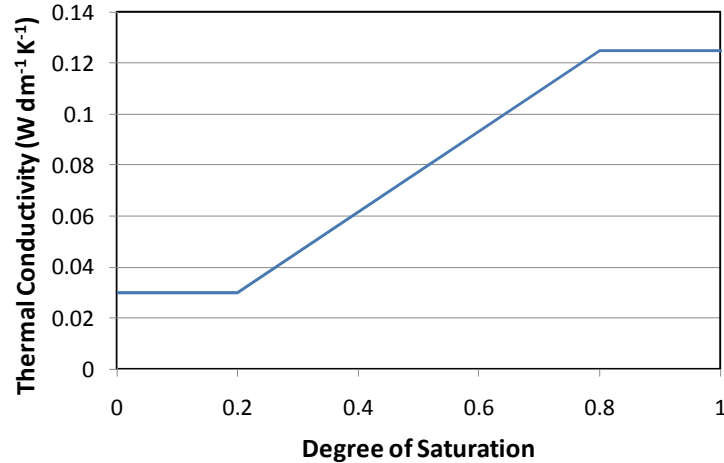


**Figure A-1: Dependence of the Thermal Conductivity of Bentonite on the Degree of Saturation as Specified for the Third Case Study (Gierszewski et al. 2004)**

**Cp1 = 845 J/kg/K**

Particle specific heat of medium 1. Note, the heat capacity is defined in the model as that of the solid and, hence, is not saturation-dependent. Value for rock defined in Table 6.2 of Garisto et al. (2004) taken as representative of dry clay.

**NMlayer2 = buffer\_2**

Name of medium in layer 2.

**L2 = 10 dm**

Thickness of medium 2. See discussion for L1.

**dx3 = 0.28 dm**

Grid interval at  $x=L1+L2$ .

**eps2E = 0.24**

Maximum effective porosity of medium 2. See discussion above for eps1E.

**eps2S = 0.24**

Maximum storage porosity of medium 2. See discussion above for eps1S.

**eps2N = 0**

Porosity inaccessible to diffusant in medium 2. For SCM V1.0, all of the porosity is assumed to be accessible.

**rho2 = 2.7 kg/dm<sup>3</sup>**

Particle density of medium 2. This is the particle density (i.e., the density of the solids), not the dry or bulk density of the material.

**c10max2 = 0.4 mol/kg**

Maximum value of c10 in medium 2. See discussion above for C10max1.

**tau2 = 0.05**

Tortuosity factor of medium 2. See discussion above for tau1.

**c52 = 0.001 mol/dm<sup>3</sup>**

Initial concentration of c5 (HCO<sub>3</sub><sup>-</sup>) in medium 2. See discussion above for c51.

**c62 = 0.015 mol/dm<sup>3</sup>**

Initial concentration of c6 (Cl<sup>-</sup>) in medium 2. See discussion above for c61.

**cCA2 = 0.28 mol/dm<sup>3</sup>**

Initial concentration of c12 (calcium carbonate) in medium 2. See discussion above for cCA1.

**S2\_in = S\_Bu\_2**

Name of file with degree of saturation of medium 2 as function of time (a). In the absence of more-detailed thermal-hydrogeological modelling using site-specific data, the time-dependent saturation of the various layers in the model is based on assumptions regarding the time to complete saturation and expert judgement regarding the initial re-distribution of the initial moisture content. See discussion under Section 2.2.2.5 of main text.

**K2\_in = K\_Bu**

Name of file with thermal conductivity (W/dm/K) of medium 2 as function of S. See discussion above under K1\_in.

**Cp2 = 845 J/kg/K**

Particle specific heat of medium 2. See discussion above under Cp1.

**NMlayer3 = buffer\_3**

Name of medium in layer 3

**L3 = 10 dm**

Thickness of medium 3. See discussion for L1.

**dx4 = 0.44 dm**

Grid interval at x=L1+L2+L3

**eps3E = 0.24**

Maximum effective porosity of medium 3. See discussion above for eps1E.

**eps3S = 0.24**

Maximum storage porosity of medium 3. See discussion above for eps1S.

**eps3N = 0**

Porosity inaccessible to diffusant in medium 3. For SCM V1.0, all of the porosity is assumed to be accessible.

**rho3 = 2.7 kg/dm<sup>3</sup>**

Particle density of medium 3. This is the particle density (i.e., the density of the solids), not the dry or bulk density of the material.

**c10max3 = 0.4 mol/kg**

Maximum value of c10 (adsorbed Fe(II)) in medium 3. See discussion above for C10max1.

**tau3 = 0.05**

Tortuosity factor of medium 3. See discussion above for tau1.

**c53 = 0.001 mol/dm<sup>3</sup>**

Initial concentration of c5 (HCO<sub>3</sub><sup>-</sup>) in medium 3. See discussion above for c51.

**c63 = 0.015 mol/dm<sup>3</sup>**

Initial concentration of c6 (Cl<sup>-</sup>) in medium 3. See discussion above for c61.

**cCA3 = 0.28 mol/dm<sup>3</sup>**

Initial concentration of c12 (calcium carbonate) in medium 3. See discussion above for cCA1.

**S3\_in = S\_Bu\_3**

Name of file with degree of saturation of medium 3 as function of time (a). In the absence of more-detailed thermal-hydrogeological modelling using site-specific data, the time-dependent saturation of the various layers in the model is based on assumptions regarding the time to complete saturation and expert judgement regarding the initial re-distribution of the initial moisture content. See discussion under Section 2.2.2.5 of main text.

**K3\_in = K\_Bu**

Name of file with thermal conductivity (W/dm/K) of medium 3 as function of S. See discussion above under K1\_in.

**Cp3 = 845 J/kg/K**

Particle specific heat of medium 3. See discussion above under Cp1.

**NMlayer4 = EDZ**

Name of medium in layer 4. For SCM V1.0, the layers comprise three layers of compacted bentonite, and excavation damaged zone (layer 4), and a layer of intact rock.

**L4 = 20 dm**

Thickness of medium 4. Defined as the maximum extent of fracturing of Opalinus Clay around tunnel (Nagra 2002). This represents an EDZ thickness equivalent to 1.6 times the diameter, slightly greater than the 1.0 times diameter for the sum of the inner and outer EDZ assumed for the LILW DGR project (Section 5.2, Walke et al. 2009).

**dx5 = 0.75 dm**

Grid interval at x=L1+L2+L3+L4.

**eps4E = 0.11**

Maximum effective porosity of medium 4. Default rock-type defined as shale, with limestone as the alternate. Porosity of EDZ defined as twice that of the host rock (an assumption consistent with that made by Walke et al. 2009), divided equally between effective mass-transport porosity and storage porosity. Porosity of host rock of 0.11 (shale) and 0.02 (limestone) (G. Kwong, private communication 2010).

**eps4S = 0.11**

Maximum storage porosity of medium 4. See discussion above under eps4E.

**eps4N = 0**

Porosity inaccessible to diffusant in medium 4. All EDZ porosity assumed to be accessible.

**rho4 = 2.6 kg/dm<sup>3</sup>**

Particle density of medium 4 (shale) (G. Kwong, private communication 2010).

**c10max4 = 0.2 mol/kg**

Maximum value of c10 in medium 4. Walke et al. (2009) define adsorption coefficients ( $K_d$ ) for a range of media that could be present in a LILW DGR, including bentonite, argillaceous material (e.g., shale), and limestone. The  $K_d$  values for limestone and argillaceous material are half of that for bentonite. On the assumption that the smaller  $K_d$  is a result of the lower content of adsorbents in the respective materials then it is reasonable to assume that the cation exchange capacity of shale and limestone are also half that of bentonite.

**tau4 = 0.05**

Tortuosity factor of medium 4. In the absence of other information, the tortuosity of the EDZ and host rock are assumed to be the same as that for compacted bentonite.

**c54 = 0.001 mol/dm<sup>3</sup>**

Initial concentration of c5 ( $\text{HCO}_3^-$ ) in medium 4. As discussed above for the compacted bentonite, the initial concentration of  $\text{HCO}_3^-$  in the EDZ pore water is determined by the solubility of  $\text{CaCO}_3$ . Similar assumptions are made regarding the pore-water pH and  $p_{\text{CO}_2}$  as for bentonite, resulting in the same calcite solubility for the EDZ and host rock.

**c64 = 4.75 mol/dm<sup>3</sup>**

Initial concentration of c6 ( $\text{Cl}^-$ ) in medium 4. The initial  $\text{Cl}^-$  concentration in the EDZ is assumed to be the same as that of the host rock pore fluid. Although evaporation of the EDZ pore fluid will occur during the operational phase, thus concentrating the solutes present, the host rock pore fluid is near saturation with  $\text{Cl}^-$  (depending on the nature of the predominant cation).

**cCA4 = 2.6 mol/dm<sup>3</sup>**

Initial concentration of c12 (calcite) in medium 4. The calcite contents of shale formations in Ontario vary significantly (e.g., from 0-30 wt.%, Table 6-7, Mazurek 2004). Based on the ranges provided by Mazurek, a characteristic calcite content of 10 wt.% is assumed, equivalent to a concentration of  $2.6 \text{ mol}\cdot\text{dm}^{-3}$  for a rock density of  $2.6 \text{ kg}\cdot\text{dm}^{-3}$ . The calcite content of limestone is much greater. If we assume a minimum calcite content of 50 wt.%, the corresponding calcite concentration is  $13 \text{ mol}\cdot\text{dm}^{-3}$ .

**S4\_in = S\_EDZ**

Name of file with degree of saturation of medium 4 as function of time (a). In the absence of more-detailed thermal-hydrogeological modelling using site-specific data, the time-dependent saturation of the various layers in the model is based on assumptions regarding the time to complete saturation and expert judgement regarding the initial re-distribution of the initial moisture content. See discussion under Section 2.2.2.5 of main text.

**K4\_in = K\_Rock**

Name of file with thermal conductivity ( $\text{W}\cdot\text{dm}/\text{K}$ ) of medium 4 as function of S. The degree of saturation of the EDZ and host rock are assumed to not change as much as that of the buffer material during the unsaturated phase. Therefore, the thermal conductivity of  $0.21 \text{ W}\cdot\text{dm}^{-1}\cdot\text{K}^{-1}$  provided by G. Kwong (private communication 2010) is assumed valid for all S. (For limestone, a value of  $0.23 \text{ W}\cdot\text{dm}^{-1}\cdot\text{K}^{-1}$  is assumed).

**Cp4 = 975 J/kg/K**

Particle specific heat of medium 4. Since the specific heat is defined for the solid matrix only, this parameter is independent of the degree of saturation. Values of  $975 \text{ J}\cdot\text{kg}^{-1}\cdot\text{K}^{-1}$  and  $830 \text{ J}\cdot\text{kg}^{-1}\cdot\text{K}^{-1}$  as specified by G. Kwong (private communication 2010).

**NMlayer5 = Rock**

Name of medium in layer 5.

**L5 = 300 dm**

Thickness of medium 5. Assumed thickness of sedimentary host rock layer between repository and adjacent hydraulically conducting formation. In the typical sequence of horizontally bedded sedimentary horizons found in Ontario, the thickness of each horizon varies from some tens of metres to several hundred metres. Here it assumed that a relatively thick horizon is selected for the repository, amounting to 60-70 m in total width. The adjacent horizons are assumed to exhibit a higher hydraulic conductivity, and are (conservatively) represented by a swept-away boundary condition for Fe species or a constant concentration boundary condition for ground water species.

**dx6 = 0.5 dm**

Grid interval at  $x=L1+L2+L3+L4+L5$

**eps5E = 0.055**

Maximum effective porosity of medium 5. Default rock-type defined as shale, with limestone as the alternate. Porosity of host rock of 0.11 (shale) and 0.02 (limestone) (G. Kwong, private communication 2010), divided equally between effective mass-transport porosity and storage porosity.

**eps5S = 0.055**

Maximum storage porosity of medium 5. Default rock-type defined as shale, with limestone as the alternate. Porosity of host rock of 0.11 (shale) and 0.02 (limestone) (G. Kwong, private communication 2010), divided equally between effective mass-transport porosity and storage porosity.

**eps5N = 0**

Porosity inaccessible to diffusant in medium 5. All of the porosity is assumed to be accessible.

**rho5 = 2.6 kg/dm<sup>3</sup>**

Particle density of medium 5 (shale host rock) (G. Kwong, private communication 2010).

**c10max5 = 0.2 mol/kg**

Maximum value of  $c_{10}$  in medium 5. Walke et al. (2009) define adsorption coefficients ( $K_d$ ) for a range of media that could be present in a LILW DGR, including bentonite, argillaceous material (e.g., shale), and limestone. The  $K_d$  values for limestone and argillaceous material are half of that for bentonite. On the assumption that the smaller  $K_d$  is a result of the lower content of adsorbents in the respective materials then it is reasonable to assume that the cation exchange capacity of shale and limestone are also half that of bentonite.

**tau5 = 0.05**

Tortuosity factor of medium 5. In the absence of other information, the tortuosity of the EDZ and host rock are assumed to be the same as that for compacted bentonite.

**c55 = 0.001 mol/dm<sup>3</sup>**

Initial concentration of c5 (HCO<sub>3</sub><sup>-</sup>) in medium 5. As discussed above for the compacted bentonite, the initial concentration of HCO<sub>3</sub><sup>-</sup> in the host rock pore water is determined by the solubility of CaCO<sub>3</sub>. Similar assumptions are made regarding the pore-water pH and p<sub>CO2</sub> as for bentonite, resulting in the same calcite solubility for the EDZ and host rock.

**c65 = 4.75 mol/dm<sup>3</sup>**

Initial concentration of c6 (Cl<sup>-</sup>) in medium 5. Host rock pore-water data provided by G. Kwong (private communication 2010).

**cCA5 = 2.6 mol/dm<sup>3</sup>**

Initial concentration of c12 (calcite) in medium 5. The calcite contents of shale formations in Ontario vary significantly (e.g., from 0-30 wt.%, Table 6-7, Mazurek 2004). Based on the ranges provided by Mazurek, a characteristic calcite content of 10 wt.% is assumed, equivalent to a concentration of for a rock density of 2.6 kg/dm<sup>3</sup>. If we assume a minimum calcite content of 50 wt.%, the corresponding calcite concentration is 13 mol/dm<sup>3</sup>.

**S5\_in = S\_Rock**

Name of file with degree of saturation of medium 5 as function of time (a). In the absence of more-detailed thermal-hydrogeological modelling using site-specific data, the time-dependent saturation of the various layers in the model is based on assumptions regarding the time to complete saturation and expert judgement regarding the initial re-distribution of the initial moisture content. See discussion under Section 2.2.2.5 of main text.

**K5\_in = K\_Rock**

Name of file with thermal conductivity (W/dm/K) of medium 5 as function of S. The degree of saturation of the EDZ and (shale) host rock are assumed to not change as much as that of the buffer material during the unsaturated phase. Therefore, the thermal conductivity of 0.21 W·dm<sup>-1</sup>·K<sup>-1</sup> provided by G. Kwong (private communication 2010) is assumed valid for all S. (For limestone, a value of 0.23 W·dm<sup>-1</sup>·K<sup>-1</sup> is assumed).

**Cp5 = 975 J/kg/K**

Particle specific heat of medium 5. Since the specific heat is defined for the solid matrix only, this parameter is independent of the degree of saturation. Values of 975 J·kg<sup>-1</sup>·K<sup>-1</sup> and 830 J·kg<sup>-1</sup>·K<sup>-1</sup> as specified by G. Kwong (private communication 2010).

**Troom = 298.15 K**

Room temperature at which all the room values below are given (25°C).

**D1room = 7.2e-08 dm<sup>2</sup>/s**

Diffusion coefficient for dissolved FeCl<sup>+</sup> (7.2 x 10<sup>-6</sup> cm<sup>2</sup>/s), taken to be the same as that for Fe<sup>2+</sup> (Anderko 2000).

**DeHD1 = 15000 J/mol**

Activation energy for D1. The activation energy for the diffusion coefficient of aqueous species is the same as that for the viscosity of water (CRC Press 1982).

**D2room = 7.2e-08 dm<sup>2</sup>/s**

Diffusion coefficient for dissolved Fe(CO<sub>3</sub>)<sub>2</sub><sup>2-</sup> (7.2 x 10<sup>-6</sup> cm<sup>2</sup>/s), taken to be the same as that for Fe<sup>2+</sup> (Anderko 2000).

**DeHD2 = 15000 J/mol**

Activation energy for D2. The activation energy for the diffusion coefficient of aqueous species is the same as that for the viscosity of water (CRC Press 1982).

**D3room = 7.2e-08 dm<sup>2</sup>/s**

Diffusion coefficient for dissolved FeOH<sup>+</sup> ( $7.2 \times 10^{-6}$  cm<sup>2</sup>/s), taken to be the same as that for Fe<sup>2+</sup> (Anderko 2000).

**DeHD3 = 15000 J/mol**

Activation energy for D3. The activation energy for the diffusion coefficient of aqueous species is the same as that for the viscosity of water (CRC Press 1982).

**D4room = 1.7e-07 dm<sup>2</sup>/s**

Diffusion coefficient for dissolved H<sub>2</sub> taken to be the same as that for dissolved O<sub>2</sub> (King et al. 2008).

**DeHD4 = 15000 J/mol**

Activation energy for D4. The activation energy for the diffusion coefficient of aqueous species is the same as that for the viscosity of water (CRC Press 1982).

**D5room = 1.1e-07 dm<sup>2</sup>/s**

Diffusion coefficient for dissolved HCO<sub>3</sub><sup>-</sup> (Anderko 2000).

**DeHD5 = 15000 J/mol**

Activation energy for D5. The activation energy for the diffusion coefficient of aqueous species is the same as that for the viscosity of water (CRC Press 1982).

**D6room = 2.0e-07 dm<sup>2</sup>/s**

Diffusion coefficient for dissolved Cl<sup>-</sup> (Anderko 2000).

**DeHD6 = 15000 J/mol**

Activation energy for D6. The activation energy for the diffusion coefficient of aqueous species is the same as that for the viscosity of water (CRC Press 1982).

**D13room = 0.0059 dm<sup>2</sup>/s**

Diffusion coefficient for gaseous H<sub>2</sub> taken to be equal to that for the diffusion of gaseous H<sub>2</sub> in air (0.59 cm<sup>2</sup>/s, CRC Press 1982).

**DeHD13 = -2060 J/mol**

Activation energy for D13 taken to be equal to the activation energy for the viscosity of air (CRC Press 1982).

**c1satRoom = 1.2e-05 mol/dm<sup>3</sup>**

Concentration of FeCl<sup>+</sup> in equilibrium with solid Fe(OH)<sub>2</sub>. Solubility of Fe(OH)<sub>2</sub> in 4.75 mol·dm<sup>-3</sup> Cl<sup>-</sup> solution at 25°C at pH 8 =  $1.2 \times 10^{-5}$  mol/kg based on data of Pan (1997). This Cl<sup>-</sup> concentration is equivalent to the groundwater concentration and implies equilibration of the pore solution with the groundwater. At this Cl<sup>-</sup> concentration, the dominant species is FeCl<sup>+</sup>. It is assumed that the pore-water pH is buffered at pH 8 by calcite. Molar concentration assumed equal to molality.

**DeH1sat = -47000 J/mol**

Activation energy for c1sat. Based on the predicted solubilities at 25°C and 100°C given by Pan (1997) and the assumption of Arrhenius behaviour in this temperature range. Ferrous hydroxide exhibits retrograde solubility.

**c2satRoom = 3.6e-06 mol/dm<sup>3</sup>**

Concentration of  $\text{Fe}(\text{CO}_3)_2^{2-}$  in equilibrium with solid  $\text{FeCO}_3$ . Based on the solubility product for  $\text{FeCO}_3$  of  $10^{-10.89}$  (Wersin et al. 2003) and assumption of equal concentrations of  $\text{Fe}(\text{II})$  and  $\text{CO}_3^{2-}$ .

**DeH2sat = 60000 J/mol**

Activation energy for c2sat (assumed value).

**c3satRoom = 3.8e-06 mol/dm<sup>3</sup>**

Concentration of  $\text{Fe}(\text{OH})^+$  in equilibrium with solid  $\text{Fe}(\text{OH})_2$ . Solubility of  $\text{Fe}(\text{OH})_2$  in 0.01 mol·dm<sup>-3</sup>  $\text{Cl}^-$  solution at 25°C at pH 8 =  $3.8 \times 10^{-6}$  mol/kg based on data of Pan (1997). At this  $\text{Cl}^-$  concentration, the dominant species is  $\text{Fe}^{2+}/\text{FeOH}^+$ . It is assumed that the pore-water pH is buffered at pH 8 by calcite. Molar concentration assumed equal to molality.

**DeH3sat = -69000 J/mol**

Activation energy for c3sat. Based on the predicted solubilities at 25°C and 100°C given by Pan (1997) and the assumption of Arrhenius behaviour in this temperature range. Ferrous hydroxide exhibits retrograde solubility.

**HinvRoom = 52.5 (unitless)**

The inverse Henry's law constant for  $\text{H}_2$  ( $\tilde{H}$ ) is defined as the ratio of gaseous to dissolved concentrations of  $\text{H}_2$  (expressed in the same units). The value for  $\tilde{H}$  is taken from Sander (1999).

**DeHHinv = -6650 J/mol**

The temperature dependence of the inverse Henry's law constant for  $\text{H}_2$  is taken from Sander (1999).

**c5satRoom = 1.0e-03 mol/dm<sup>3</sup>**

Concentration of dissolved  $\text{HCO}_3^-$  in equilibrium with calcite ( $\text{CaCO}_3$ ). Based on the solubility data given in Fig. 6.6 of Langmuir (1997) and the assumption of pH 8 pore water and a  $\text{CO}_2$  partial pressure of 0.001 atm (101 Pa).

**DeH5sat = -15600 J/mol**

Activation energy for c5sat. Because of the exothermic nature of the dissolution of  $\text{CaCO}_3$ , calcite exhibits a retrograde solubility. Activation energy estimated based on Fig. 6.8 of Langmuir (1997) and the assumption of Arrhenius behaviour between 0°C and 90°C.

**k1room = 1.0e-05 dm<sup>3</sup>/(mol.s)**

Homogeneous reaction rate constant for the reaction between  $\text{FeOH}^+$  and  $\text{Cl}^-$  to form precipitated  $\text{FeCl}^+$ . Kinetic data for this homogeneous reaction step are not available. The value for the second-order rate constant is defined such that the rate of conversion of  $\text{FeOH}^+$  to  $\text{FeCl}^+$  at a  $\text{Cl}^-$  concentration of 1 mol·dm<sup>-3</sup> is the same as that for the formation of  $\text{Fe}(\text{OH})_2$ .

**DeH1 = 60000 J/mol**

Activation energy for k1 (assumed value).

**k2room = 1.0e-05 1/s**

Homogeneous reaction rate constant for the reaction between  $\text{FeOH}^+$  and  $\text{OH}^-$  to form precipitated  $\text{Fe}(\text{OH})_2$ . Kinetic data for this homogeneous reaction step are not available. Because precipitation and dissolution reactions are likely to be faster than mass-transport processes in highly compacted bentonite it is not necessary to accurately define the value of  $k_2$  provided the reaction is fast compared to the rate of mass transport. Here, an arbitrary rate constant of  $10^{-5} \text{ s}^{-1}$  is assumed, equivalent to a half-life of 19 hours.

**DeH2 = 60000 J/mol**

Activation energy for k2 (assumed value).

**k3room = 1e-02 dm<sup>3</sup>/(mol.s)**

Rate constant for the conversion of  $\text{Fe}(\text{OH})_2$  to  $\text{FeCO}_3$  in the presence of  $\text{HCO}_3^-$ . Kinetic data for this reaction are not available. Because precipitation and dissolution reactions are likely to be faster than mass-transport processes in highly compacted bentonite it is not necessary to accurately define the value of  $k_3$  provided the reaction is fast compared to the rate of mass transport. Here, an arbitrary second-order rate constant of  $10^{-2} \text{ dm}^3 \text{ mol}^{-1} \text{ s}^{-1}$  is assumed, corresponding to a half-life for  $\text{Fe}(\text{OH})_2$  of 19 hours in the presence of  $0.001 \text{ mol}\cdot\text{dm}^{-3} \text{ HCO}_3^-$ .

**DeH3 = 60000 J/mol**

Activation energy for k3 (assumed value).

**k4room = 1.0e-07 1/s**

Rate constant for the Schikorr reaction. This reaction is known to be slow at temperatures below  $80^\circ\text{C}$  so a small value is assigned to the first-order rate constant at room temperature ( $1 \times 10^{-7} \text{ s}^{-1}$ ), equivalent to a half-life of precipitated  $\text{Fe}(\text{OH})_2$  of 80 days.

**DeH4 = 60000 J/mol**

Activation energy for k4 (assumed value).

**k5room = 1.0e-05 1/s**

Homogeneous reaction rate constant for the precipitation of  $\text{FeCO}_3$  from  $\text{Fe}(\text{CO}_3)_2^{2-}$ . Kinetic data for this reaction are not available. Because precipitation and dissolution reactions are likely to be faster than mass-transport processes in highly compacted bentonite it is not necessary to accurately define the value of  $k_5$  provided the reaction is fast compared to the rate of mass transport. Here, an arbitrary rate constant of  $10^{-5} \text{ s}^{-1}$  is assumed, equivalent to a half-life of 19 hours.

**DeH5 = 60000 J/mol**

Activation energy for k5 (assumed value).

**km5room = 1.0e-04 dm<sup>3</sup>/(mol.s)**

Second-order rate constant for the dissolution of  $\text{FeCO}_3$  in the presence of  $\text{HCO}_3^-$ . The value of the rate constant has been selected such that the half-life of  $\text{FeCO}_3$  is 80 days in  $0.001 \text{ mol}\cdot\text{dm}^{-3} \text{ HCO}_3^-$ , reflecting the limited solubility of ferrous carbonate.

**DeHm5 = 60000 J/mol**

Activation energy for km5 (assumed value).

**k6room = 2.4e-10 mol/(dm<sup>3</sup>.s)**

Zeroth-order rate constant for the transformation of montmorillonite by Fe(II) ( $2.4 \times 10^{-10} \text{ mol}\cdot\text{dm}^{-3}\cdot\text{s}^{-1}$  at 25°C). The rate-controlling process is assumed to be the dissolution of montmorillonite for which a value was taken from the compilation of Palandri and Kharaka (2004). The surficial dissolution rate of  $3.89 \times 10^{-15} \text{ mol}\cdot\text{m}^{-2}\cdot\text{s}^{-1}$  was converted to a volumetric dissolution rate by multiplying by the specific surface area ( $37.5 \text{ m}^2\cdot\text{g}^{-1}$ , Wersin et al. 2007) and the bentonite dry density ( $1.65 \text{ Mg}\cdot\text{m}^{-3}$ ).

Because the preceding dissolution step is assumed to be rate controlling, the same value for the rate constant is used for the interaction of montmorillonite with  $\text{FeCl}^+$  ( $k_6$ ),  $\text{Fe}(\text{CO}_3)_2^{2-}$  ( $k_{12}$ ), and  $\text{FeOH}^+$  ( $k_9$ ).

**DeH6 = 48000 J/mol**

Activation energy for k6 from Palandri and Kharaka (2004).

**k7room = 2e-03 dm<sup>3</sup>/(mol.s)**

Homogeneous reaction rate for the adsorption of  $\text{FeCl}^+$  on bentonite at 25°C. Value taken by analogy with that for Cu(II) (King and Kolar 2000).

**DeH7 = 0 J/mol**

Activation energy for k7. Value taken by analogy with that for Cu(II) (King and Kolar 2000).

**km7room = 1e-06 1/s**

Homogeneous reaction rate for the desorption of Fe(II) from bentonite at 25°C to form  $\text{FeCl}^+$ . Value taken by analogy with that for Cu(II) (King and Kolar 2000).

**DeHm7 = 0 J/mol**

Activation energy for km7. Value taken by analogy with that for Cu(II) (King and Kolar 2000).

**k8room = 1.0e-05 1/s**

Homogeneous reaction rate constant for the hydrolysis of  $\text{FeCl}^+$  to form  $\text{Fe}(\text{OH})_2$ . Kinetic data for this homogeneous reaction step are not available. Because precipitation and dissolution reactions are likely to be faster than mass-transport processes in highly compacted bentonite it is not necessary to accurately define the value of  $k_8$  provided the reaction is fast compared to the rate of mass transport. Here, an arbitrary rate constant of  $10^{-5} \text{ s}^{-1}$  is assumed, equivalent to a half-life of 19 hours.

**DeH8 = 60000 J/mol**

Activation energy for k8 (assumed value).

**km8room = 1.0e-06 1/s**

Homogeneous reaction rate constant for the dissolution of  $\text{Fe}(\text{OH})_2$  to form  $\text{FeCl}^+$ . Kinetic data for this reaction are not available. Because precipitation and dissolution reactions are likely to be faster than mass-transport processes in highly compacted bentonite it is not necessary to accurately define the value of  $k_8$  provided the reaction is fast compared to the rate of mass transport. Here, an arbitrary rate constant of  $10^{-6} \text{ s}^{-1}$  is assumed, equivalent to a half-life of 8 days. The dissolution rate constant is assumed to be smaller than that for precipitation in order to allow the solid to form during the simulations.

**DeHm8 = 60000 J/mol**

Activation energy for km8 (assumed value).

**k9room = 2.4e-10 mol/(dm<sup>3</sup>.s)**

Zeroth-order rate constant for the transformation of montmorillonite by Fe(II) ( $2.4 \times 10^{-10} \text{ mol}\cdot\text{dm}^{-3}\cdot\text{s}^{-1}$  at 25°C). The rate-controlling process is assumed to be the dissolution of montmorillonite for which a value was taken from the compilation of Palandri and Kharaka (2004). The surficial dissolution rate of  $3.89 \times 10^{-15} \text{ mol}\cdot\text{m}^{-2}\cdot\text{s}^{-1}$  was converted to a volumetric dissolution rate by multiplying by the specific surface area ( $37.5 \text{ m}^2\cdot\text{g}^{-1}$ , Wersin et al. 2007) and the bentonite dry density ( $1.65 \text{ Mg}\cdot\text{m}^{-3}$ ).

Because the preceding dissolution step is assumed to be rate controlling, the same value for the rate constant is used for the interaction of montmorillonite with  $\text{FeCl}^+$  ( $k_6$ ),  $\text{Fe}(\text{CO}_3)_2^{2-}$  ( $k_{12}$ ), and  $\text{FeOH}^+$  ( $k_9$ ).

**DeH9 = 48000 J/mol**

Activation energy for k9 from Palandri and Kharaka (2004).

**k10room = 2e-03 dm<sup>3</sup>/(mol.s)**

Homogeneous reaction rate for the adsorption of  $\text{FeOH}^+$  on bentonite at 25°C. Value taken by analogy with that for Cu(II) (King and Kolar 2000).

**DeH10 = 0 J/mol**

Activation energy for k10. Value taken by analogy with that for Cu(II) (King and Kolar 2000).

**km10room = 1e-06 1/s**

Homogeneous reaction rate for the desorption of Fe(II) from bentonite at 25°C to form  $\text{FeOH}^+$ . Value taken by analogy with that for Cu(II) (King and Kolar 2000).

**DeHm10 = 0 J/mol**

Activation energy for km10. Value taken by analogy with that for Cu(II) (King and Kolar 2000).

**k11room = 1.0e-05 1/s**

Homogeneous reaction rate constant for the reaction between  $\text{FeOH}^+$  and  $\text{H}_2\text{O}$  to form precipitated  $\text{Fe}(\text{OH})_2$ . Kinetic data for this homogeneous reaction step are not available. Because precipitation and dissolution reactions are likely to be faster than mass-transport processes in highly compacted bentonite it is not necessary to accurately define the value of  $k_{11}$  provided the reaction is fast compared to the rate of mass transport. Here, an arbitrary rate constant of  $10^{-5} \text{ s}^{-1}$  is assumed, equivalent to a half-life of 19 hours.

**DeH11 = 60000 J/mol**

Activation energy for k11 (assumed value).

**km11room = 1e-06 1/s**

Homogeneous reaction rate constant for the dissolution of  $\text{Fe}(\text{OH})_2$  to form  $\text{FeOH}^+$ . Kinetic data for this reaction are not available. Because precipitation and dissolution reactions are likely to be faster than mass-transport processes in highly compacted bentonite it is not necessary to accurately define the value of  $k_{11}$  provided the reaction is fast compared to the rate of mass transport. Here, an arbitrary rate constant of  $10^{-6} \text{ s}^{-1}$  is assumed, equivalent to a half-life of

8 days. The dissolution rate constant is assumed to be smaller than that for precipitation in order to allow the solid to form during the simulations.

**DeHm11 = 60000 J/mol**

Activation energy for km11 (assumed value).

**k12room = 2.4e-10 mol/(dm<sup>3</sup>.s)**

Zeroth-order rate constant for the transformation of montmorillonite by Fe(II) ( $2.4 \times 10^{-10} \text{ mol}\cdot\text{dm}^{-3}\cdot\text{s}^{-1}$  at 25°C). The rate-controlling process is assumed to be the dissolution of montmorillonite for which a value was taken from the compilation of Palandri and Kharaka (2004). The surficial dissolution rate of  $3.89 \times 10^{-15} \text{ mol}\cdot\text{m}^{-2}\cdot\text{s}^{-1}$  was converted to a volumetric dissolution rate by multiplying by the specific surface area ( $37.5 \text{ m}^2\cdot\text{g}^{-1}$ , Wersin et al. 2007) and the bentonite dry density ( $1.65 \text{ Mg}\cdot\text{m}^{-3}$ ).

Because the preceding dissolution step is assumed to be rate controlling, the same value for the rate constant is used for the interaction of montmorillonite with  $\text{FeCl}^+$  ( $k_6$ ),  $\text{Fe}(\text{CO}_3)_2^{2-}$  ( $k_{12}$ ), and  $\text{FeOH}^+$  ( $k_9$ ).

**DeH12 = 48000 J/mol**

Activation energy for k12 from Palandri and Kharaka (2004).

**k13room = 2e-03 dm<sup>3</sup>/(mol.s)**

Homogeneous reaction rate for the adsorption of  $\text{Fe}(\text{CO}_3)_2^{2-}$  on bentonite at 25°C. Value taken by analogy with that for Cu(II) (King and Kolar 2000).

**DeH13 = 0 J/mol**

Activation energy for k13. Value taken by analogy with that for Cu(II) (King and Kolar 2000).

**km13room = 1e-06 1/s**

Homogeneous reaction rate for the desorption of Fe(II) from bentonite at 25°C to form  $\text{Fe}(\text{CO}_3)_2^{2-}$ . Value taken by analogy with that for Cu(II) (King and Kolar 2000).

**DeHm13 = 0 J/mol**

Activation energy for km13. Value taken by analogy with that for Cu(II) (King and Kolar 2000).

**k15room = 1.9e-05 mol/(dm<sup>3</sup>.s)**

Zero-order rate constant for the dissolution of calcite ( $1.9 \times 10^{-5} \text{ mol}\cdot\text{dm}^{-3}\cdot\text{s}^{-1}$  at 25°C). Based on the expression of Plummer et al. (1979), as discussed by Langmuir (1997). For near-neutral solutions with  $p_{\text{CO}_2} < 10 \text{ kPa}$ , the dissolution of  $\text{CaCO}_3$  can be described by a zero-order reaction for the process:



For temperatures of 25°C and higher, the rate constant is given by:

$$\log k = 1.10 - 1737/T \quad (\text{A-7})$$

where T is the temperature in K. Implicit in the use of this expression are the assumptions that the system is far from equilibrium, i.e., the dissolved  $\text{Ca}^{2+}$  and  $\text{HCO}_3^-$  concentrations are small, and that the surface area of calcite is constant. The former assumption may not be valid for

either the bentonite pore water or the groundwater, but the inclusion of the back reaction would require the addition of another species ( $\text{Ca}^{2+}$ ) to the model, with a consequent increase in execution time. The latter assumption will be valid at short times, but will become increasingly invalid as  $\text{CaCO}_3$  is dissolved.

**DeH15 = 33000 J/mol**

Activation energy for k15, based on the temperature dependence from Equation (A-7).

**rho7 = 3400 kg/m<sup>3</sup>**

Skeletal density of  $\text{Fe}(\text{OH})_2$  precipitate (CRC Press 1982).

**M7 = 0.08986 kg/mol**

Molar mass of  $\text{Fe}(\text{OH})_2$ .

**rho8 = 5180 kg/m<sup>3</sup>**

Skeletal density of  $\text{Fe}_3\text{O}_4$  precipitate (CRC Press 1982).

**M8 = 0.2315 kg/mol**

Molar mass of  $\text{Fe}_3\text{O}_4$ .

**rho9 = 3800 kg/m<sup>3</sup>**

Skeletal density of  $\text{FeCO}_3$  precipitate (CRC Press 1982).

**M9 = 0.1159 kg/mol**

Molar mass of  $\text{FeCO}_3$ .

**epsMin = 0.01**

Minimum precipitate porosity at C-steel surface (variable).

**E0Aroom = -0.650 V\_SCE**

Standard potential for dissolution of C-steel at 25°C (CRC Press 1982).

**E0Croom = -0.764 V\_SCE**

Standard potential for reduction of  $\text{HCO}_3^-$ .

Standard potential for the reduction of  $\text{HCO}_3^-$  at 25°C ( $E_D^0 = -0.764 V_{\text{SCE}}$  at pH 8 and  $p_{\text{H}_2} = 5$  MPa).

**E0Droom = -0.764 V\_SCE**

Standard potential for reduction of  $\text{H}_2\text{O}$ .

Standard potential for the reduction of  $\text{H}_2\text{O}$  at 25°C ( $E_D^0 = -0.764 V_{\text{SCE}}$  at pH 8 and  $p_{\text{H}_2} = 5$  MPa).

The values for  $E_D^0$  and  $\Delta E_D^0$  were calculated from the theoretical dependence of the potential for  $\text{H}_2\text{O} + e^- \rightarrow \frac{1}{2}\text{H}_2 + \text{OH}^-$  namely,

$$E_D^0(V_{\text{SHE}}) = 0.000 - \frac{2.3RT}{F} \text{pH} - \frac{2.3RT}{2F} \log p_{\text{H}_2}$$

where  $p_{H_2}$  is the partial pressure of  $H_2$  and the convention is used that the standard potential for the evolution of  $H_2$  is zero at all temperatures. Values for  $E_D^0$  were calculated for various temperatures at pH 8 and  $p_{H_2} = 5$  MPa (the hydrostatic pressure at a depth of 500 m). The value of  $\Delta E_D^0$  was obtained from the linear dependence of  $E_D^0$  on temperature.

**DeE0A = 0.00068 V/K**

Linear temperature dependence coefficient for E0A (D.J. Jobe, private communication, 1998).

**DeE0C = -0.0019 V/K**

Linear temperature dependence coefficient for E0C (D.J. Jobe, private communication, 1998).

**DeE0D = -0.0019 V/K**

Linear temperature dependence coefficient for E0D. See explanation given for E0Droom above.

**kAroom = 2.2e-07 mol/(dm<sup>2</sup> s)**

Anodic rate constant. Zeroth-order electrochemical rate constant for the irreversible interfacial oxidation of Fe to  $Fe^{2+}$  at 25°C ( $2.2 \times 10^{-9}$  mol·cm<sup>-2</sup>·s<sup>-1</sup>). Derived from the data of Marsh and Taylor (1988).

**DeHA = 104,000 J/mol**

Activation energy for kA. Temperature dependence of  $k_A$  (104 kJ·mol<sup>-1</sup>). Derived from the data of Marsh and Taylor (1988).

**kCroom = 1.7e-10 dm/s**

Cathodic rate constant for the reduction of  $HCO_3^-$  to  $CO_3^{2-}$ . Based on data from Gray et al. (1990).

**DeHC = 60000 J/mol**

Activation energy for  $k_C$ . Assumed value.

**kDroom = 1.2e-09 mol/(dm<sup>2</sup> s)**

Cathodic rate constant. Interfacial rate constant for the cathodic reduction of  $H_2O$  on C-steel at 25°C ( $k_D = 1.2 \times 10^{-11}$  mol·cm<sup>-2</sup>·s<sup>-1</sup>). Mean value of the data of Turnbull and May (1987) and Marsh and Taylor (1988).

The parameter values for  $k_D$ ,  $\Delta H_D$  and  $\alpha_D$  are taken from studies on the cathodic reduction of  $H_2O$  on C-steel in 3-3.5 wt.% (0.5-0.6 mol·dm<sup>-3</sup>) NaCl solution by Turnbull and May (1987) and Marsh and Taylor (1988). Marsh and Taylor worked at temperatures between 20°C and 90°C and found the values to be independent of pH in the range pH 4-10. Turnbull and May report data for temperatures between 5°C and 40°C and those data for pH 9.5 are used here. In both studies, there was no systematic variation of  $\alpha_D$  with temperature. The data reported by the two groups of workers are consistent and the data given are mean values from the two studies.

**DeHD = 52,100 J/mol**

Activation energy for  $k_D$ . Temperature dependence of  $k_D$  (52.1 kJ·mol<sup>-1</sup>). Mean value of the data of Turnbull and May (1987) and Marsh and Taylor (1988).

See explanation given for kDroom above.

**alfaA = 1.08**

Tafel constant for the oxidation of Fe ( $\alpha_A = 1.08$ ). Based on the data of Marsh and Taylor (1988).

**alfaC = 0.36**

Transfer coefficient for the reduction of  $\text{HCO}_3^-$ . Based on data from Gray et al. (1990).

**alfaD = 0.48**

Transfer coefficient for the reduction of  $\text{H}_2\text{O}$ . Transfer coefficient for the reduction of  $\text{H}_2\text{O}$  on C-steel ( $\alpha_K = 0.48$ ). Mean value of the data of Turnbull and May (1987) and Marsh and Taylor (1988).

See explanation given for kDroom above.

**nB = 1**

Number of electrons transferred in the rate-determining step for the dissolution of C-steel.

**nC = 1**

Number of electrons transferred in the reduction of  $\text{HCO}_3^-$ .

**nD = 1**

Number of electrons transferred in the reduction of  $\text{H}_2\text{O}$ .

**c5R = 1.8e-03 mol/dm<sup>3</sup>**

RHS boundary concentration for  $\text{HCO}_3^-$  based on the reference SR-270-PW groundwater concentration of 110 mg/L (G. Kwong, private communication 2010).

**c6R = 4.75 mol/dm<sup>3</sup>**

RHS boundary concentration for  $\text{Cl}^-$  based on the reference SR-270-PW groundwater concentration of 168,500 mg/L (G. Kwong, private communication 2010).

**rhoW = 1.0204 kg/dm<sup>3</sup>**

Groundwater density at 0°C.

**Rgas = 8.314 J/(K.mol)**

Gas constant.

**Farad = 96487 C/mol**

Faraday constant.

**hkmin = 1.0**

Humidity value below which surface reaction rates are 0. Defined as the minimum threshold relative humidity typically reported for atmospheric corrosion (Leygraf and Graedel 2000, Shreir et al. 1993).

**hkmax = 1.0**

Humidity value above which surface reaction rates equal their maximum values (corresponding to saturated conditions). For numerical reasons, the humidity at which interfacial electrochemical reactions are supported is treated as a range. The upper end of the range is arbitrarily taken as 0.7, which is within the range of threshold relative humidity values for atmospheric corrosion (Leygraf and Graedel 2000, Shreir et al. 1993).

**rhsT\_in = tempFract**

Name of file with RHS temperature b.c. formatted as: time (a) temperature (°C).

**H0 = -0.072**

If negative: Use LHS temperature b.c. file (lhsT\_in); otherwise: use container heat output file (heat\_in) and scale it by H0.

**lhsT\_in = tempCont**

Name of file with lhs temperature b.c. formatted as: time (a) temperature (°C).

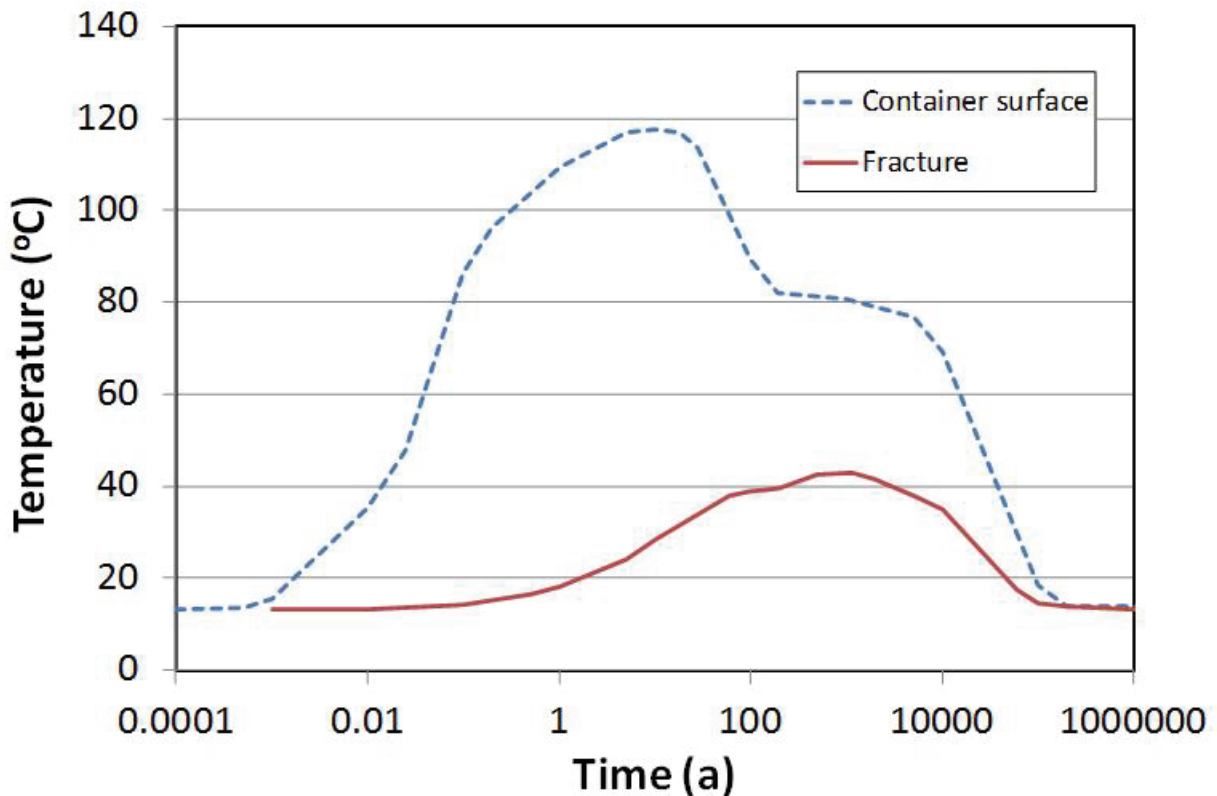


**Figure A-2: Container Surface and Fracture Temperature Profiles Used in the SCM V1.0**

Temperature profiles for the container surface and a point in the far-field representing the right-hand boundary of the model were taken from the study of Guo (2010).

**heat\_in = HeatSource**

Name of file with heat source formatted as: time (a) Output (W/dm<sup>2</sup>).

**initT\_in = templnit**

Name of file with initial temperature formatted as: x (dm) temperature (°C).

## REFERENCES

- Anderko, A. 2000. Simulation of  $\text{FeCO}_3/\text{FeS}$  scale formation using thermodynamic and electrochemical models. In Proc. CORROSION/2000, paper no. 00102 (NACE International, Houston, TX).
- Craig, R.F. 1987. Soil Mechanics. Fourth edition. Van Nostrand Reinhold (International) (London, UK).
- CRC Press. 1982. Handbook of Chemistry and Physics, 63<sup>rd</sup> Edition, 1982-1983. CRC Press, Boca Raton, FL.
- Garisto, F., A. D'Andrea, P. Gierszewski, and T. Melnyk. 2004. Third Case Study – reference data and codes. Ontario Power Generation Nuclear Waste Management Division Report No: 06819-REP-01200-10107-R00.
- Gierszewski, P., J. Avis, N. Calder, A. D'Andrea, F. Garisto, C. Kitson, T. Melnyk, K. Wei and L. Wojciechowski. 2004. Third Case Study - Postclosure Safety Assessment. Ontario Power Generation, Nuclear Waste Management Division Report 06819-REP-01200-10109-R00. Toronto, Canada.
- Gray, L.G.S., B.G. Anderson, M.J. Danysh, and P.R. Tremaine. 1990. Effect of pH and temperature on the mechanism of carbon steel corrosion by aqueous carbon dioxide. In Proc. CORROSION/90, paper no. 40 (NACE International, Houston, TX).
- Guo, R. 2010. Coupled thermal-mechanical modelling of a deep geological repository using the horizontal tunnel placement method in sedimentary rock using CODE\_BRIGHT. Nuclear Waste Management Organization Technical Report No.: NWMO TR-2010-22.
- King, F., and M. Kolar. 2000. The copper container corrosion model used in AECL's second case study. Ontario Power Generation Nuclear Waste Management Division Report No: 06819-REP-01200-10041-R00.
- King, F., M. Kolar, and P. Maak. 2008. Reactive-transport model for the prediction of the uniform corrosion behaviour of copper used fuel containers. *J. Nucl. Mater.* 379, 133-141.
- Langmuir, D. 1997. Aqueous Environmental Geochemistry. Prentice Hall (Upper Saddle River, NJ).
- Leygraf, C. and T.E. Graedel. 2000. Atmospheric Corrosion. Wiley Interscience. New York, USA.
- Marsh, G.P and K.J. Taylor. 1988. An assessment of carbon steel containers for radioactive waste disposal. *Corros. Sci.* 28, 289-320.
- Mazurek, M. 2004. Long-term used nuclear fuel waste management – geoscientific review of the sedimentary sequence in Southern Ontario. Nuclear Waste Management Organization Background Papers, 6. Technical Methods, Report 6-12.

- Nagra. 2002. Project Opalinus Clay. Safety Report. National Cooperative for the Disposal of Radioactive Waste, Nagra Technical Report NTB 02-05.
- Oscarson, D.W. and D.A. Dixon. 1989. Elemental, mineralogical, and pore-solution composition of selected Canadian clays. Atomic Energy of Canada Limited Report, AECL-9891.
- Palandri, J.L. and Y.K. Kharaka. 2004. A compilation of rate parameters of water-mineral interaction kinetics for application to geochemical modeling. U.S. Geological Survey Open File Report 2004-1068.
- Pan, P. 1997. Unpublished work. Atomic Energy of Canada Limited.
- Plummer, L.N., D.L. Parkhurst, and T.M.L. Wigley. 1979. Critical review of the kinetics of calcite dissolution and precipitation. *In* Chemical Modeling in Aqueous Systems, ed. E.A. Jenne (American Chemical Society, Washington, DC), Am. Chem. Soc. Symp. 93, 537-573.
- Posiva. 2006. Expected evolution of a spent nuclear fuel repository at Olkiluoto. Posiva Report, Posiva 2006-05.
- Sander, R. 1999. Compilation of Henry's law constants for inorganic and organic species of potential importance in environmental chemistry. <http://www.mpch-mainz.mpg.de/~sander/res/henry.html>.
- Shreir, L.L., R.A. Jarman, and G.T. Burstein. 1993. Corrosion. Volume 1 Metal/Environment Reactions, 3<sup>rd</sup> Edition. Butterworth-Heinemann. Oxford, UK.
- Turnbull, A. and A.T. May. 1987. Steady state electrochemical kinetics of BS 4360 50D structural steel in deaerated 3.5% NaCl solution of varying pH. *British Corrosion* 22, 176-181.
- Walke, R., A. Bath, A. Bond, N. Calder, P. Humphreys, F. King, R. Little, R. Metcalfe, J. Penfold, J. Rees, D. Savage, G. Towler, and R. Walsh. 2009. Postclosure safety assessment (V1): data. Nuclear Waste Management Organization Technical Report No.: NWMO DGR-TR-2009-08.
- Wersin, P., L.H. Johnson, B. Schwyn, U. Berner, and E. Curti. 2003. Redox conditions in the near field of a repository for SF/HLW and ILW in Opalinus Clay. Nagra Technical Report, NTB 02-13.
- Wersin, P., M. Birgersson, S. Olsson, O. Karnland, and M. Snellman. 2007. Impact of corrosion-derived iron on the bentonite buffer within the KBS-3H disposal concept – the Olkiluoto site as case study. Posiva Report, Posiva 2007-11.